Upgrading Standard Laboratory Equipment with Microfluidic Techniques

By

Jacob J. Tokar

A dissertation submitted in partial fulfillment of

the requirements for the degree of

Doctor of Philosophy

(Biomedical Engineering)

at the

UNIVERSITY OF WISCONSIN-MADISON

2019

Date of final oral examination: 6/12/2019

The dissertation is approved by the following members of the Final Oral Committee:
David J. Beebe, Professor, Biomedical Engineering
Randolph S. Ashton, Professor, Biomedical Engineering
Joshua M. Lang, MD, Oncology
J. Scott Ferguson, MD, Pulmonology
Justin C. Williams, Department Chair, Biomedical Engineering

Copyright Page

Acknowledgements

Oof da, this PhD has been a ride. I owe a lot of thanks to a lot of people, but I must start with Dr. David Beebe. Dave gave me the opportunity to work in his lab as an undergrad back in the summer of 2012 when I was still a Mechanical Engineering student at UW-Platteville. Fortunately for me, Dave has a soft spot for Platteville Engineering students. I learned a lot that summer and I loved every second of it, which is why I ultimately transferred to UW-Madison to finish my Bachelors and start my graduate degree in Biomedical Engineering. Thank you, Dave, for your mentorship and the many influential opportunities you have provided me.

Next, I must thank my remaining committee members. Thank you, Dr. Josh Lang, Dr. Randolph Ashton, Dr. Scott Ferguson, and Dr. Justin Williams for all of your tutelage over the years. With all of the travelling Dave has done throughout my PhD, it was always reassuring to know that I could come to each of you if I had questions about experiments, writing, etc.

I would like to express my deepest gratitude to Dr. Jay Warrick, without whom I might not have ever made it through to the end. Jay has helped me in countless ways over the years. Many of the experiments presented in this thesis were discussed with Jay at some point. I learned the most about experimental design from Jay. He also introduced me to R and the world of Data Science. Thank you, Jay.

I should also thank Dr. Ben Casavant, Dr. Mary Regier, Dr. Erwin Berthier, and Dr. David Guckenberger for all of their help over the years. In addition, I need to thank my undergrads, Courtney Lynch and Ben Horman. Without their help, I would not graduate for another two years. They were constantly milling and molding devices for me, saving me a great deal of time, which I could dedicate to other things.

Thank you to my family and friends who have supported me over the years. My mom was always sending me treats. My dad taught me the meaning of a hard day's work. My grandma took me to

museums, zoos, and aquariums, sparking my initial interest in science. My brother is always happy to take me fishing, helping me to clear my mind when life gets crazy. My younger sister has always been a motivation to me because I wanted to be the best role model for her, though I am not sure how well that is going.

Finally, I need to thank my longtime girlfriend, Jessica. Starting a long-term relationship at the beginning of a PhD is not the most conducive environment for a successful partnership, but we have figured it out over the years. The stresses and anxieties of grad school have allowed us to learn a lot about one another and we are stronger for it. She has been extremely helpful throughout this whole process and I honestly cannot imagine getting through it without her, looking back. Thank you, Jess, love you.

Abstract

The field of Microfluidics has made major strides over the last two decades, having an increasingly more important role biomedical research. As microfluidics and biomedical research have become more dependent on each other's success, scientists have begun to adapt microfluidic technology to better integrate with established biomedical laboratory equipment; such as plate readers, microscopes and liquid handling robots. Because many laboratory machines are built to work with tissue culture well-plates, much of microfluidic integration has involved either mimicking or modifying well-plates. Other modes of integration have involved retrofitting devices to microscopes for real-time imaging and manipulation of microfluidic samples. In this thesis we present several different techniques for upgrading laboratory equipment with microfluidic technology. First, we upgraded a liquid handling robot with a surface tension driven analyte extraction plate, which was used to isolate lung cancer cells from bronchoalveolar lavage samples. Second, we upgraded a fluorescent microscope with a semi-automated single cell aspirator platform, which relies on a specialized microwell array to entrap and isolate single cells from a heterogeneous population. Using the semi-automated aspirator, we were able to acquire highly enriched circulating tumor cell samples in quick fashion, protecting the integrity of RNA for PCR analysis and comparison to patient outcome. Finally, we upgraded well-plates with simple microfluidic inserts to increase tissue model complexity, while keeping operational complexity at a minimum. With hydrogel gradient stamps, we were able to explore breast cancer tissue cultures over a multi-day treatment of chemotherapy gradients. We were also able to explore spatial differentiation of human pluripotent stem cell derived neural organoids after they were treated with a Sonic Hedgehog gradient for four days. Each of these techniques demonstrate the technological potential of microfluidic upgrades to standard laboratory equipment.

Table of Contents

List of Figures

1. Microfluidics for well-plates: the next generation of well inserts for high-throughput tissue modeling

Jacob J. Tokar, Jay W. Warrick, David J. Beebe (To be submitted to Lab on a Chip)

The use of microfluidic techniques for biomedical research has produced interesting findings in recent years. In fact, the unique properties provided by microfluidic physics has enabled researchers to develop *in vitro* tissue models with ever increasing complexity, becoming more mimetic of *in vivo* tissue environments. As microfluidic tissue models become more relevant, they could eventually provide cheaper, more humane methods with which to study disease, toxicology, and development. Unfortunately, biomedical research has been slow to adopt microfluidic tissue models as reliable research tools. Much of this could be due to the increased operational complexity of many traditional microfluidic devices. Moreover, for many years microfluidics devices offered minimal compatibility with established tissue culture infrastructure – such as plate readers and liquid handling robots. Because these essential research machines are built to interact with multi-well tissue culture plates, one method of microfluidic integration could be to mimic or modify well-plates with microfluidics. In this review we cover the evolution of microfluidic devices from channel arrays that mimic well-plate formats to microfluidic well-plate modifications. Finally, we detail five recent studies that implement a promising new technique that is capable of swiftly upgrading well-plates with microfluidic inserts. The various tissue models demonstrated in these well-plate insert studies illustrate the potential impact this technique could have on the future of *in vitro* tissue models.

1.1 INTRODUCTION

The microfluidic industry has been experiencing greater commercial success recently thanks to advancements in gene sequencing and point-of-care (POC) diagnostic technologies[1]. Key indicators of this success are the ever-increasing number of microfluidic startup companies in the US and around the globe as well as the increase in R&D investment from larger companies. As more microfluidic technologies catch this wave of success, engineers now, more than ever, have to consider the desires of the end users. In the past potential customers have been slow to adopt such technologies because conventional practices are so well integrated with standard lab equipment and require less technical training to operate, negating many of the advertised advantages. By cleverly integrating microfluidic devices with standard laboratory equipment, the industry will continue to experience commercial success.

Integrating microfluidics with laboratory equipment has long been an area of study (Fig. 1.1). Two decades ago, researchers were already thinking about microfluidic integration with liquid handling robots, mimicking the layout of microtiter plates so each tip of the robot is able to add and remove liquid from ports and microwells within the devices[2]. Later on, high throughput assays were also developed to integrate with plate readers[3–5]. In the early 2010s, labs started modifying well plates directly, taking advantage of their ubiquity and familiarity[6,7]. Each of these advancements provide advantages, some even went on to become successful products. However, many such devices experienced minimal adoption of the technology because they share a major disadvantage: they remain highly engineered and require a practiced hand to properly operate.

A specific way to improve the accessibility of microfluidics is to incorporate devices directly into well-plates. The technique of modifying well-plates with a simple insert has already proven to be effective given the success of the Transwell permeable support well. This technology has been used

for over 25 years to perform various types of co-culture experiments to replicate a variety of physiological systems such as immune cell migration[8,9], mesenchymal stem cell migration[10], and the blood-brain barrier[11–13]. In addition to permeable support wells, other well inserts have likewise become commercially available. Such products include CellCrown sample immobilization inserts and removable inserts that define cell seeding regions within a well for wound healing and migration assays[14–16]. While well plate inserts, such as the Transwell, have enabled impactful studies, such experiments have their limitations. Being a 2D co-culture system, Transwell studies lack the complexity to best replicate a tissue microenvironment, missing out on essential cues – chemical, physical, etc. – that have been shown to provide entirely different results[17].

Taking inspiration from the success of Transwell permeable inserts, recent studies have demonstrated simple microfluidic well-plate inserts that provide the *in vitro* tissue complexity of microfluidic technology, while retaining the simplicity of a well-plate[18–22]. This idea could not only have an impact on the high-throughput capabilities of microfluidic systems but could also have a great commercial impact as well. By characterizing the physics and experimenting with various ways of simple integration, such studies provide a groundwork of which future technology can build upon.

1.2 CURRENT RESEARCH

1.2.1 Mimicking MWP Layout

In the early 2000's scientists were first proposing the idea of microfluidic device arrays that mimicked the format of well-plates; the motivation being the integration with high-throughput screening infrastructure such as liquid handling robots and automated plate readers[4]. By the end of the decade, engineers had designed microfluidics to integrate with lab equipment. In 2007 H. Yu, C. Alexander, and D. Beebe presented a plate reader compatible microfluidic array that improved

detection limit and allowed greater microenvironmental control than a traditional 96 well-plate[3]. As the technique of passive pumping became further characterized[23,24], integrating open microfluidic arrays with liquid handling robots became a more viable option, sparking an increase in the development of automated microfluidic high-throughput systems (HTS). In fact, the concept of microfluidic systems built for liquid handling robots has been highly productive over the last decade[25–31]. However, while these technologies are useful in a fully equipped biomedical laboratory, they remain unhelpful for global health initiatives aiming to improve point-of-care testing in areas with limited resources.

Paper microzone plates

Being cheap to produce and easy to operate, paper microfluidics has inspired many global health scientists to develop clever kits and assays. However, being based on colorimetric immunoassays, most paper assays only produce qualitative or binary readouts, providing little more information for clinicians to interpret.

In 2009, E. Carrilho et.al. demonstrated how a paper microfluidic assay could become quantitative by mimicking a well-plate format so the device could be analyzed by a conventional plate reader, measuring both fluorescence and absorbance, depending on the assay[5]. This has led to more recent studies developing point-of-care ELISAs[32], characterizing reagent stability[33], and detecting telomerase activity in paper microzone plates[34]. Providing affordable, robust, and easy to operate point-of-care devices with well-plate formats is an intriguing branch of microfluidic development. However, well-plates are not just used for screening samples, they are also important tools for high-throughput *in vitro* tissue model studies.

HTS Tissue Models

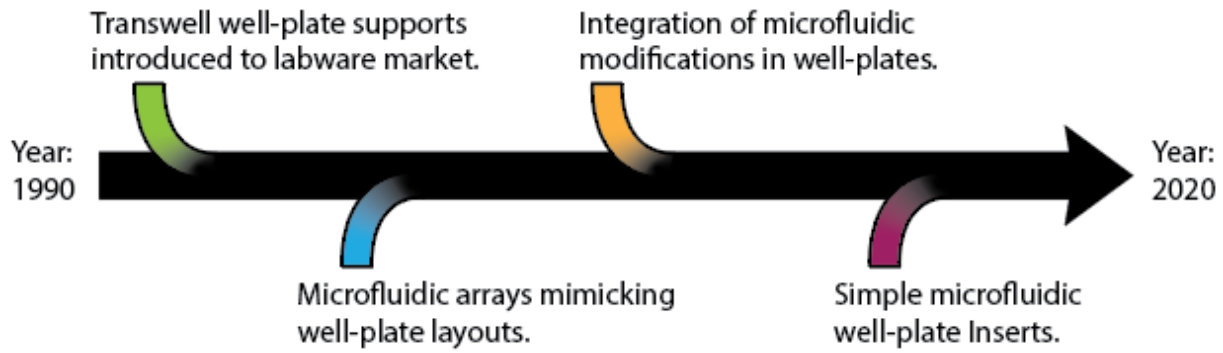

Figure 1.1. *Well-plate Modification Timeline* – Over the last two decades microfluidic engineers have gone from mimicking to modifying well-plates. Only just recently have scientists taking inspiration from the success of Transwell inserts by developing microfluidic well-plate inserts.

Many high throughput studies using well-plates provide little more complexity than a 2D monoculture in a well, though 2.5D and 3D studies are becoming more prevalent. For researchers wanting to perform more complex co-culture studies, technology like Transwell permeable inserts have been a useful tool, but they still lack the tissue complexity that traditional microfluidic devices can provide[35–38].

For some years, 3D spheroid cultures have been a popular way to test basic biology and therapeutics in a more physiologically relevant manner, though traditional methods are tedious and produce highly variable spheroids. In 2011, Y. Tung and A. Hsiao et.al. addressed these concerns by developing a hanging drop spheroid culture array that mimics a 384-well plate that integrates with a liquid handling robot[39]. While the spheroid HTS indeed provided more consistent spheroids, traditional spheroid culture remains prominent. Much of this might be due to scientists already feeling comfortable with established protocols and working with readily available materials, such as well plates. In fact, major well-plate production companies offer their own spheroid culture plates, which use round bottom wells made from material cells cannot attach to rather than hanging droplets.

Well-plate array of microfluidic ELISA devices (2012)

In addition to high-throughput tissue spheroids, mimicking well plate formats have been used to improve standard well-plate assays as will. ELISA's are commonly performed in 96 and 384 well plates. To save on reagents, labs sometimes use 1536 well plates because they only require a few microliters per assay step. Unfortunately, these low volumes are very sensitive to evaporation, leading to high variability in results. Moreover, the surface area for the reaction to take place is also greatly decreased.

To improve on this, Siloam Biosciences developed their Optimiser™ microplate, which consists of an array of 96 spiral micro-channels leading from the bottom of a funnel-shaped input well[40]. The spiral channel provides a large increase in surface area to volume ratio, but it requires only 4.5 μL of volume to operate. This layout makes use of microfluidic advantages, while maintaining the high-throughput capability of well-plate ELISA's.

1.2.2 Modifying MWPs

Because it is difficult and expensive to fabricate small batches of devices that mimic well-plate formats, many engineers began modifying well-plates themselves in the early 2010's as a way of cheaply prototyping an HTS design.

In 2011, C. Conant et.al. demonstrated a microfluidic HTS that tests dynamic platelet behavior under shear stress[6]. This device was fabricated using a now popular technique where the PDMS device array is "sandwiched" between coverglass and the bottom of the well-plate. As with similar devices, the microchannels connect adjacent wells in such a way where the plate wells become fluid reservoirs or sinks during operation. In 2012, Fluxion Biosciences also used the sandwich technique to fabricate a well-plate microfluidic patch-clamp array for automated, high-throughput screening of chemical effects on ion channel function[7].

Similar to the platelet shear and patch clamp plates, other groups have upgraded well plates with active pumping microfluidics to produce tumor microenvironment models and tissue culture

gradients in a high throughput array[41,42]. Although, this requirement for active pumping presents added platform complexity, negating most of the advantages provided by the use of well-plates.

A clever workaround for flow within a well-plate without the need for active pumping is gravity driven flow from one well to an adjacent well, connected via microchannels beneath the bottom of the well-plate. Using this technique scientists have developed systems for specialized cell culture and vascularized micro-organs[43,44]. In each of these studies, a microchannel array was attached to the bottom of a bottomless 96 well plate. Channel inputs, outputs, and other ports were aligned to the bottom of specific wells, enabling high-throughput operation of complex cultures.

1.2.3 Open Microfluidic Inserts

Low-volume MWP insert

To our knowledge, the first study to implement an open microfluidic well-plate insert was demonstrated by Gheibi et.al. in early 2017[18]. Their device leverages the inherently low volumes of microfluidics to amplify endogenous signals of primary hepatocytes in culture (Fig. 1.2A), preventing de-differentiation. A major roadblock for primary hepatocyte research is that they readily de-differentiate *in vitro*, which has slowed advances in liver culture models. In a previous study, the Revzin Lab has shown that culturing hepatocytes within small volume chambers (i.e. - microfluidic devices) can significantly improve retention of a hepatic phenotype, suggesting that endogenous cell signaling plays a key role in proper liver cultures[45]. This phenomenon has also been demonstrated in other cultures such as stem cells and cancer drug resistance[46,47].

With picoliter resolution volumes, microfluidics appears ideal for retaining endogenous signaling in *in vitro* cultures. However, Gheibi et.al. were motivated to go one step further and integrate their device with a well plate, claiming that traditional microfluidic devices too specialized, contributing to difficulties when used by an untrained hand. In contrast, well plates are highly established in biological laboratories because they are simple and easy to use. By designing a microfluidic device

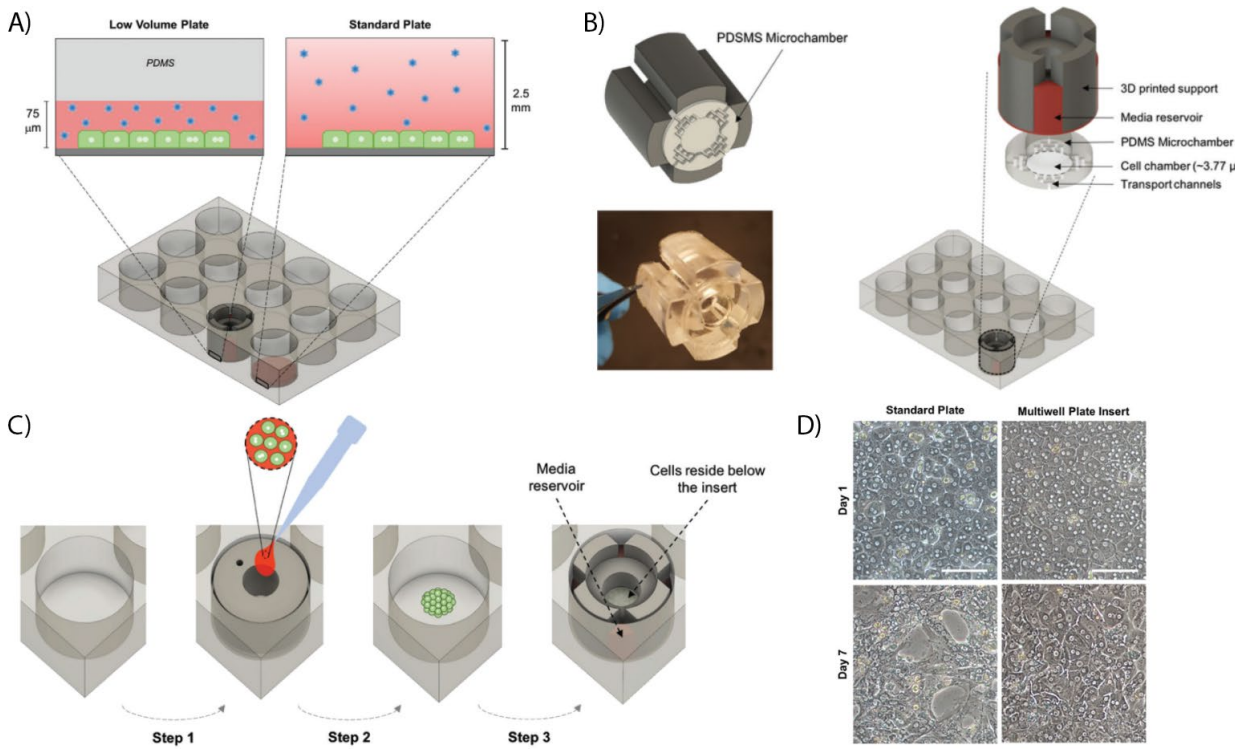

Figure 1.2. *Low-volume Well-plate Insert* – A) Microfluidic volumes concentrate cellular signaling as seen *in vivo* whereas traditional cell culture dilutes signaling. B) A 3D-printed insert attached to a PDMS microfluidic device provides a simple upgrade to high-throughput plates. C) Hepatocytes were seeded in the center of the well using a seeding insert before being switched out with the experimental insert. D) The low-volume insert helps retain primary hepatocyte phenotype by maintaining endogenous signaling.

that can be simply inserted into a standard well plate, researchers can achieve a complex *in vitro culture* while device handling remains easy.

Specifically, in this study, Gheibi et.al. fabricated inserts to fit within a well of a 12-well plate (Fig. 1.2B). These inserts were made of two materials. The bulk of the insert was 3D printed out of a biocompatible polymer. The microfluidic portion was made from PDMS molded within the 3D printed insert, which was properly oriented above an SU-8 master mold. The insert was made hydrophilic via oxygen plasma treatment to promote fluid filling within the microchannels. Once fully fabricated and treated, the device was inserted into the well over the cells, which were seeded 24 hours earlier. The cells were only allowed to grow in the center region of the well using a

seeding insert, ensuring all cells seeded would be within the culture region of the experimental insert (Fig. 1.2C).

Using these well inserts, they were able to significantly demonstrate the retention of hepatic phenotype within the low volume well when compared to a standard plate (Fig. 1.2D). Adding biological complexity, they were also able to co-culture the hepatocytes with fibroblasts by seeding them on the top of the microfluidic chamber before placing the insert in the well. This further enhanced hepatic phenotype as demonstrated by a two-fold increase in albumin production. This study not only demonstrates the advantages of microfluidics for *in vitro* studies, but more importantly demonstrates the promise of a simple microfluidic well-plate adapter.

Rail channel inserts for in-well co-culture

Building off Gheibi et.al., two recent studies have demonstrated the integration of rail-channel micro-devices into standard well-plates. First characterized by S. Berry and T. Shang et.al. in 2017, this type of well insert leverages spontaneous capillary filling and microfluidic pinning to create complex co-culture conditions in a simple manner[19]. Rail channels are non-traditional microfluidic channels that are made up of a rail (top of channel), a well-plate bottom (bottom of channel), and two open sides that interface with adjacent wells of the device (Fig. 1.3A).

The idea of a micro-channel with multiple open sides was first characterized by Casavant and Berthier et.al. in 2013. They demonstrated how specific geometries and surface chemistries promote spontaneous capillary flow within a micro-channel with less than four sides[48]. Used to create fluid flow barriers between neighboring wells, rail channels are filled with a hydrogel solution because – even though flow is inhibited – molecular signaling via diffusion can still freely occur. Having channels with open sides which interface with adjacent air or liquid provides interesting culture capabilities for *in vitro* co-culture tissue models.

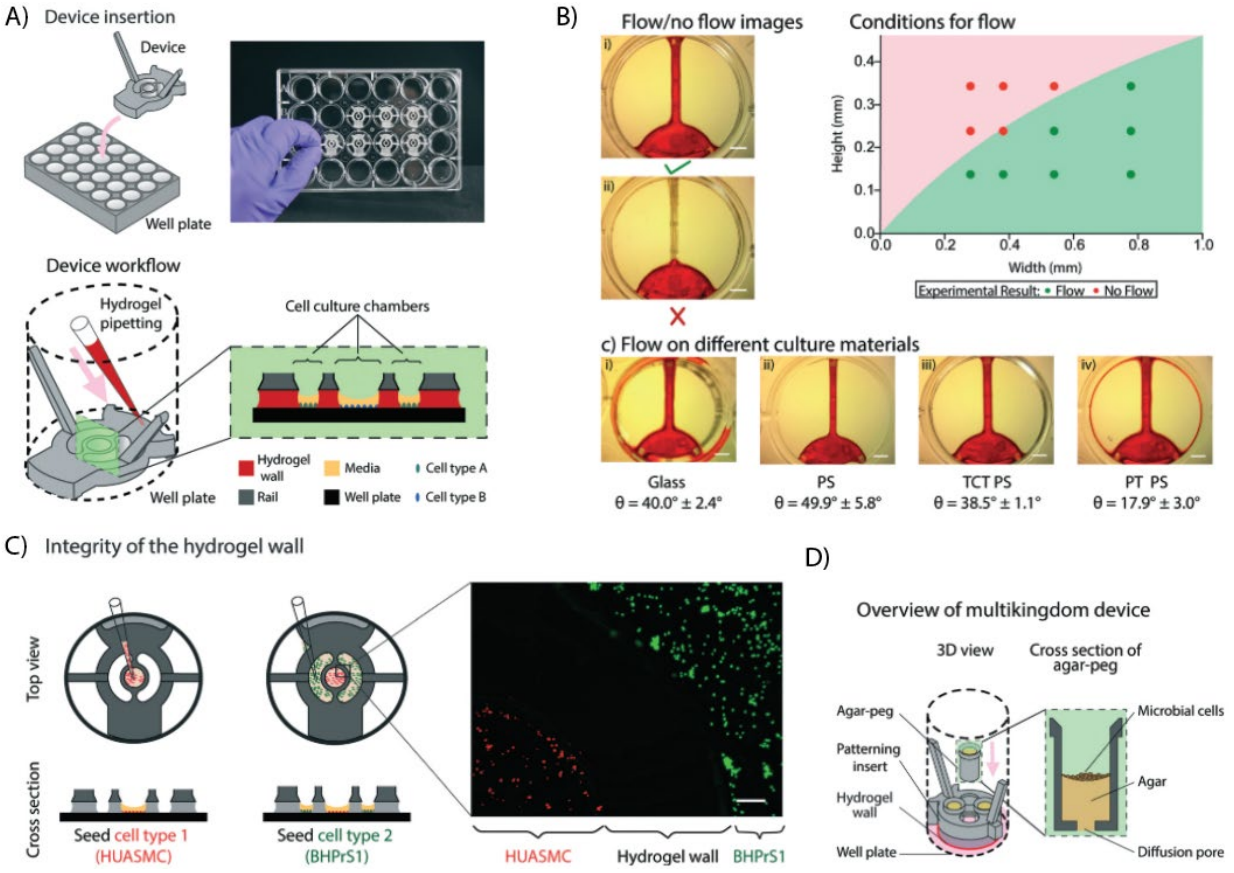

Figure 1.3. *Suspended Rail Channel Inserts* – A) Rail channel inserts readily fit into well-plates and provide significant co-culture capabilities in a high-throughput format. B) Rail channel dimension must be considered carefully when designing a device. C) Rail channels provide robust co-culture barriers, but still allow crosstalk between neighboring culture wells (D).

The advancement of rail micro-channels provides a simple way to add complexity to tissue cultures within standard well plates. The biggest selling point for rail channel inserts should be that such devices make only require standard, tissue-culture treated well-plates to operate properly. This decreases financial burden on labs wanting to increase the complexity of their tissue models because they are not required to purchase specialized equipment or training. Another advantage of rail channel devices is the fact that they use the native substrates within well plates, so once the insert is placed the loading of the device is nearly as straightforward as traditional well plate culture. This reduces the learning curve to operate such devices, increasing the probability more scientists will adopt the technology.

In their study, Berry and Shang et.al. demonstrated a few ways well plate inserts could be used to improve the complexity of well plate cultures with simple design. However, first they characterized loading hydrogels into rail channels, investigating specific design aspects to produce predictable, proper channel filling, increasing user friendliness (Fig. 1.3B). Once optimized, they tested the co-culture capabilities of their designs (Fig. 1.3C-D). Initially, they demonstrated that hydrogel filled rail channels keep distinct cell cultures segregated and contained. Then they were able to replicate established multikingdom co-culture results by observing decreased *A. Fumigatus* (fungus) growth when co-cultured with *P. aeruginosa* (bacteria)[49]. It should be noted that the rail channel inserts demonstrated in this study were engineered with a gel loading well, where all rail channels of a single insert can be filled by a single pipetting step.

Adding to the work done by Berry and Shang et.al., in 2018 Y. Lee and J.W. Choi et.al. published on their own rail-channel insert, characterizing a rail-channel loading technique that does not require a gel loading well that previous designs required[50]. With this technique, the hydrophilic well plate surfaces promote spontaneous flow along the corner of the periphery of the well. This way, when loading a rail channel, all the user needs to do is pipet liquid hydrogel into the outer corner of the well and it will flow and fill the rail channels via capillary action (Fig. 1.4A). By not requiring space dedicated to a loading well, this technique allows rail channel device design to be more flexible and miniaturized further, allowing devices to fit into the smaller wells of 48 and 96-well plates, as was done in this study. This enables high throughput screening of dozens of complex tissue cultures contained within just one plate.

The device demonstrated in this study consisted of two rail channels separated by a middle culture channel, which is filled via two ports through the top of the device (Fig. 1.4B). To test the tissue modeling capabilities of their rail device, Lee and Choi et.al. created a 3D angiogenesis assay (Fig. 1.4C). To do so, rail channels were filled with acellular fibrin gel to separate the middle channel from the left and right reservoirs. The middle channel was seeded with lung fibroblasts

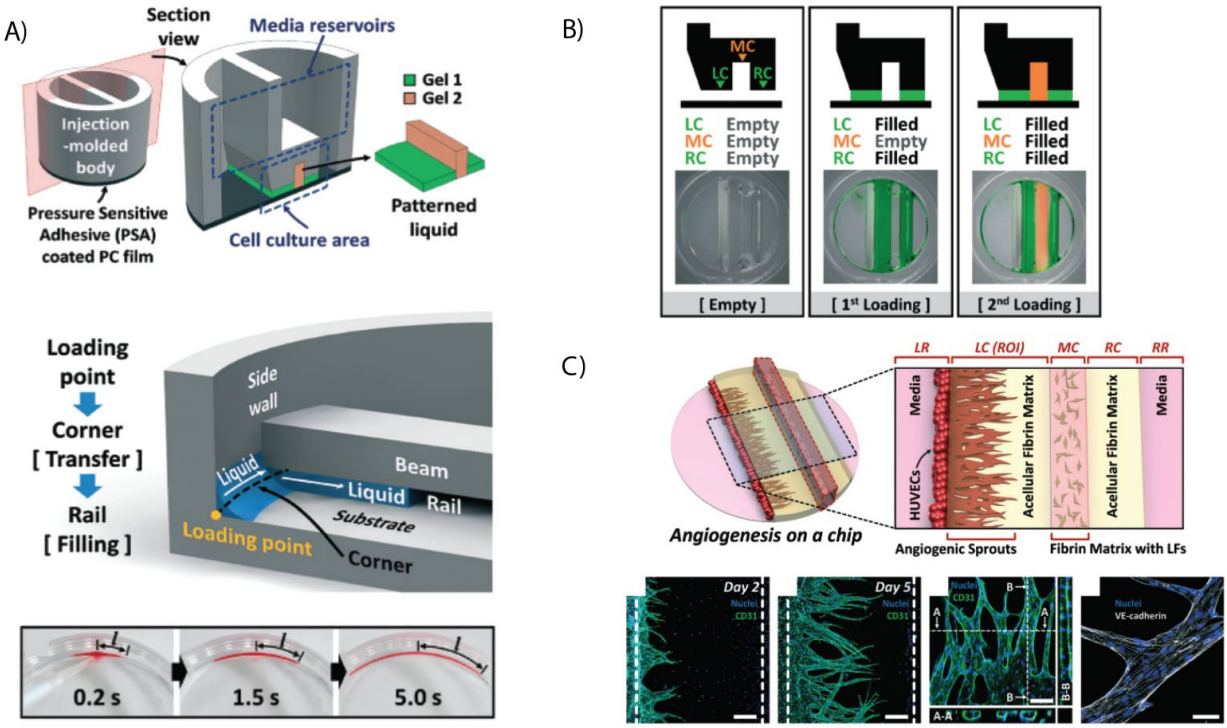

Figure 1.4. *Corner Filled Rail Channel Inserts* – A) Rail channels can be filled via capillary action along the peripheral corner of a well, removing the need for a loading port and saving space. B) Rail channels are filled first so there are barriers in place when culture wells and channels are loaded. C) Rail channels can be used to generate complex angiogenesis assays within a high-throughput format.

embedded in a fibrin matrix. Human endothelial cells (HUVECs) were seeded from the left reservoir onto the outer side of the acellular fibrin matrix in the rail channel. The endothelial cells were allowed to grow for five days, developing into sprouts. By day five the sprouts were found to possess hollow lumen structures (confocal imaging) and strong tight junctions (VE-Cadherin stain), illustrating another complex *in vitro* tissue system to be easily cultured within a well plate. One could imagine such a well-plate platform being used to test things such as anti-angiogenic cancer drugs in a high-throughput, cheap fashion relative to the standard animal models currently used, while retaining more biological complexity than standard well-plate angiogenesis assays.

Hydrogel inserts for 3D co-culture

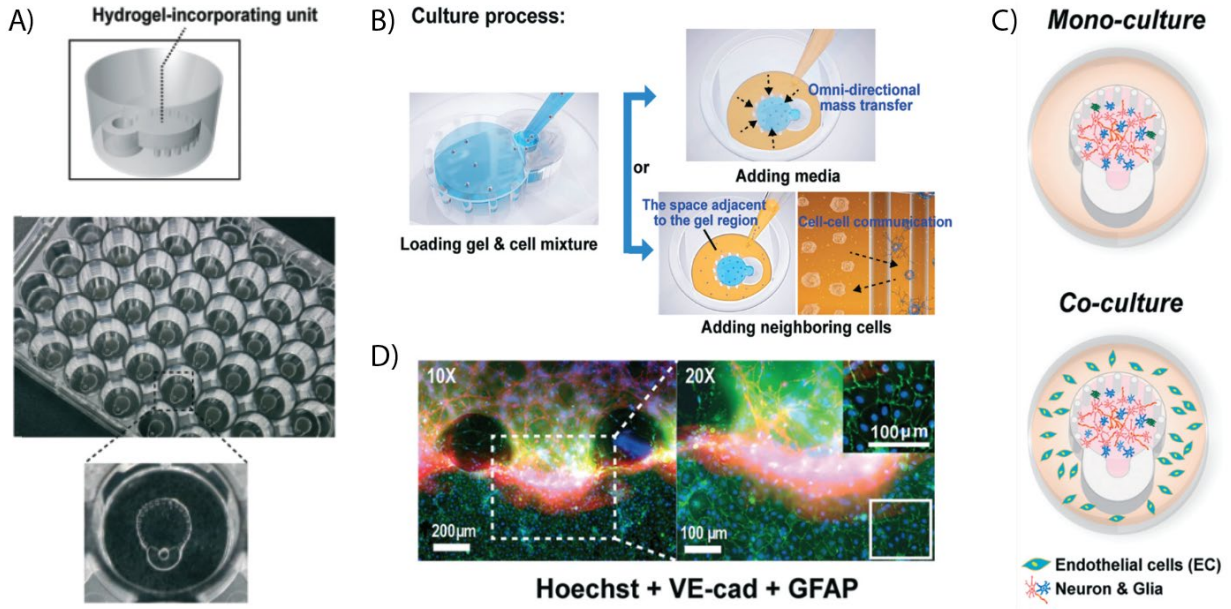

Figure 1.5. *Hydrogel Incorporating Insert* – A) Hydrogel inserts provide a high-throughput (48-well plate) 3D co-culture system. B) Cells imbedded in gel are seeded into the insert from the loading port, then neighboring cells are seeded in the surrounding space. C) Both mono and co-culture tissues are options. D) The inserts were used to produce a high-throughput Alzheimer disease model.

An example of a microfluidic well-plate insert with no channels was demonstrated by Y. J. Yu et.al. in 2018[21]. The advantage of an insert without channels is that operation complexity is reduced even further. To achieve this, a PDMS insert was designed with a central chamber circumvented by microposts (Fig. 1.5A). The chamber is filled with cell embedded in hydrogel from the top of the insert via the loading port (Fig. 1.5B). The PDMS microposts at the periphery of the hydrogel chamber pin the hydrogel within the device while still allowing molecular exchange from the 3D culture and the culture surrounding the device in the bulk of the well. This allows easy bulk media exchange with no perturbation of the 3D culture.

Designed to fit into 48-well plates, the inserts provide a quick tissue-modeling upgrade to standard well-plates (Fig. 1.5C.). To demonstrate the capability of the platform, they engineered a high-throughput neural disease model. Using previously developed neural progenitor cells, an Alzheimer's Disease tissue model was constructed in a 48-well plate, co-culturing the neural

progenitor cells with glial and endothelial cells (Fig. 1.5D). As proof, they were able to run a luciferase assay within the modified wells and observe a dose-dependent response using a plate-reader. As with the rail channel angiogenesis assay, such a technology could provide a cheap and useful alternative to animal models in neural disease and drug research.

PDMS inserts for immune response

One of the most recent studies utilizing a microfluidic well-plate insert was presented by F. Ellett et.al. earlier in 2019[22]. Like the low volume insert for endogenous signaling, it is another example of microfluidic engineers updating a previous device to increase ease of operation by a broader range of end users[51]. Unlike the low volume insert and the rail channel devices, the insert demonstrated in this study is a more traditional open microfluidic device made of PDMS. Micromolded from PDMS, it requires a glass bottom well-plate to which it can be plasma bonded. This does add a level of complexity since many non-engineering labs do not have easy access to an O_2 plasma treatment chamber, however, it is still vastly easier to operate than the previous design.

The device described by Ellet et.al. is meant to track and quantify the immune response of isolated human neutrophils in response to microbes in co-culture. The device consists of three main components: the main microchannel, the array of egg-shaped micro-chambers within the main microchannel, and the 10 μm square chemotaxis microchannel that connects the main channel to each micro-chamber (Fig. 1.6A). The cross-sectional area of the chemotaxis channel is important, being specifically designed to be large enough for bacteria to flow through freely, but small enough to prevent neutrophils from doing the same, forcing them to actively migrate toward the stimuli within the micro-chamber.

To set up the assay, bacteria are first loaded into the micro-chambers via the main micro-channel. Once a sufficient number of bacteria are loaded into the chambers, the main channel is thoroughly washed, removing only the bacteria present in the main channel because viscous forces

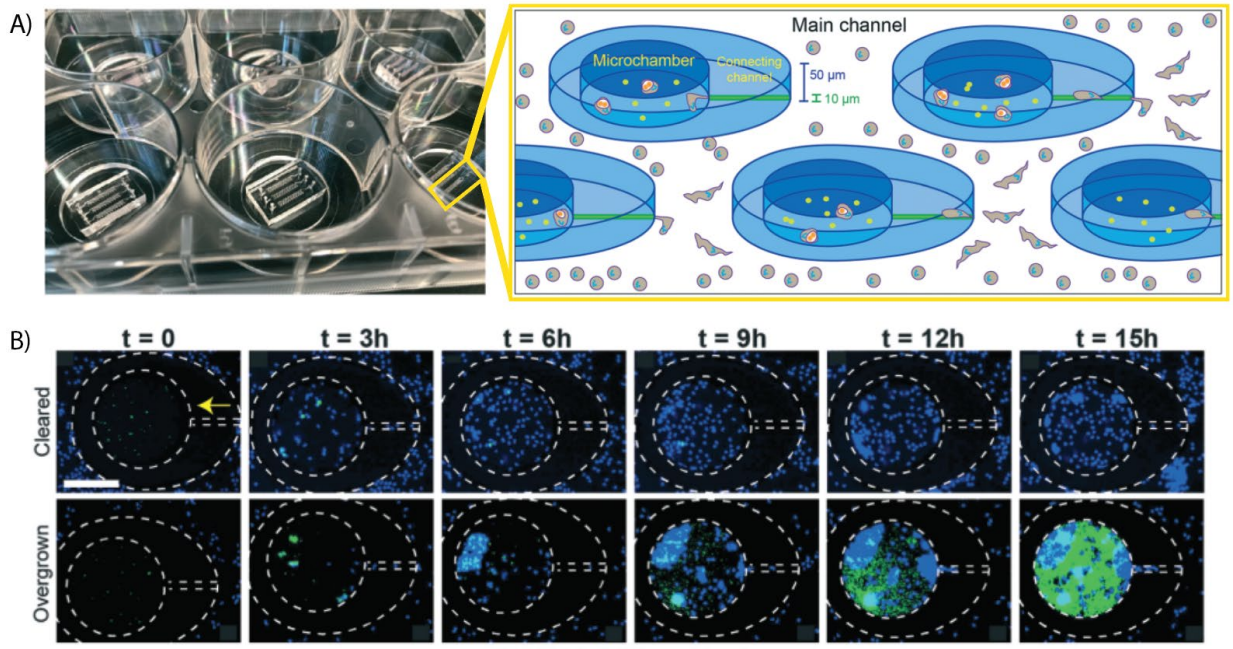

Figure1.6. *Immune Response Inserts* – A) Immune response assay inserts fit onto glass bottom well-plates, containing microchannels filled with dozens of microchambers. B) A cleared microchamber is one where neutrophils have eradicated the bacteria within the chamber, whereas an overgrown microchamber is where the bacteria proliferate faster than neutrophils can eradicate.

inhibit external perturbation of the contents within the micro-chambers. Once thoroughly washed, the main channel is seeded with isolated human neutrophils, initiating the immune response assay.

The device provides multiple readouts, giving insight into immune response. The first readout is neutrophil recruitment; do the neutrophils sense and migrate up the chemotaxis channel into the micro-chamber. The second readout provides a binary result – cleared or overgrown – on whether or not the recruited neutrophils are able to clear the micro-chamber of its pathogen within a set length of time (Fig. 1.6B). Staining the cells with specific markers provides a third readout where the various neutrophil microbial responses can be observed, such as phagocytosis, reactive oxygen species (ROS) secretion, and NETosis.

To characterize these readouts, Ellet et.al. ran immune response assays with neutrophils responding to increasing concentrations of two different bacterium -- *S. aureus* and *E. coli*. Once

characterized, they tested the device on neutrophils from six patients who had recently undergone major surgery. Three of the patients had developed sepsis, while the three others had not. They also had one healthy patient as a control. As established in characterization of the device, the healthy neutrophils were highly recruited to the micro-chambers and were able to fully clear every chamber. Interestingly, all of the non-septic neutrophils were unable to clear any chamber, but they appeared to be recruited better than the septic neutrophils. In their discussion the authors hypothesize different reasons for this intriguing result, but in broad terms it provides reason for further study using this well-plate adapter.

1.3 CONCLUSION

Microfluidics has long demonstrated impressive capabilities in high-throughput assays and tissue cultures. Over the last 20 years scientists have demonstrated a wide variety of ways to integrate microfluidics with established laboratory equipment – such as microscopes, plate readers, and liquid handling robots. Recently, a sub-area of microfluidic research has begun to characterize the capabilities of simple microfluidic well-plate inserts. Such devices mimic the concept first popularized by Transwell permeable inserts where well-plate tissue cultures could be easily upgraded to more complex co-culture systems. Five relevant studies were highlighted in this review, each providing unique evidence for how impactful well-plate inserts can be. In the future, some of these techniques could lead to commercially available inserts that provide high-through tissue models that are simple and cheap, while retaining relevant tissue complexity.

2. Interrogating bronchoalveolar lavage samples via automated exclusion-based analyte extraction

Jacob J. Tokar, Jay W. Warrick, David J. Guckenberger, Jamie M. Sperger, Joshua M. Lang, J. Scott Ferguson, and David J. Beebe (From work submitted to SLAS Technology)

While average survival rates for lung cancer have improved, earlier and better diagnosis remain a priority. One promising approach to assisting earlier and safer diagnosis of lung lesions is bronchoalveolar lavage (BAL), which provides a sample of lung tissue as well as proteins and immune cells from the vicinity of the lesion, yet diagnostic sensitivity remains a challenge. Reproducible isolation of lung epithelia and multi-analyte extraction has the potential to improve diagnostic sensitivity and provide new information for developing personalized therapeutic approaches. We present the use of a recently developed exclusion-based, solid phase extraction technique called SLIDE to facilitate analysis of BAL samples. We developed a SLIDE protocol for lung epithelial cell extraction and biomarker staining of patient BALs, testing both EpCAM and Trop2 as capture antigens. We characterized captured cells using TTF-1 and p40 as immunostaining biomarkers of adenocarcinoma (AdC) and squamous cell carcinoma (SCC), respectively. We achieved up to 90% (EpCAM) and 84% (Trop2) extraction efficiency of representative tumor cell lines. We then used the platform to process two patient BAL samples in parallel within the same sample plate to demonstrate feasibility and observed that Trop2-based extraction potentially extracts more target cells than EpCAM-based extraction.

2.1 INTRODUCTION

Lung cancer is the number one cause of cancer related deaths in the United States[52]. Improved early diagnosis and ability to stratify patients and match them to effective treatment options is critical to improving patient outcomes. Currently lung cancer is identified using a CT scan and specific diagnosis is made via biopsy and histology. One type of biopsy, percutaneous needle biopsy, provides precise sampling of a tumor for histology to differentiate between the various subtypes of lung cancer. However, percutaneous lung biopsies are associated with significant risk to the patient with some studies finding that patients have an 8-35% chance of pneumothorax (collapsed lung)[53–56]. Bronchoscopy methods, such as the bronchoalveolar lavage (BAL), are considered to be safer than percutaneous techniques given they avoid puncturing the pleural membrane, but are limited by sensitivity[57]. During a BAL, saline is instilled in a region of the lung where the lesion is, and is collected back providing cells, proteins, and lipids (Fig. 2.1A). The BAL can sometimes yield a diagnosis. However, there are multiple challenges to successful diagnosis via BAL.

First, it is often difficult to sample small lesions in the periphery of the lung using normal bronchoscopes due to their size and difficulty of accurate navigation to the lesion site. Thus, smaller bronchoscopes[58], endobronchial ultrasound (EBUS) and more advanced navigation procedures like electromagnetic navigation (ENB) are now being used[59]. Although it is safer than percutaneous biopsies, the BAL sampling procedure is rarely used for accurate diagnosis of cancer. However, if performed immediately after the regularly scheduled bronchoscopic sampling, it may be able to provide a significant amount of additional tissue (e.g., normal epithelium, stroma, and immune cells) than typically acquired via BAL (Fig. 2.1B). This additional tissue may be important in lung cancer studies. Lastly, we currently lack robust approaches to examine these cells and other factors within the saline wash solution that results from a BAL.

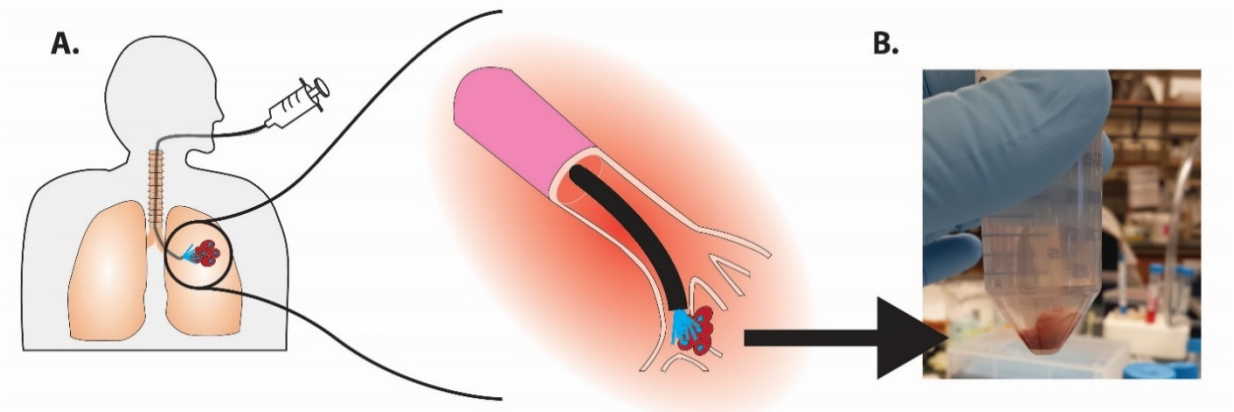

Figure 2.1. *BAL Sampling* – Bronchoalveolar lavage sampling (BAL) is used to sample lung lesions in a less invasive manner than traditional percutaneous needle biopsy method. (**A**) A bronchoscope is guided down the bronchial tree, where it is used to wash the lesion site with saline. The saline is collected and its contents are analyzed. (**B**) BAL sample after centrifugation in a 50 mL conical tube. BAL samples are very heterogenous, containing cells, proteins, and extracellular matrix, making it difficult to process and analyze.

Recent advances in Exclusion-based Sample Preparation (ESP™) could allow more information to be obtained from a BAL sample. ESP extraction makes use of paramagnetic particles (PMPs) in a different way than traditional PMP-based solid phase extraction (SPE) assays. In traditional PMP-based SPE, PMPs are coupled with magnetic force to hold a sample fraction in place while the remaining fluid is removed or washed away, but with ESP it is the analyte that is removed from the bulk fluid. This allows highly efficient and gentle sample processing as well as multi-analytical extraction from a single sample[60,61]. Here we utilize one embodiment of ESP, called Sliding Lid for Immobilized Droplet Extraction (SLIDE), to leverage these advantages for the processing of BAL samples from lung cancer patients.

The SLIDE multi-analyte extraction platform was specifically designed to facilitate automation[62]. The SLIDE platform is applied here to allow parallel extraction of lung epithelial cells from patient BAL samples. Broader, more efficient processing using this platform can allow more clinically useful information to be gleaned from the less invasive BAL. Further, the method helps to address current

challenges in downstream histological analysis given it is well-suited for cell isolation from complex samples.

2.2 MATERIALS AND METHODS

2.2.1 *Device Fabrication*

A custom extraction plate was fabricated from cyclic olefin copolymer (COC) resin using hot embossing techniques described in Young et al[63]. An aluminum mold was made using an automated CNC mill[64]. The plate is designed with a 270 µL input well, 60 µL wash well, and 40 µL output well. Given the SLIDE automation has standard well-plate geometries pre-programmed into its software, the dimensions of the extraction plate were designed to resemble that of a 96 well plate.

2.2.2 *Gilson Pipetmax Custom Automation*

The Gilson Pipetmax was fitted with a special pipette head that houses neodymium magnets (K&J Magnetics). The magnets can be moved up and down by giving the robot the commands to aspirate or dispense. The magnets are put in the lowered position to attract magnetic beads to the pipette head to remove the beads from a sample well. The magnets are raised to allow a separate magnet below the sample plate to recollect the beads into a desired sample well downstream (Fig. 2.2B). The operation of this specialized pipette head was programmed using the TRILUTION micro Protocol Builder software provided by Gilson Inc.

2.2.3 *SLIDE Protocol*

The protocol consists of three steps: 1) Loading of the sample, 2) binding of PMPs to target analytes, 3) extraction of target analytes, 4) washing of the extracted sample. Briefly, all samples

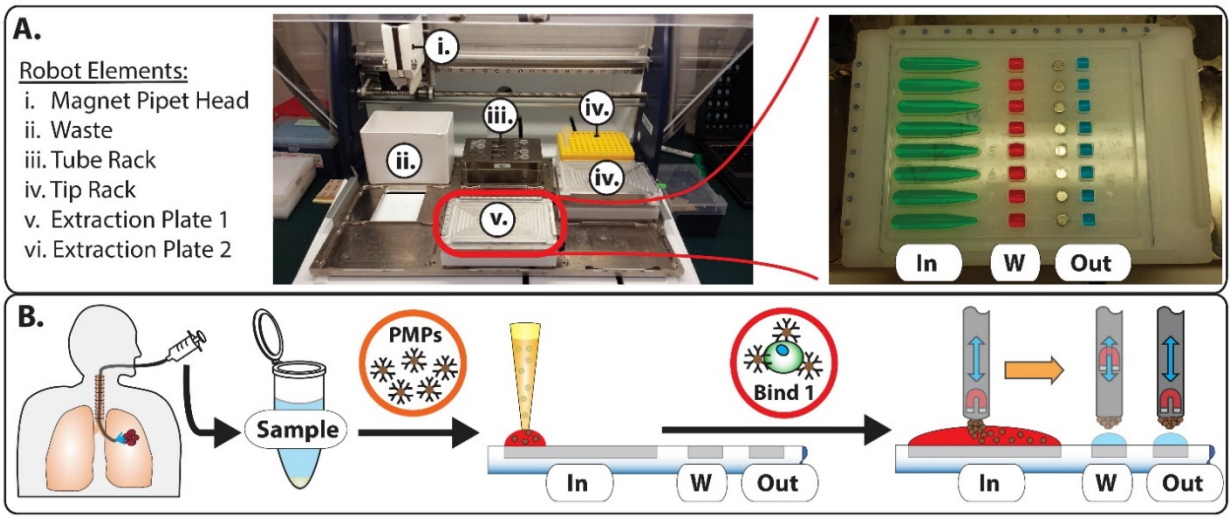

Figure 2.2. *Automated BAL Processing* – A) The robot deck elements include a waste bin, a tube rack for samples and buffers, a tip rack, and two extraction plates. Each extraction plate consists of an input (In), a wash (W), and an output well (Out). B) Samples are extracted via bronchoalveolar lavage and preprocessed with buffers and paramagnetic particles (PMPs). Samples are then placed in the tube rack, where the robot protocol distributes them to an input well where they are allowed to bind for 30 min at room temperature. Afterward, the modified magnetic pipet head is moved into position at the input well with its magnets in the bottom position. The magnet head is then moved slowly along the length of the well, extracting PMPs along with any cells bound to them. After collecting PMPs from the input, the magnet head moves them to the wash well, which has magnets embedded just below it in the plate platform. The magnets in the modified pipet head are then raised into the top position, allowing the PMPs to be pulled down into the well by the now stronger magnetic force of the embedded magnets. The plate is slid until the output well is positioned above the embedded magnets and the wash well is briefly mixed. Next, the magnets in the pipette head are lowered back to the bottom position, and the magnet head is positioned at the wash well to collect the PMPs, which are then moved to the output well and mixed in the same fashion as previously used for the wash well. Further details of SLIDE processing are contained in ref. 11. Downstream processing is performed manually off chip.

were prepared in a solution of 1x PBS, 1% BSA, 1mM EDTA, and PBST to bring the sample to a volume of 300 µL. Immediately prior to processing, PMPs are added to the sample tubes and placed in the tube rack of the robot for SLIDE processing (Fig. 2.2A). The sample is incubated in the input well with the beads for 30 mins. The magnetic head is then used to transfer the cells to the wash well. The wash well is pipetted to mix and resuspend the sample allowing cells that were carried over non-specifically to fall to the bottom of the well. The bound cells are then transferred to the output well where the sample can be collected for downstream analysis. The protocol takes

approximately 60 minutes to complete. A step-by-step illustration of the protocol is provided in Fig. 2.2B.

2.2.4 *PMP Preparation*

PMPs (ThermoFisher, 11205D) were washed with PBST and coated in a 1.5µg/mL solution of capture antibody (Biotinylation Kit - Thermo Fisher D20655, EpCAM - R&D systems AF960 or Trop2 - R&D systems AF650) for 30-60 minutes at room temperature (RT) in a benchtop shaker, then they were washed again with PBST to remove any unbound antibody.

2.2.5 Cell Line Culture

H358, A549, and H226 human lung cancer and THP-1 human monocyte cell lines were cultured according to ATCC recommendations in RPMI 1640 media with 10% FBS and 1% Pen/Strep added. When passaging, the adherent lung cancer cells were dissociated with either Trypsin-EDTA (0.05%) or using a cell scraper. Culturing in suspension, the THP-1 cells were simply split as they became confluent.

2.2.6 Cell Line Labeling and Extraction

For extraction studies, human lung cancer cell lines and THP-1 human monocyte cell line were fluorescently labeled with 1.6 µM Calcein AM (ThermoFisher, C3100MP) and CellTracker™ Red (ThermoFisher, C34552) respectively, at 37°C for 15 min followed by one wash. It has been shown that epithelial cells make up between 0.05-1.5% of the cells recovered in BAL[14]. To replicate this cell fraction, 10,000 cells of the cancer cell line population were spiked into a sample of 1,500,000 THP-1 monocytes giving an experimental epithelial fraction of 0.67%. These cell line samples were then processed according the SLIDE protocol.

2.2.7 Patient Sample Extraction and Target Cell Identification

Primary samples were acquired via bronchoalveolar lavage, guided by electromagnetic navigation, from two patients suspected to have lung cancer. The bronchoscope was navigated to within millimeters of the lesion site. First, forceps and brush biopsies were collected and sent to pathology and cytology respectively. A BAL was then performed. During the BAL, four 20 mL aliquots of saline were instilled and collected, each into a syringe; approximately 50% of the instilled aliquot was returned upon collection. Samples were then processed in a similar fashion as Pollock et. al[65]. Patient BAL saline samples were twice centrifuged at 500 rcf for 10 min and resuspended with DMEM containing 10% FBS and HEPES buffer. Some BAL samples contained excess mucous and extracellular matrix to the point where pipetting was severely hindered, even with large orifice pipettes. In cases such as these the sample was washed through a 100 μm cell strainer (Corning Inc., 352360). The samples were then fixed in 4% PFA for 15 minutes, washed and resuspended in 1mL of PBS + 1% BSA. Each of the two patient samples used in this study contained a large cell/tissue pellet, so a 200 μL aliquot of each was used for extraction and the remaining sample was saved at 4°C for later studies. The 200 μL aliquot was then used for processing according the SLIDE protocol. In total, processing, imaging, and analyzing of patient samples takes approximately 24 hours to complete.

2.2.8 Calculation of Cell Line Extraction Efficiency

Extraction efficiency is calculated as the number of cells that were identified via microscopy in the input and output wells of the SLIDE extraction plate then dividing the output count by the combined total. Similarly, the ability to extract cell aggregates, as opposed to individual cells, was also quantified by counting the number of aggregates in the input and output wells of the device. Tumor cells were identified post-extraction using FIJI image analysis software[15] by automated detection and counting of fluorescently labeled cells (see Cell Line Labeling and Extraction).

2.2.9 Immunohistochemistry

To verify EpCAM expression, all three cell lines were fixed (15 mins in 4% PFA) and fluorescently stained for EpCAM expression. To stain, approximately 25 x 10^3 cells were incubated at room temp for 60 min with a 10 μg/mL solution of primary goat anti-human EpCAM IgG (R&D Systems, AF960) in PBS. The cells were washed and then incubated at room temp in a 10 μg/mL Alexa Fluor 568 donkey anti-goat IgG (Thermo Fisher, A-11057) and Hoechst (Molecular Probes, H1399) in PBS solution for 30 min and then washed and imaged on a fluorescent microscope. Trop2 expression in cell lines was verified in the same fashion using a 1:50 concentration of mouse anti-human Trop2 PE (Fisher Scientific, BDB564837).

All extracted cancer cells underwent the same intracellular staining protocol for lung cancer markers, TTF-1 and p40. Extracted cancer samples were fixed with 4% PFA and permeabilized with 0.2% Triton X-100. Mouse anti-human TTF1 (Abcam, ab72876) and rabbit anti-human p40 (EMD Millipore, ABS552) were diluted to a 10μg/mL concentration in PBS. Samples were incubated at 4°C overnight in the diluted antibody solution. They were then washed and incubated for 60 minutes at RT in a 10μg/mL secondary antibody solution of Alexa-fluor 488 anti-mouse (ThermoFisher, A-11029) and Alexa-fluor 568 anti-rabbit (ThermoFisher, A-11036). The samples were washed again and incubated for 30 minutes at RT in a solution of 1:120 Hoechst and 1:30 of Alexa-fluor 647 anti-human CD45 (Biolegend, HI30). Samples were washed a final time and then fluorescently imaged.

2.2.10 Immunostaining Fluorescence Quantification

Cells were quantified using multi-channel fluorescence microscopy followed by image analysis in the JEX image analysis program (www.github.com/jaywarrick/JEX)[66]. Briefly, for cell lines, images were background subtracted and cell locations were determined by finding fluorescence maxima corresponding to the channel for Hoechst nuclear staining within an image. These coordinates were

then used to quantify the intensity in the other imaging channels by measuring the mean fluorescent intensity within a 6.5 μm diameter circular region around each maxima. Given the additional complexity of the patient samples compared to cell lines, a modified JEX workflow was used. Following background subtraction, filtering and thresholding was performed on the nuclear channel to define separable regions for each cell. The integrated fluorescence intensity of these regions was quantified in each fluorescence channel. During analysis of fluorescence, "Ln" refers to the natural logarithm.

2.3 RESULTS

Cell lines provided reproducible samples with which to characterize the performance of the SLIDE platform in terms of cell extraction and immunostaining. The protocol was then applied to patient samples to demonstrate feasibility.

2.3.1 Cell Line Extraction

The efficiency and specificity of epithelial cell extraction were quantified using H358, A549, and H226 cell lines, which represent high, moderate, and low/negligible EpCAM expressing tumor cells, as shown in Fig. 2.3A-B. The fluorescence intensity density plots show three distinct populations of cells. Fig. 2.3C shows that even cells with moderate EpCAM expression like the A549 cells can be robustly extracted. Although a slight drop in capture efficiency is observed when compared to the high expressing H358 cells. The non-EpCAM expressing H226 cells had an average extraction efficiency of 2.6% (Fig. 2.3C). In terms of purity, the samples started with 150 monocytes per tumor cell, whereas afterward, the H358 sample had 0.8 ± 0.14 monocytes per tumor cell while the A549 sample had 0.9 ± 0.3 monocytes per tumor cell. Thus, tumor cell sample purity was enriched by greater than 150-fold.

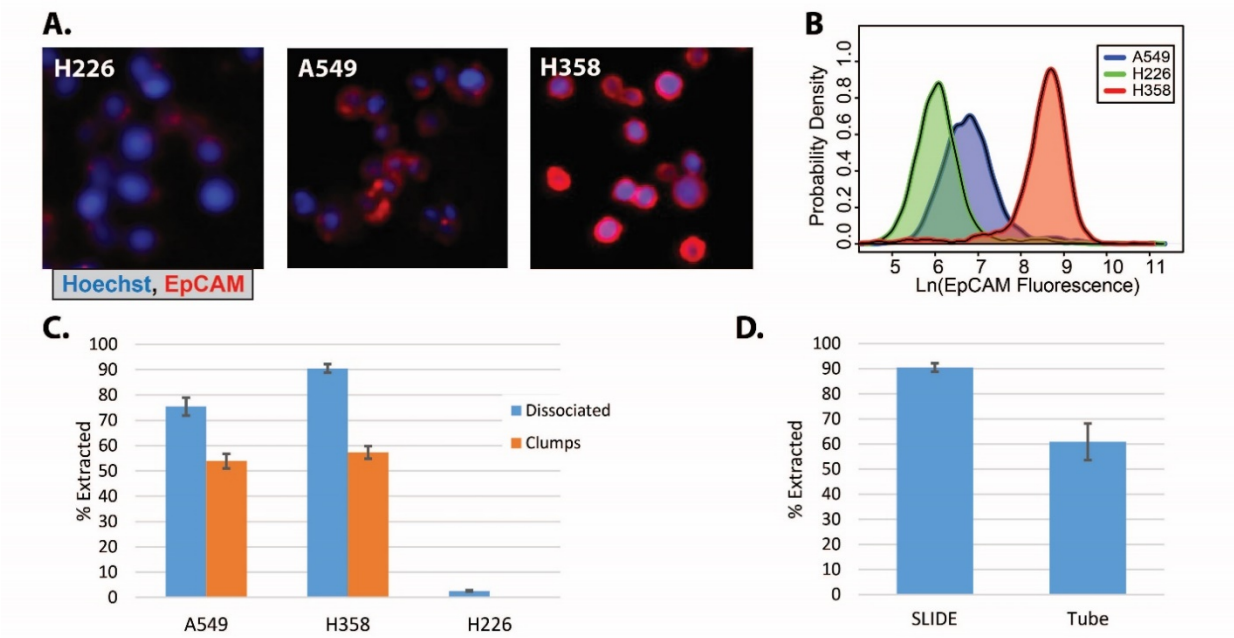

Figure 2.3. *Cell Extraction via EpCAM* – A) Representative images (identically treated) of EpCAM expression in H358, A549, and H226 cells. B) A probability density plot of the natural log of EpCAM fluorescence in each of the three cell lines. C) Extraction efficiency of cell lines using EpCAM. The EpCAM-positive cell lines (H358 and A549) were spiked into separate fractions of a cell suspension of THP-1 monocytes for a total of eight technical replicates of each condition. Extraction efficiency was compared with that of the H226 cell line, which moderately expresses EpCAM. Extraction efficiency of cell clumps is also shown. D) Comparison of extraction efficiency of H358 cells in phosphate-buffered saline using SLIDE versus standard tube-based paramagnetic particle extraction.

A common characteristic of BAL samples is the presence of large clumps of target cells that have been sloughed off the tumor during the BAL procedure. To test how the SLIDE platform performs when target cells are part of larger aggregates the cell lines were scraped off their culture plate rather than being dissociated with Trypsin to promote suspension of cell aggregates or fragments of cell sheets. Fig. 2.3C shows that greater than 50 percent of the clumps in samples were extracted. Clumps were defined as aggregates of more than 2 cells.

The extraction efficiency of the SLIDE platform was also compared to manual extraction using the traditional approach PMP-bound cells in tubes, magnetic tube racks, and pipet-based washes. The SLIDE platform isolated H358 cells with~90% efficiency compared to ~60% percent efficiency with the traditional method (Fig. 2.3D).

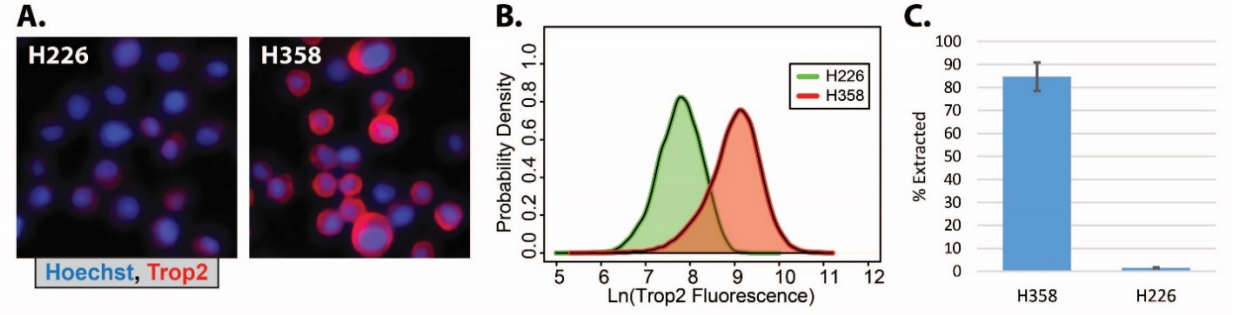

Figure 2.4. *Cell Extraction via Trop2* – A) Representative images (identically treated) of Trop2 expression in H358 and H226 cells. B) A probability density plot of the natural log of Trop2 fluorescence in each of the two cell lines. C) Extraction efficiency of the cell lines using Trop2.

As part of characterizing capture using Trop2, Trop2 expression of the H226 and H358 cells was measured via fluorescence microscopy. H226 cells exhibited low fluorescence compared to the H358 cells (Fig. 2.4A-B). In concordance with Trop2 expression, almost 85% of the H358 cells (high Trop2) were captured, while less than 2% of the H226 cells (low Trop2) were captured (Fig. 2.4C).

2.3.2 Biomarker Staining

The staining protocol for analyzing p40 and TTF-1 expression in patient samples was characterized using the H358 and H226 non-small cell lung cancer cell lines. Fluorescent IHC shows that H358 cells have a higher TTF1:p40 expression ratio than H226 cells, mirroring what is seen clinically (Fig. 2.5A). This difference is enough that two distinct curves are produced when the expression ratio is illustrated in a density plot (Fig. 2.5B). Note the localization of TTF1 to the nucleus of the H358 cells compared to the H226 cells.

2.3.3 Patient Samples

This study looked at two patient samples acquired via BAL and processed as described above. These samples, referred to as Patient 1 and Patient 2, were strained using a 100 μm cell strainer to remove unwanted mucous. The samples were then fixed in 4% PFA for 15 minutes, washed and

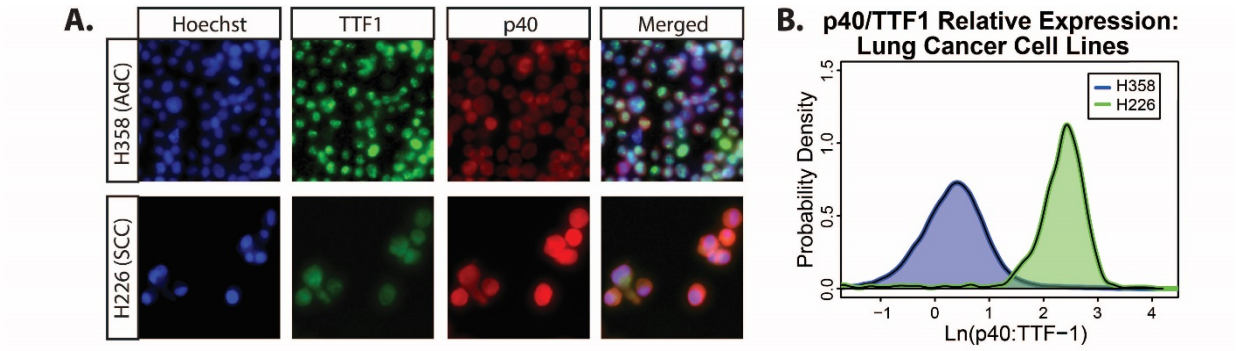

Figure 2.5. *Cancer Diagnostic Cell Line Controls* – A) Fluorescent immunohistochemistry images of H358 and H226 cells with channels split and merged. B) The ratio of TTF1 and p40 fluorescent intensity was determined for each cell; the log of the ratio was then taken and plotted on a density curve.

resuspended in 1 mL of PBS + 1% BSA. Both samples contained a large cell/tissue pellet, so a 200µL aliquot of each was used for extraction and the remaining sample was saved at 4°C for later studies. Each sample aliquot was split in half, adding 25 µL of anti-EpCAM coated PMPs to the first half of each sample and adding 25µL of anti-Trop2 coated PMPs to the remaining 100µL respectively. The two samples split into two extraction conditions resulted in four parallel extractions. The patient samples were processed with the SLIDE and stained just as the cell line controls were in Fig. 2.6.

Given the BAL sample contains cell debris and non-target cells, even after extraction, multiple criteria were used to define 'target' lung epithelial cells for subsequent analysis. The target cells must be Hoechst^{+} and CD45^{-} and generally exhibit cell-like morphology in brightfield. For example, a representative cancer cell that is TTF1^{+} and p40^{+}, and CD45^{-} is shown in Fig. 2.6A and indicated using a white arrow. While the cancer cells were purified, there were still leukocytes that were carried along with the extracted sample fraction as it was moved from the input to the output much like the clump of CD45^{+} leukocytes identified by the pink arrow in Fig. 2.6A. There were noticeably more cells captured from Patient 2 BAL than Patient 1. The CD45^{-} cell counts in Fig. 2.6B show that over 230 more target cells were extracted from Patient 2 than Patient one for both capture

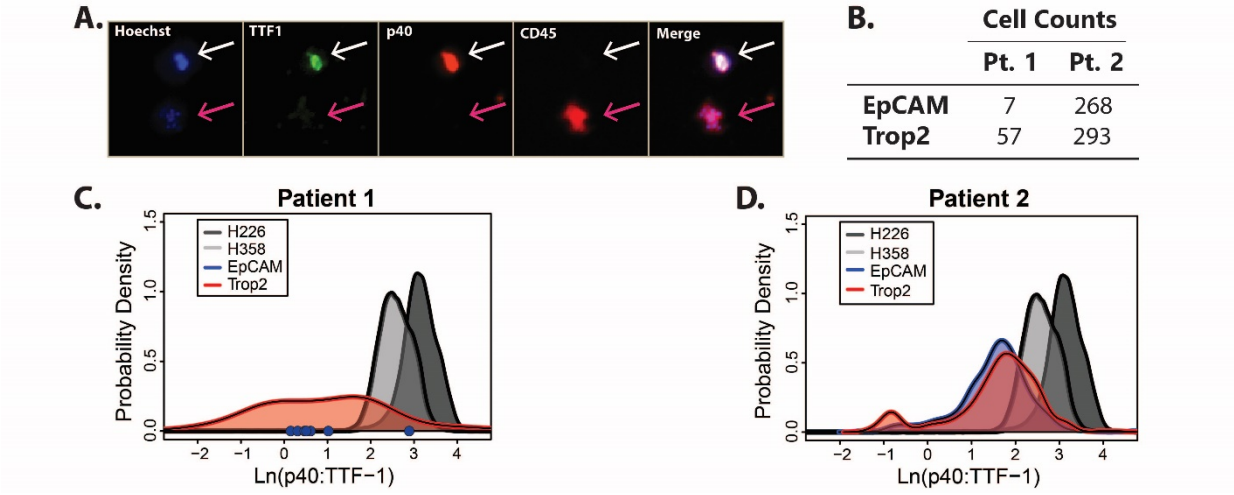

Figure 2.6. *Patient BAL Cell Extraction Staining* – A) An example image from a patient sample that has been processed with the automated SLIDE protocol and stained for TTF1, p40, CD45, and Hoechst. A cancer cell (TTF1 and p40 positive, white arrow) and a clump of leukocytes (CD45 positive, pink arrow) can be seen in this image. B) Number of target cells extracted from each patient (Pt.) sample aliquot using EpCAM and Trop2 capture antigens. C & D) Density histograms of log(p40:TTF1) for patient target cells and associated cell line controls. EpCAM capture for Pt. 1 produced too few cells to make a histogram. Instead, the seven cells are plotted as blue dots on the x-axis.

antibodies. What is also interesting is that in both cases Trop2 isolation captured more target cells than EpCAM.

H358 and H226 cells were stained in parallel with the patient samples as lung AdC and SCC controls respectively. As before, a density plot was generated from the log of the fluorescence intensity ratio of p40:TTF1. Since so few cells were captured from Patient 1 using EpCAM extraction, the individual cell ratios were plotted as blue dots on the x-axis of Fig. 2.6C, concentrating between a 0-1 log ratio. The bulk of the cells captured using either technique on Patient 2 are centered around a log ratio of ~1.8, but there was a small subpopulation of cells captured using Trop2 that express greater TTF1 than p40 (Fig. 2.6D).

Given the limited number of patients, conclusions cannot be made regarding a relationship between patient/disease characteristics and results. However, a short summary of the patient information is as follows. Patient 1 was diagnosed with non-small cell carcinoma, not otherwise

specified (NSCLC-NOS). Bronchoscopic biopsy was used to verify diagnosis of the 33 mm diameter mass in the right upper lobe. In patient 2, bronchoscopic biopsy of an 18 mm diameter left upper lobe nodule revealed adenocarcinoma.

2.4 DISCUSSION

The SLIDE platform offers the potential to improve the quality and quantity of diagnostic information that can be obtained from highly complex and heterogenous BAL samples from lung cancer patients. However, the potential benefits of the SLIDE technology for BAL sample analysis have yet to be highlighted. Towards this goal, we first demonstrated and characterized an automated SLIDE protocol for the extraction and staining of cell lines and applied it to analyze BAL samples.

Extraction characterization was performed using conditions and cell lines intended to recapitulate important aspects of BAL samples and the disease. Target cells were spiked into and extracted from suspensions of THP-1 monocytes to mimic the prevalence of monocytes often observed in BAL samples. A typical BAL sample is made up of anywhere from 80-95 percent alveolar macrophages[67]. We chose to explore the use of 2 different capture antigens for cell extraction. Although, the standard approach for capturing epithelial cells is to target EpCAM, it can be expressed moderately in normal lung epithelia and variably in different types of lung cancer[68]. Thus, not all target cells are expected to express EpCAM. A potential alternative capture antigen for lung epithelia is Trop2. Much like EpCAM, Trop2 expression has also been shown to be moderate in normal lung tissue while variably present in malignant tissues (The Human Protein Atlas; www.proteinatlas.org). Another reason these two capture proteins are significant is that they appear to be related to the disease in slightly different manners, as evidenced by their different prognostic values[68–71]. Thus, EpCAM and Trop2 were chosen for our initial demonstration of the

platform because they are not only useful capture targets but could also have significant impact as prognostic biomarkers. We also chose cell lines representative of the two most frequent types of lung cancer. NSCLC makes up over 80 percent of lung cancer cases[72]. Within that group, AdC and SCC are the most common subtypes. The H358 cell line is an established lung AdC and H226 is an established lung SCC. Clinically, lung AdC and SCC are differentiated from one another using transcription factors TTF1 and p40 as IHC markers, thus informing our choice of antibodies for staining characterization. AdC overexpresses TTF1 while p40 is overexpressed in SCC (Fig. 2.5)[73].

We first demonstrated the specificity and efficiency of the SLIDE platform for EpCAM-based tumor cell extraction using cell lines. We performed EpCAM immunostaining and single-cell fluorescence analysis to establish the relative abundance of the capture antigens on each of the target cell lines. Results demonstrate a large difference in the average expression amongst the different cell lines as well as the single-cell heterogeneity of the expression (Fig. 2.3A-B). It is expected that expression level should correspond well with extraction efficiency. The platform was able to extract the highly and moderately EpCAM expressing cell lines with roughly 90 and 75% efficiency, respectively, compared to 2.6% for the H226 cell line that had very low relative EpCAM expression (Fig. 2.3C). We also quantified the ability to capture cell clumps using EpCAM given that, in our experience, BAL samples contain many cell aggregates or fragments of epithelial sheets of variable size. Also, the biomarker expression of cells within such aggregates could spur interesting observations; thus, avoiding unnecessary dissociation of aggregates is preferred. While there was a significant drop as compared to the capture of individual cells, it remains encouraging that more than half of the aggregates were isolated (Fig. 2.3C). Lastly, we compared the extraction efficiency of the SLIDE-based platform to a standard tube-based PMP protocol where PMP-bound samples are placed in a tube in a magnetic tube rack to perform washes. While the standard method is well established and effective in many scenarios, the SLIDE protocol described here exhibited a 20-30% increase in cell extraction along with reduced variability from one sample to the next (Fig. 2.3D).

We suspect this is due to the gentler extraction and washing process of the SLIDE technique. Overall, the high capture efficiencies for H358 and A549 cells and the correspondence of the EpCAM expression levels and capture efficiencies suggests EpCAM capture is both efficient and specific using the SLIDE platform.

The second capture antigen, Trop2, was also tested using lung cancer cell lines. The platform performed as expected, extracting the high Trop2 expressing H358 cells with almost 85% efficiency and the low Trop2 expressing H226 cells with 1.52% efficiency (Fig. 2.4). The Trop2 extraction of both the H358 and H226 lung cancer cell lines using Trop2 appeared to be nearly as efficient as EpCAM extraction. Again, we observe a high capture efficiency and a high correspondence between expression levels and capture efficiency, indicating Trop2 capture is also specific and efficient using the SLIDE platform.

After establishing performance of EpCAM and Trop2 extraction, we demonstrated the ability of the SLIDE platform to process actual patient BAL samples (Fig. 2.6). In this brief demonstration, we processed two patient samples in parallel on the same day, on the same sample plate, performing both EpCAM and Trop2 capture on each sample. After extraction, we manually stained the cells for Hoechst (nuclear stain), CD45 (a marker of hematopoietic lineage), p40, and TTF-1. In parallel, we also stained H358 and H226 cells to account for day-to-day variability in the manual staining procedure and enable more robust interpretation of results. Both samples showed a noticeably lower p40:TTF-1 ratio than the cell line controls. Both samples also displayed a higher number of target cells when extracted using Trop2 compared to EpCAM. Patient 2 had enough cells with both EpCAM and Trop2 capture for creating comparing density histograms of the two capture methods. Overall, the histograms are largely consistent, in keeping with EpCAM and Trop2 capture results for H358 cells during characterization with cell lines. However, there may also be an additional small population of low p40:TTF-1 ratio target cells that were extracted using Trop2 that were not extracted using EpCAM. This observation is consistent with clinical observations that individual

patients can have cancers made up of both AdC and SCC cells. However, to see if such a trend continues would require much larger data set and is complicated by the fact that normal epithelium will also most likely be present in samples as well. Lastly, the distributions of the Trop2 captured cells of Patient 1 and Patient 2 appeared to show different levels of heterogeneity. The distribution for Patient 1 was relatively well distributed while Patient 2 showed noticeable peaks in the distribution, highlighting the heterogeneity that is likely to be expected patient-to-patient. Overall, results demonstrate the automated platform is able to perform specific and efficient parallel cell extractions from complex and heterogeneous patient BAL samples, enabling isolation of different subsets of target cells for downstream analysis.

Although results of patient sample are promising, they also highlight topics to address moving forward. One topic is the choice of capture antigens. For example, as part of extraction characterization with cell lines, we observed that EpCAM and Trop2 are not effective at extracting H226 cells; thus, it is likely that additional capture antigens will need to be explored. One such protein is CAIX, which has been found to be expressed in a high percentage of lung SCC[74,75]. Capture antigens might also be linked more specifically to treatment options. For instance, therapeutic targets like EGFR and FGFR mutations are exclusively expressed in lung AdC and SCC respectively[76]. Furthermore, whether the such extractions should be performed in parallel on separate fractions of a sample or in sequence on a single sample should also be considered.

Automation allows for more objective and repeatable parallel processing, which allows for more nuanced interpretation of parallel sample results. However, the SLIDE methodology is also amenable to sequential extraction, hence the additional extraction plate shown in Fig. 2.2A. Therefore, future development to automate sequential capture could allow different cell populations to be isolated in variable sequence from the same input well, to tease apart the nature and overlap of the populations captured with each antigen. Development of such approaches will need to address the potential for target cells to express multiple capture target antigens and

require optimization of the order in which the different capture antibodies are introduced. Currently, sequential capture would require multiple plates; however, alteration of the SLIDE apparatus, such as additional pairs of wash and output wells, could enable sequential capture on a single plate. It is also possible that multiple antibodies either on the same beads or on different beads mixed together can be used to simultaneously capture multiple populations, such as for removal of background cells.

Another topic to address moving forward is the automation of both extraction and downstream readouts. Currently only the extraction of cells has been automated, yet the platform is also well-suited for extraction of other analytes such as proteins and nucleic acids. The platform is also amenable to automation of immunostaining procedures, which could prove important for continued development of the immunostaining analysis initiated here. In the present study, manual immunostaining was used for downstream analysis; however, there was a noticeable increase in the p40:TTF-1 ratio in the cell line controls (Fig. 2.5-6). This increase could indicate the presence of significant biological variability in the cell lines or the need for further optimizing the staining protocol to remove day-to-day variability in the manual staining process. Although, it is still possible to perform relative qualitative comparison of the parallel processed patient results obtained here, optimization will be needed to make immunostaining and patient comparisons more quantitative to improve confidence in the biological interpretation of results. Moving forward, we plan to sample a normal and diseased portion of each patient. This will provide a more direct and patient-specific normal control for assay endpoints. Further, integration of staining procedure into the automated protocol could not only aid in optimization but improve repeatability. Similarly, integration of additional endpoints, such as extraction of soluble factors and nucleic acids will also strengthen this automated platform for BAL analysis, allowing comparison of concordant metrics for more robust interpretation of results and an increased ability to leverage BAL samples for safer and more robust diagnosis of lung cancer.

2.5 CONCLUSION

In conclusion, BAL is unique and promising cancer sampling technique, but is currently less precise than percutaneous techniques for purposes of diagnosis, in part due to the complexity and heterogeneity of the sample itself. However, being heterogeneous in nature, the sample also provides other analytes such as immune cells, cytokines and lipids that might provide additional clinically relevant information as well as basic insights into the tumor microenvironment. Here we have demonstrated a new approach to tumor cell extraction from BAL samples that has the potential to leverage these additional sample components. We characterized the ability of the platform to provide specific and efficient capture of cell lines from monocyte rich backgrounds and showed feasibility of performing automated parallel processing of patient BALs for downstream immunostaining endpoints. We envision that future iterations of the technology will involve exploration of alternative capture antigens that could potentially be coupled with informative markers of diagnosis and therapy. Likewise, we imagine that further integration of downstream processing will enable more robust analysis from this promising and rich yet complex and heterogeneous type of tumor sample for lung cancer patients.

3. Pairing microwell arrays with an affordable, semi-automated single-cell aspirator for the interrogation of circulating tumor-cell heterogeneity

Jacob J. Tokar, Charlotte N. Stahlfeld, Jamie M. Sperger, David J. Niles, David J. Beebe, Joshua M. Lang, and Jay W. Warrick (to be submitted to SLAS Technology)

Comprehensive analysis of tumor heterogeneity requires robust methods for the isolation and analysis of single cells from patient samples. An ideal approach would be fully compatible with downstream analytic methods, such as advanced genomic testing. These endpoints necessitate the use of live cells at high purity. The Lab-on-a-Chip field has produced a multitude of CTC enrichment technologies, but many of those perform bulk sample enrichment and are not, on their own, capable of single cell interrogation. To address these needs, we developed an affordable Semi-automated Single Cell Aspirator (SASCA) to further enrich rare cell populations from a specialized microwell array, per their phenotypic markers. Immobilization of cells within microwells, integrated with a real-time image processing software facilitates the detection and precise isolation of targeted cells that have been optimally seeded into the microwells. Here, we demonstrate the capabilities of the platform through the aspiration of target cells from an impure background population, where we obtain purity levels of 90-100% and demonstrate the enrichment of the target population with high quality RNA extraction and transcriptomic analysis. A range of low cell numbers were aspirated using SASCA before undergoing whole transcriptome and genome analysis, exhibiting the ability to obtain endpoints from low-template inputs. Lastly, circulating tumor cells from patients with castrate resistant prostate cancer were isolated with this platform and confirmed the utility of this method for rare cell isolation. This platform satisfies a need for an affordable option to isolate single cells or highly purified subpopulations of cells to probe complex mechanisms driving disease progression and resistance in patients with cancer.

3.1 INTRODUCTION

Rare cell populations can have a tremendous influence in disease development, progression, and resistance. Isolation and analysis of rare cells offers a method to study the pertinent cell-to-cell heterogeneity that may harbor drivers of disease progression or treatment resistance[77,78]. However, rare cells (e.g., circulating tumor cells, CTCs) are generally difficult to isolate at high purity[79]. The Lab-on-a-Chip field has produced many iterations of rare cell enrichment devices, leveraging both physical and biological phenomena[80]. However, the majority of these platforms are bulk enrichment techniques, and significant levels of background or contaminating cells remain after isolation. While these methods can provide an averaged measure of cells found in the entire sample, the presence of contaminating cells can directly alter results and interpretation[81,82]. Moreover, devices that excel in cell yield/recovery often perform poorly in cell purity[83], establishing a need for methods that provide high rare-cell purity to avoid the bias of contaminating cells and enable meaningful clinical analysis. Furthermore, we envision that if widely accessible methods or technologies were available that could maintain cell viability and integrate with a range of existing lab-on-a-chip technologies, then a multitude of clinically relevant endpoints could be studied.

As mentioned previously, CTCs are an important example of a rare cell population of interest, as demonstrated by the wealth of CTC enrichment microdevices developed in recent years. Moreover, CTCs have been shown to contain clinically relevant information with regard to cancer progression and therapeutic resistance[84–86]. CTCs are found in peripheral blood at a frequency of ~1 in 10^8 to 10^{10} peripheral blood cells[87,88], and those isolated from patients with prostate cancer have been shown to exhibit high degrees of heterogeneity[89]. This heterogeneity extends to a range of molecular alterations including genomic, transcriptomic and proteomic differences in both solid tumor biopsies and CTCs from liquid biopsies[90,91]. For example, single cell RNASeq of prostate cancer CTCs identified intra- and inter- patient heterogeneity in expression of androgen receptor

(AR) splice variants, which is known to confer resistance to AR targeted therapies[92]. Accordingly, there is a critical need to understand the molecular alterations that account for, and may drive, cancer progression to develop improved biomarkers and therapeutic modalities for patients with advanced disease. To do so, there is a need for a system that works in tandem with bulk LOC enrichment devices for a system that works in tandem with bulk LOC enrichment devices that can retrieve purified, live CTC populations while maintaining requisite cell viability that enables robust downstream single cell interrogation.

For many years single-cell studies have been accomplished using cell micromanipulators (CMMs), which integrate directly with microscopes to interrogate cells of interest from a larger population[93–95]. These studies -- and many that followed -- used manually operated CMMs. Manual micromanipulators have been essential for advances in neuroscience[96], microbial science[97], and in-vitro fertilization[98]. Unfortunately, such manual models can be cumbersome, requiring a practiced hand to operate accurately. The inefficiency of these models results in low sample throughput. To mitigate the issues with slow throughput, companies have recently developed fully automated CMM technologies. Automated platforms that have already been used to isolate CTCs include the AVISO CellCelector and the RareCyte CyteFinder/CytePicker[99,100]. Being fully automated, these technologies present major advantages in sample processing and throughput, but these benefits come at a steep price; they can be as much as 100x more expensive than manual CMMs. In order to make advanced molecular analysis of CTCs more accessible to researchers, a less expensive, high-throughput single cell manipulation technique is needed to couple with upstream bulk enrichment technologies.

To address the need for an affordable, yet robust CMM platform, we have developed a semi-automated system for purifying rare cell populations. This system is designed to work in tandem with various upstream LOC bulk enrichment technologies and costs less than $3,000 to fabricate (Table S1 in Appendix 1). Furthermore, this system – referred to as the Semi-Automated Single Cell

Aspirator (SASCA) – integrates modularly with standard inverted microscopes which are already present in many laboratories, especially those investigating CTCs (Fig. 3.1A). This integration reduces cost by obviating the need to purchase expensive equipment. In addition to microscope integration, the SASCA couples with established LOC technologies to immobilize cells and increase throughput (Fig. 3.1B).

For years microwell arrays (MAs) have been used in microfluidics to isolate individual cells for various single cell assays. Previous applications have included single cell PCR, cytokine secretion, and natural killer cell interactions[101–103]. For the SASCA, sample cells are evenly distributed in a unique polydimethylsiloxane (PDMS) microwell array (MA) to immobilize and contain the cells, thereby enabling robust single cell selection and negating the worry of accidental contaminant aspiration as seen with some glass slide setups (Fig. 3.1C). The technique of paring a CMM with a MA was previously demonstrated in 2009 by Ozawa et.al. where a manual CMM was used to select rare targets from a heterogeneous population. Specifically, they isolated rare B-cell populations expressing type A influenza nucleoprotein from the blood of vaccinated patients for downstream antibody generation, illustrating the enrichment capabilities of the method[104].

We further improved our final purity by matching experimental results with a Pólya-Aeppli probability distribution to optimize our microwell seeding method and developed a custom software that incorporates real-time detection and localization of target cell subpopulations. To isolate a cell in a MA that has been identified using the software, the SASCA leverages the microscope's own mechanisms to navigate the MA in an automated fashion. These components contribute to improved objectivity of target cell selection, throughput, and sample purity. In this study we test the efficacy of the SASCA platform in rare cell purification through the collection of CTCs from the blood of patients with prostate cancer, showing that high-throughput phenotypic analysis of such samples can be accomplished at an affordable price.

3.2 MATERIALS AND METHODS

3.2.1 Semi-Automated Single Cell Aspirator

The single cell aspirator presented in this study is an assemblage of commercially available items and custom engineered parts. A four-axis mechanical CMM (Siskiyou, MX130R) was used to hold a glass micropipette (50 μm tip inner diameter, FIVEphoton Biochemicals, MGM 1C-50) and perform initial pipette alignments. The CMM was bolted to an aluminum mounting cantilever that was custom machined (dimensions listed in technical drawing in Appendix 1) out of aluminum square bar stock (⅝ inch, Grainger, 2EZP2). The cantilever base was machined out of aluminum flat bar stock (¼ x 3 inches, Grainger, 2EYZ6) and embedded with three neodymium magnets (K&J Magnetics, one R822CS-N52 and two R622CS-N52) which held the base in place when it was slid into the mounting plate (Fig. 3.2A-C). The mounting plate was made of a 1/64 inch thick steel sheet (10 x 4 inches, Grainger, 16NH24) that was bent into the shape of the cantilever base. The steel mounting plate was attached to the top of the microscope's motorized nosepiece housing (Fig. 3.2B) using double sided tape (ARCare, 90106). Fluid movements for aspirating and dispensing cells were controlled by a manual microinjector syringe pump (Sutter Instruments, 10 μL syringe model), which was connected to the CMM via a 3 ft length of plastic microtubing (United States Plastic Corp., #054397).

3.2.2 Microwell Arrays

Microwell arrays were fabricated out of PDMS (Dow SYLGARD™ 184) using soft lithography replica molding techniques[105,106]. A mold for the MA was fabricated using established SU-8 photolithography techniques[107] and placed in a plastic petri dish. Using a standard 1:10 ratio of cross-linking agent to pre-polymer, a PDMS solution was mixed and de-gassed before being poured

over the molds. The PDMS was cured at 70° C for 4 hours and allowed to cool for at least 1 hour before removal from the mold. Finally, before they were ready for use, the MAs were cleaned using a Soxhlet extractor filled with 70% EtOH.

3.2.3 SASCA Media

During the single cell aspiration process, two specialized solutions were used interchangeably to prevent cell adhesion and maintain cell viability. In initial experiments a specific SASCA media was developed using DMEM media with 4.5 mg/mL glucose, 0.1% BSA (Sigma-Aldrich, A9056), 0.1% Pluronic F-127 (Sigma-Aldrich, P2443), and 10 mM HEPES buffer (Gibco, 15630-080). Pluronic F-127 was specifically used because it has been shown to inhibit cell adhesion in biomedical research[108–110]. Eventually a commercially available PBS blocking buffer (SuperBlock™, Thermo Fisher) was found and substituted in place of the SASCA media when performing cell line nucleic acid extraction experiments.

3.2.4 Microwell Loading

Microwell arrays were placed on precleaned microscope slides (Fisherbrand, 12-550-15) before being loaded. Due to the hydrophobicity of PDMS, the microwells do not spontaneously fill with media. To promote microwell filling, the empty bullseye MAs were placed in a vacuum chamber for 30 minutes as previously described[66]. Immediately following PDMS gas evacuation, 60 µL of either SASCA media or SuperBlock™ buffer was pipetted onto each bullseye -- within the inner edge of the moat -- and allowed to fill for 15 minutes. After the microwells had filled, the samples were added.

The volume of the patient samples following initial enrichment could vary from 50-80 µL, which was near the maximum volume a bullseye could contain within the inner rim of its moat, so before adding the sample to its respective bullseye(s), 50 µL of the initial 60 µL of liquid used to fill the device was removed. Leaving behind 10 µL ensures that the wells remain filled and covered with a

thin film of media; if this film is allowed to evaporate the wells will not refill without requiring an additional vacuum chamber treatment. Next the sample is pipetted onto its respective bullseye MA, being careful not to spill into the moat and risk losing cells.

Once the sample is seeded, the MA device is placed in a covered omni-tray and left in a darkened chamber for the cells settle into the microwells. The cells were allowed to settle for approximately 15 minutes, but no less than 11 because the theoretical settling velocity of cells (2.8 cm/h) suggests that a cell at the top of a 5 mm tall liquid droplet requires almost 11 minutes to reach the bottom[111]. After the cells are fully settled, the moat is filled with 10 μL of media or buffer, merging with the sample droplet and pinning it within the outer bounds of the bullseye moat. The moat filling step is critical for proper brightfield imaging later on.

3.2.5 Cell Seeding Simulations

To quantify how different protocols for cell collection might influence final sample purity, we simulated the process of cell seeding and collection. After performing a virtual cell seeding to randomly distribute 250 target cells with different levels of background cells, microwells with target cells were collected in two ways. Using a "naive" approach, each microwell that is encountered containing target cells is collected. Using an optimized or "ranked" approach, microwells are visited in order of decreasing purity. In both cases, collection proceeds until 50 target cells are collected. The simulation was rerun 60 times for each level of initial sample purity using R statistical software. Collected/final sample purities (each containing 50 target cells and a variable number of background cells) were then calculated. Final purities using the "naive" and "targeted" approach were then compared.

3.2.6 Microscopy and Target Cell Identification

The SASCA system was mounted to a Nikon Eclipse Ti-E inverted fluorescence microscope (Nikon USA, Melville, NY), and images were acquired at 10x magnification in bright-field and three fluorescence channels: 390 nm (Hoechst), 560 nm (EpCAM), and 648 nm (Exclusion). To identify target cells, images were acquired across the entire bullseye MA and analyzed using custom software written in MATLAB (The Mathworks, Natick, MA) (github.com/dn008j). This process was fully automated and performed in real-time during image acquisition in order to minimize the time spent prior to the aspiration of cells.

The analysis algorithm involved distinct processes depending on the image channels. All cells were detected based on fluorescence intensity using the Hoechst channel. The mask of detected nuclei was combined with that of microwells detected in the bright-field channel in order to restrict interest to cells lying within microwells. Fluorescence images for EpCAM and Exclusion were background-subtracted, then the mean fluorescence within detected cells was calculated. After processing all MA images, a plot of EpCAM vs. Exclusion for all cells was produced and thresholds were manually placed on this plot to define the target and exclusion cell staining profiles. Cells which were $EpCAM^{+}/Exclusion^{-}$ were considered to be CTCs, while PBMCs were defined as $EpCAM^{-}/Exclusion^{+}$. For the subsequent image-guided aspiration, a list of CTC locations was generated and imported into NIS Elements as a multipoint list. By clicking through each point on this list the microscope stage automatically locates to the specific cell coordinates, allowing the user to quickly navigate a sample.

In some experiments where cell recovery was being characterized, the bullseye MA was again imaged following aspiration to confirm removal of all target cells, and the collected cells were separately imaged to evaluate target cell purity. However, this follow-up imaging step was not performed during experiments where nucleic acid endpoints were the focus, as maintaining cell

viability was prioritized. In transcriptomic experiments the cells were aspirated and immediately dispensed into lysis buffer to protect molecular integrity.

3.2.7 Cell Aspiration from Microwell

The following steps were used to ensure successful cell aspiration from microwells. With the tip positioned above the target microwell (Fig. 3.1D-i), the glass pipette was lowered into the well by lowering the z-plane of the microscope (Fig. 3.1D-ii). This process brings the cells slightly out of focus, yet the blurred image of the target cell can still be tracked visually when using 10X magnification. Slight deformation of the microwell's elastic wall was used as an indicator for when the pipette tip had been properly lowered into the well (Fig. 3.1D-ii). Next, the syringe pump is used to generate a suction force within the pipette tip, aspirating the contents of the well. Finally, the pipette tip is raised out of the microwell as the level of the z-plane is returned to its initial position, bringing the cells back into full focus (Fig. 3.1D-iii).

3.2.8 Dispensing Cells

Aspirated cells can be dispensed into a droplet of buffer in various fluid containers. Specifically, in this study cells were dispensed into situation-specific buffers held within either a silicone isolator well array (Grace Bio-Labs, JTR10S-A-2.0) or a clear, flat-bottom PCR strip cap. The buffers used in this study included the SASCA media, SuperBlock™ buffer, and lysis buffer (RLT Plus + βME). The volumes of the buffers used also depended on the specific endpoint (i.e. - cell imaging and quantification, RNA or DNA extraction). The silicone isolators were placed adjacent to MAs on the glass slide, and PCR strip caps were placed proximal to the slide on the sample processing device. This limits the time spent between aspirating and dispensing cells, promoting maintenance of cell viability. Silicone isolators were used for imaging and quantifying aspirated cells to characterize target cell recovery and final purity, with each well containing 35 μL of SASCA Media.

For the purposes of mRNA extraction, isolators were filled with lysis buffer. Alternatively, for whole genome amplification, cells were dispensed into inverted PCR caps containing (1-4 μL) of PBS. Cell transfer to the caps was visually confirmed by keeping the micropipette tip in focus while imaging in real time as cells were dispensed using the microsyringe pump. Tubes were then placed on the caps, reoriented to the upright position, and briefly centrifuged before continuing with the WGA protocol.

3.2.9 Cell culture

The prostate cancer cell line 22Rv1 (ATCC CRL-2505) was a gift from Scott Dehm at the University of Minnesota. Monocytic cell line THP-1 (ATCC TIB-202) was a gift from Fotios Asimakopoulos at the University of Wisconsin. Prostate cancer line LAPC4 was a gift from Doug McNeel at the University of Wisconsin. Prostate cancer cell line C4-2B was a gift from Felix Feng at the University of California- San Francisco. LAPC4s were cultured in DMEM media (Corning Cellgro) supplemented with 20% fetal bovine serum (Gibco). Remaining cell lines were cultured in RPMI 1640 Medium (Corning Cellgro) supplemented with 10% fetal bovine serum. All media included 2% Penicillin-Streptomycin (HyClone). THP-1 medium was also supplemented with 1% Gibco GlutaMAX (LifeTech).

3.2.10 Cell Preparation

Cells were isolated by trypsin digestion and washed with 1x PBS + 0.1% BSA. 22Rv1s were stained with anti-EpCAM [Phycoerythrin, VU-1D9] (Abcam) and THP-1s were stained with anti-human CD45 (AlexaFluor 647, BioLegend). Both cell lines were also incubated with Hoechst 33342 (Life Technologies) to visualize nuclei.

3.2.11 Blood Processing & Cell Isolation

Whole blood was collected from patients with metastatic prostate cancer. The study was approved by the University of Wisconsin Institutional Review Board and patients supplied written informed consent. PBMCs were isolated using a Ficoll-Pacque Plus (GE Healthcare) gradient before undergoing CD45 depletion (MACS, Miltenyi Biotec). The VERSA[112–114] platform was used to capture CTCs with an anti-EpCAM antibody and stain for extracellular markers EpCAM [VU-1D9] (Phycoerythrin, Abcam), CD45, CD34, and CD11b (AlexaFluor 647, BioLegend).

3.2.12 Reverse Transcription, Pre-amplification, and Quantitative RT-PCR

Preliminary mRNA extraction (Fig. 3.4B) to demonstrate the enrichment ability of the aspirator was completed as described by Strotman et al.[61]. Purification of total RNA at low cell numbers (Fig. 3.5A) was performed using the RNEasy Plus Micro Kit (Qiagen). cDNA was generated using the High Capacity cDNA Reverse Transcriptase Kit (LifeTech) and Bio-Rad C1000 Thermo Cycler (Bio-Rad), as per manufacturer guidelines. The generated cDNA was then amplified for 14 cycles using a Taqman PreAmp Master Mix (LifeTech), before being diluted 1:20 in 1x TE (10 mM Tris-HCL pH8, 1mM EDTA). For TaqMan assays, 5 µL of diluted cDNA template was mixed with 10 µL iTaq master mix (Bio-Rad, USA), 1 µL TaqMan Gene Expression Assay (Life Technologies, USA) and 4 µL nuclease free (NF) water. Each reaction was amplified for 45 cycles (denature at 95°C for 15 seconds followed by annealing at 60°C for 1 minute) using a CFX Connect Real-Time PCR System (Bio-Rad, USA). Primers used were: AR_V7 (Hs4260217_m1), TMPRSS2 (Hs01120965_m1), KLK3 (Hs02576345_m1), PTPRC (Hs04189704_m1), RPLOP0 (Hs4333761F), and POLR2A (Hs00172187_m1).

3.2.13 Whole Genome Amplification

Cells isolated using the SASCA were dispensed directly into a droplet of PBS placed at the bottom of a PCR reaction tube before undergoing lysis and whole genome amplification (WGA) using a modified version of the Repli-G Single Cell kit (Qiagen). Recommended modifications to the kit as listed in Sho et al. included a 30 minute lysis period (as opposed to 10 minutes recommended in the kit's protocol), and division of the amplification step into 16 individual reactions. We adjusted this methodology to include the extended lysis period, but reduced the number of parallel reactions to 8. Amplified genomic DNA underwent a pre-amplification step before undergoing qPCR as described above. Primers used were: ACTG1 (Hs03044422_g1), BRAF (Hs01052465_g1), GAPDH (Hs02758991_g1), KIT (Hs00922194_g1), KRAS (Hs00364284_g1), PIK3CA (Hs00611502_s1), and UQCRC1 (Hs00899647_g1) (Life Technologies).

3.3 RESULTS

3.3.1 SASCA Platform

Microscope Integration

The SASCA consists of three main parts: 1) the mechanical micromanipulator (Fig. 3.1A-i), 2) the magnetic mounting cantilever (Fig. 3.1A-ii), and 3) the manual syringe pump (Fig. 3.1A-iii). The syringe pump and micromanipulator are connected by a length of plastic microtubing (Fig. 3.1A-iv), to allow precise fluid movements. This manual syringe pump was chosen over more advanced models because it was less expensive, but with a 4.2 nL resolution it still provides adequate control when aspirating cells. The mounting cantilever (Fig. 3.1A-vi) attaches the micromanipulator to the z-axis of the microscope via a magnetic base (Fig. 3.2A) rather than the microscope stage (Fig. 3.1A-

v). By mounting to the z-axis, the micropipette tip (Fig. 3.1A-vi) can be easily moved in and out of wells using the focus knob on the microscope. A shaped steel plate provides a ferromagnetic mounting pad for the cantilever and is a permanent fixture on the microscope, though it does not affect operation of the microscope (Fig. 3.2B). Moreover, it allows for quick and precise attachment of the aspirator to the microscope by guiding the cantilever base into position where it is held in place by the magnets (Fig. 3.2A-C).

The unique mounting method implemented by the SASCA platform provides two significant advantages over traditional mounting techniques. First, this approach holds the aspirator stationary in x-y directions relative to the microscope stage (Fig. 3.1B). To navigate the microwell platform, the stage is moved using the microscope's built-in x-y joystick. This allows the pipette tip to *remain fixed in the field of view* while the user scans the sample (Fig. 3.1C). This concept of camera following the end-effector is similar to what is used on specific manufacturing robots that implement object-related machine vision [cite robot guidance 2016]. The technique uses a camera (microscope objective) that is fixed in such a way that it continuously follows the motion of the end-effector (micropipette tip). Second, when a cell is being aspirated the mounted CMM is moved up and down the z-plane using the objective focus knob (Fig. 3.1D). This is a major advantage of the platform as it provides quick yet precise movements in and out of microwells. By exploiting the microscope's own maneuvering mechanisms, the SASCA platform is able to achieve the precision and accuracy of automated platforms while remaining affordable.

Microwell Integration

Microwell arrays can be used to significantly aid single CTC isolation[99,115,116]. Viscous forces at the micro-scale help to slow fluid flow within the microwells, thereby preventing cells from being dislodged or removed by exterior flows. In the context of single-cell aspiration, this allows the

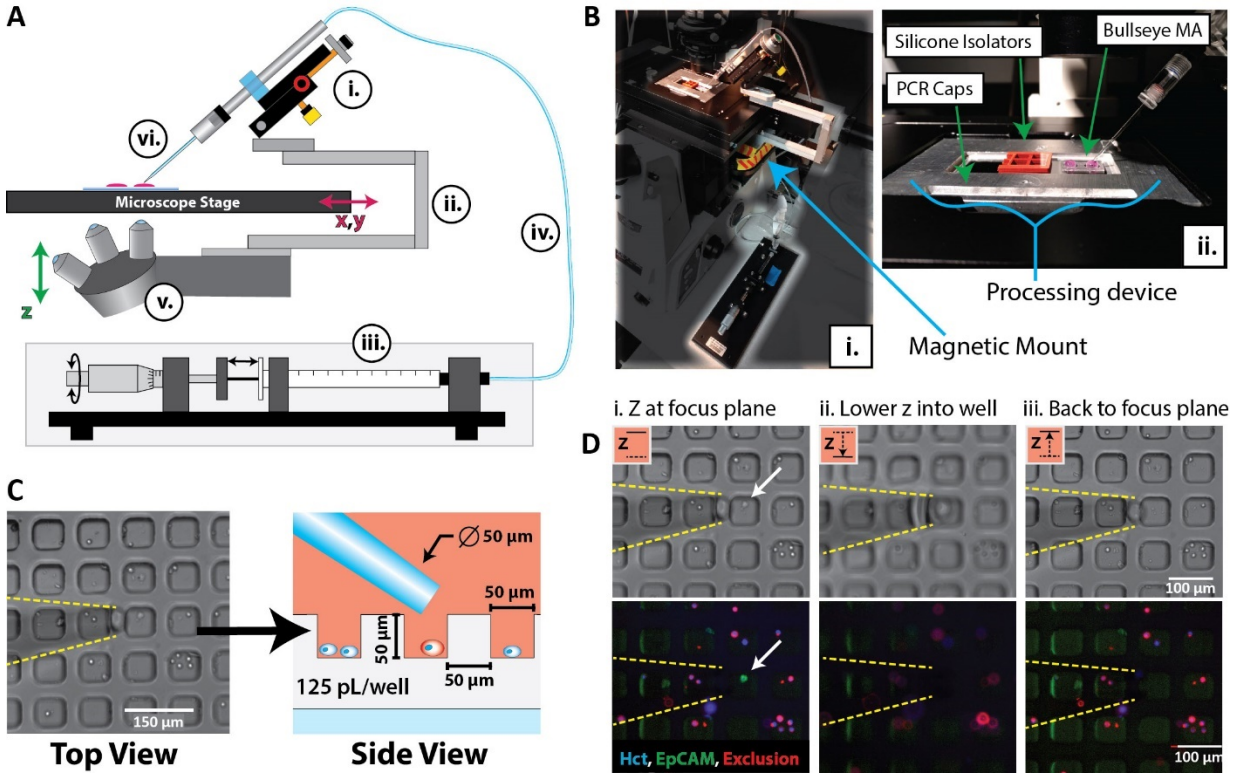

Figure 3.1. *SASCA Platform* – The semi-automated single cell aspirator platform is engineered to integrate with inverted microscopes. A) The aspiration apparatus itself is made up of several components, including the multi-axis micromanipulator (i), the mounting cantilever (ii) (v), and the 10 µL syringe pump (iii). The syringe is connected via microtubing (iv) to the glass pipette (50 µm inner diameter) (vi). B) The platform attaches easily to the microscope (i) and integrates well with the processing device (MAs, silicone isolators, and PCR caps) (ii). C) To entrap the cells, the samples are seeded into MAs. D) Samples can be imaged and processed efficiently, using the microscopes own x,y,z mechanical movements to navigate to cells expressing target markers (EpCAM, green) (i). When identified, target cells can be aspirated by lowering the z-plane of the microscope itself, which drops the pipette tip into the target well for aspiration (ii). Afterwards the z-plane is raised back to the focus plane, bringing the pipette tip out of the well (iii).

contents of one microwell to be aspirated without aspirating contaminants from adjacent wells (Fig. 3.1D). We have enhanced the interface between users, aspirators, and microwells by integrating a pipette-friendly MA design that we recently developed[66,117]. The original bullseye MA design was modified slightly for this rare cell application by removing the recessed region in the center to maximize the number of microwells, reduce dead-volume, and minimize cell loss. The resulting microwells had dimensions that were ~50x50x50 µm (well volume of 125 pL), with the well-to-well spacing in the array also being 50 µm in either x or y direction (Fig. 3.1C).

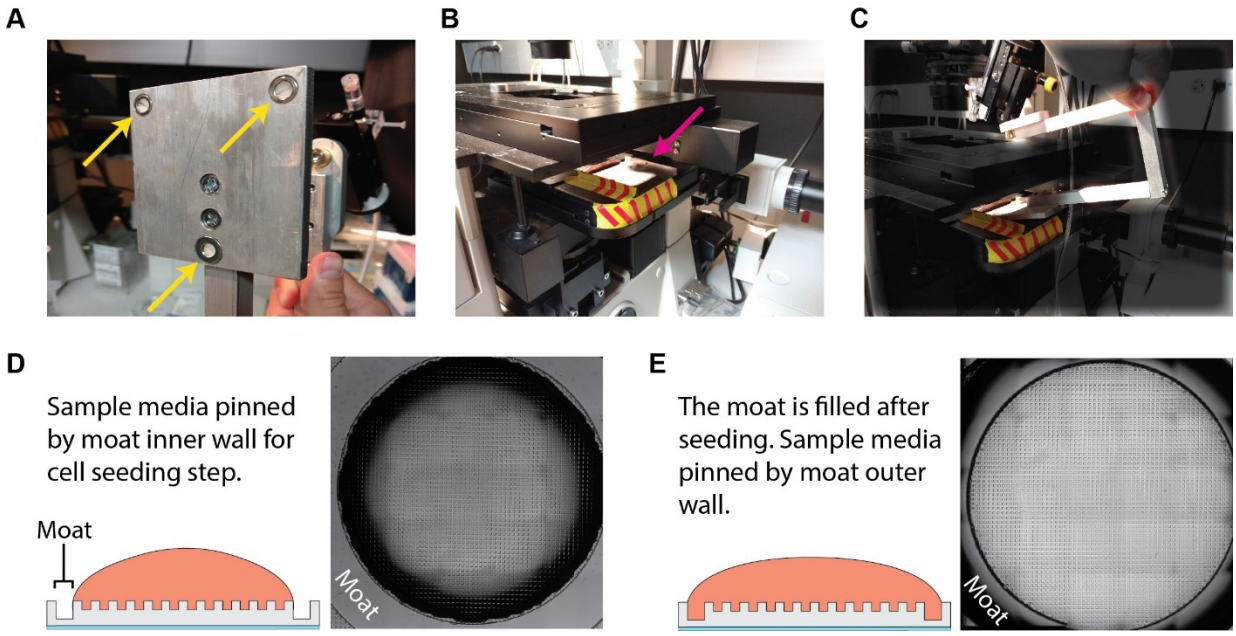

Figure 3.2. *SASCA Mounting and Processing Device* – A) Neodymium magnets (yellow arrows) were embedded into the base of the mounting cantilever to hold the aspiration apparatus in place. B) The magnetic base fits snugly into the steel mounting plate (pink arrow), which was fitted to the nosepiece motor housing of the microscope (indicated by the yellow and red striped hazard tape). C) The base of the mounting cantilever is precisely guided into the correct position by the shaped steel mounting plate. D) To avoid losing rare cells, the sample is pinned within the inner perimeter of the bullseye MA moat during the cell seeding step. E) Once the cells have settled into the wells, fluid is added to the sample, allowing the moat to fill, which greatly improves BF scanning near the periphery of the bullseye.

To contain samples into finite arrays, a circular "moat" (250 μm deep) was fabricated around an array of ~2800 microwells, giving the MA a diameter of 6 mm. The moat provides a surface tension driven barrier at the exterior edge of the sample. Unfortunately, refraction and interference near the periphery of the sample droplet resulted in dark regions in the bright-field channel, obfuscating the microwells (Fig. 3.2D). This was problematic for our software-based identification, because it only considered cells within software-detected microwells. To address this, a moat filling step was added after the cells had settled. To eliminate any bright-field shadow near the edge of the microwell array, the moat is filled with 10 μL of extra media so it merges with the sample (Fig. 3.2E). It was important to only fill the moat after the cells had settled into the microwells to prevent the loss of cells. Moving the droplet edge shadow beyond the perimeter of the MA greatly improved

the success of identification and aspiration of cells near the periphery of the bullseye, which ensured that no rare cells were excluded from software detection.

Optimizing Microwell Seeding and Collection

When the microwell array is seeded with a heterogeneous suspension of cells, it is possible for multiple cells to settle into a single microwell, which can result in a mixed population of cells occupying the same well. Because sample purity is of the utmost importance, the goal of microwell seeding is to maximize the ability to isolate and collect the rare target cells while minimizing collection of contaminating background cells. To optimize this process, one must be able to predict/estimate how many cells will occupy each microwell. Traditionally, a Poisson distribution has been used to model microwell seeding[118,119]; however, this model does not take into account the fact that cell suspensions are generally not monodisperse (i.e., some cells cluster with one another). To account for the presence clusters, we used the closely related Pólya-Aeppli distribution instead.

The Pólya-Aeppli distribution is typically used to model the "Poisson delivery" of clusters of items where the number of items per cluster follows a geometric distribution. Two parameters define the Pólya-Aeppli distribution. The first parameter is identical to the standard Poisson parameter, λ (i.e., average number of clusters delivered to a microwell). The second parameter, p, defines the geometric distribution of cluster sizes (i.e., the average number of cells in a cluster). In this case, $p = 1/(1 + \text{average number of cells per cluster})$. Fig. 3.3A illustrates how the probability distribution of cells per well shifts when settling objects are considered to be cell clusters (1 to 6 cells/cluster) rather than a monodisperse suspension.

To confirm that a Pólya-Aeppli distribution improves upon established microwell seeding models, experimental cell-count distributions were measured from MAs seeded at different densities. These experimental distributions were fitted with either a Poisson distribution (Fig.

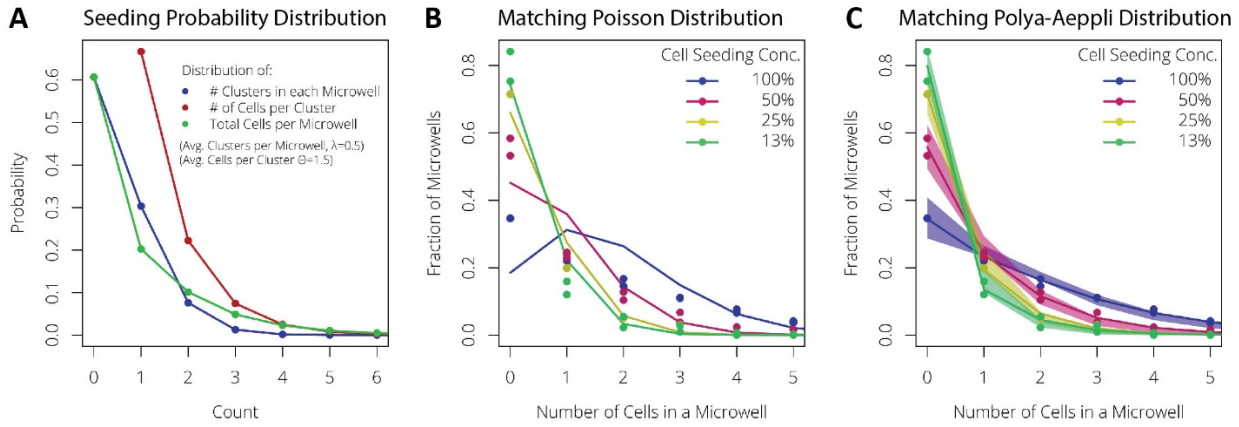

Figure 3.3. *Optimizing Cell Seeding* – A) The probability distribution of cells per microwell shifts if objects settling into wells are considered to be clusters of cells rather than individual cells. The occurrence of single-cell clusters remains the most probable, but accounting for multi-cell clusters increases the probability of wells containing 2-5 cells. B) Traditional cell seeding distribution is modeled using a Poisson distribution compared to experimental cell seeding conditions with range of four different cell:well ratios. C) However, a Pólya-Aeppli distribution accounts for multi-cell clusters and proves to be a much better predictor of cell distribution in MAs using the same data as (B). The shaded ribbons shadowing each model line represents the 95% confidence interval.

3.3B), or a Pólya-Aeppli distribution (Fig. 3.3C) using maximum likelihood estimation (R, 'stats4' and 'polyaAeppli' packages, www.r-project.org). The Pólya-Aeppli distribution followed the data much more closely and was able to model changes in suspension density via changes in λ while maintaining a consistent estimate of the average cluster size. To our knowledge, this represents the first proposal and demonstration of using the Pólya-Aeppli distribution to better model cell seeding distributions in microwell arrays.

Given that some microwells will contain 100% target cells (i.e., 100% purity) while others will contain differing numbers of contaminating cells (i.e., < 100% purity), we proposed to optimize collection of seeded target cells by visiting microwells in order of decreasing purity. This "ranked" approach can be compared to a "naive" approach which is defined as indiscriminately collecting cells from any microwell containing at least one target cell (i.e., in random order of purity). The value of a ranked approach can be seen in the simulations summarized in Fig. 3.4. If a naive approach is used, the simulated results suggest a sample purity ≥50% can be achieved if the cell to

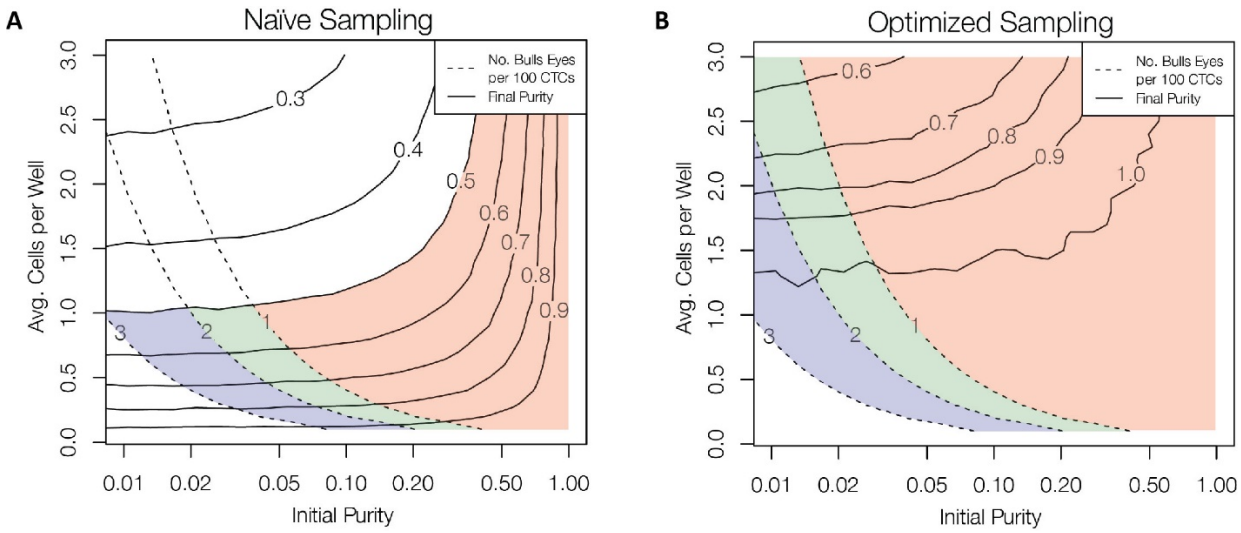

Figure 3.4. *Simulating Cell Collection* – The sample is gathered by either visiting wells naively (i.e., all wells were sampled or some wells were sampled at random) or by visiting wells in order of decreasing purity (i.e., a rank optimized sampling approach). It is assumed that when sampling a microwell, all cells within the microwell are gathered. Simulations are run assuming that 250 target cells existing in the entire sample that has an initial purity described by the x-axis of the plots. Initial purity is calculated as target / (total cells) while the final purity of the sample is targets collected / (total collected). Red regions represent samples that only required a single MA array (i.e., 2500 microwells). The green regions are samples that can be gathered using an additional MA array (2 total) while blue uses 3 total MA arrays. A) Final purity of the sample when using naive sampling. B) Final purity of the sample when using optimized sampling.

well ratio is kept at or below 1:1 (Fig. 3.4A). If a ranked approach is used, final purity increased to 100% (Fig. 3.4B). Given this result, we developed a semi-automated collection method that enables ranking of microwells by purity to increase final purity.

3.3.2 Semi-Automated Processing

After cells are seeded into microwells, target cells can be identified in two separate ways. With the Manual Image and Capture (MIC) technique used above, where the user scans through the microwell by eye, cycling through the fluorescent channels along the way to identify target cells. Once a target cell has been discovered, it is subsequently aspirated. This approach becomes tedious, even with the high maneuverability of the SASCA. In comparison, the Automated Image and Manual Capture (AIMC) method incorporates real-time image processing software into the workflow. The

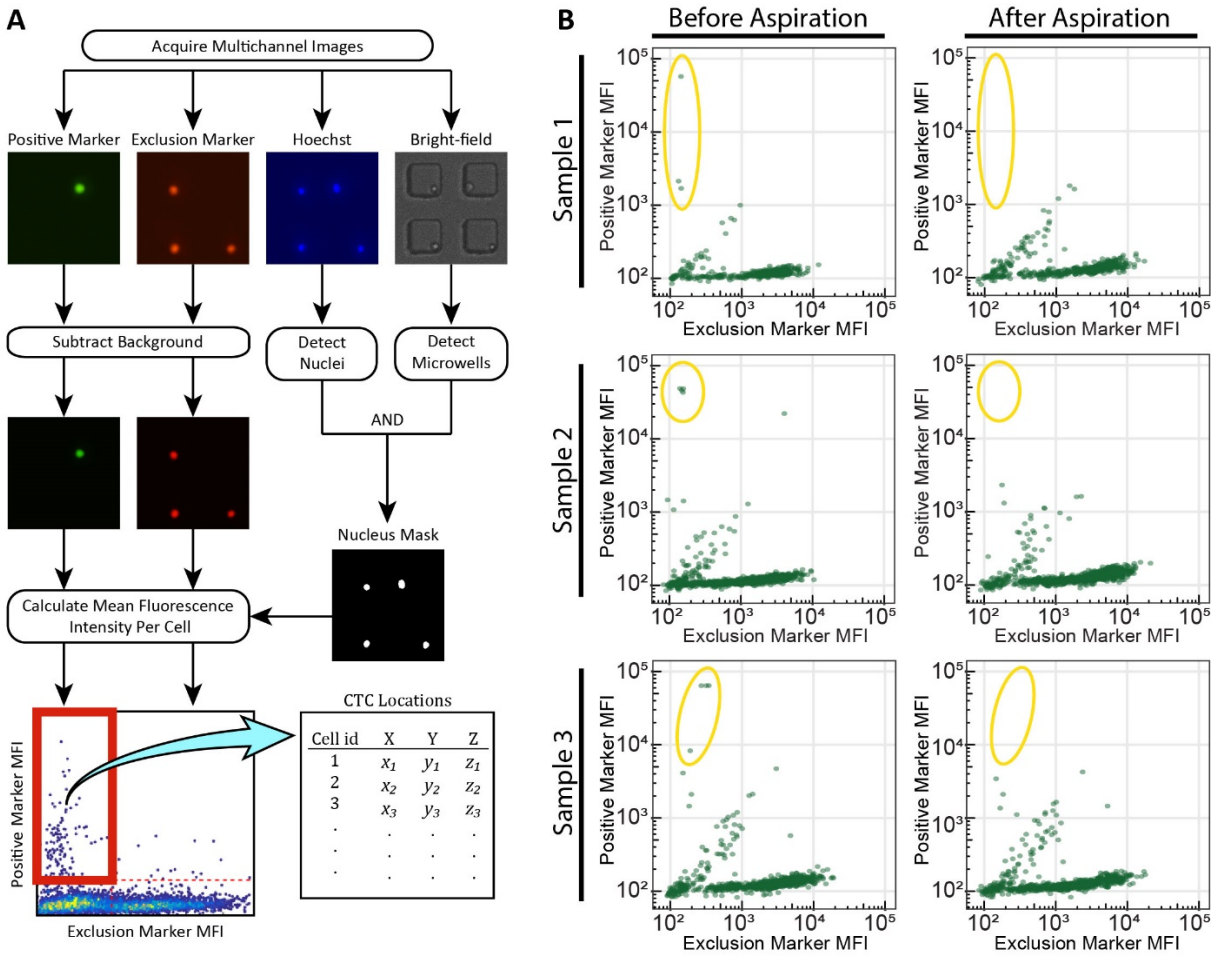

Figure 3.5. *Semi-automated Detection of CTCs* – A) Cell detection algorithm using multichannel images. Cells which were EpCAM + /Exclusion - were considered CTCs (red box). The locations of these cells were used to guide subsequent aspiration. B) Scatter plots of fluorescence intensity of cells in three distinct bullseye samples. The bullseyes MAs were imaged before and after aspiration, demonstrating the successful identification and collection of a rare target cell sub-population (yellow ellipse) within heterogeneous samples. The initial sample purities were approximately 1% for each of the three samples.

software pre-scans a sample for cells exhibiting phenotypes of interest. In less than 5 minutes, the program identifies potential targets, records and processes data on these targets, and outputs a list of discovered cells (and their locations) to assist the user in their decision-making process (Fig. 3.5A). All of these functions are performed simultaneously while the sample is scanned by a microscope macro. With AIMC, the user is directed toward potential targets, enhancing both the output purity achieved and speed at which targets are isolated.

The coordinate list generated is loaded into NIS Elements software and used to quickly navigate from one point of interest to another. Once the cell of interest is identified, the user validates whether or not the cell should be targeted for aspiration. To confirm that this semi-automated identification and navigation can reliably collect rare populations of cells within a sample, heterogeneous mixtures of background and target cells were prepared at an initial concentration of approximately 1% target cells. This heterogeneous sample was seeded into three separate bullseye MAs and processed using the AIMC technique. By collecting only cells that were identified as targets by the algorithm, it was shown that every target cell in each of the three samples was identified and collected (Fig. 3.5B).

The semi-automated method of identification and navigation increases processing speed without compromising cell recovery and final purity, allowing users to quickly scan through the samples in a directed fashion. The workflow for the SASCA is divided into three parts: upstream LOC bulk enrichment, SASCA cell purification, and downstream rare cell interrogation (Fig. 3.6). LOC bulk enrichment is vital because it aims to decrease the number of cells to a manageable quantity for seeding into MAs. Platforms available for upstream CTC isolation rely on a combination of immunoaffinity mechanisms (positive/negative selection), size filtration, electrophoresis, and inertial focusing[120]. However, as described above these platforms do not provide single cell resolution, necessitating further enrichment using the SASCA. Once pure populations of viable cells have been isolated, they can be interrogated for molecular heterogeneity with deep genome sequencing, used for organoid culture, or transciptomically analyzed. These downstream analytic methods can offer a more comprehensive insight into genomic heterogeneity and CTC diversity found in patients.

To illustrate the improvement of aspiration with AIMC, heterogeneous cell mixtures were made with an initial target cell purity of approximately 1% and 10%. These ratios were chosen because they should be representative of sample purity after an initial bulk enrichment step is completed.

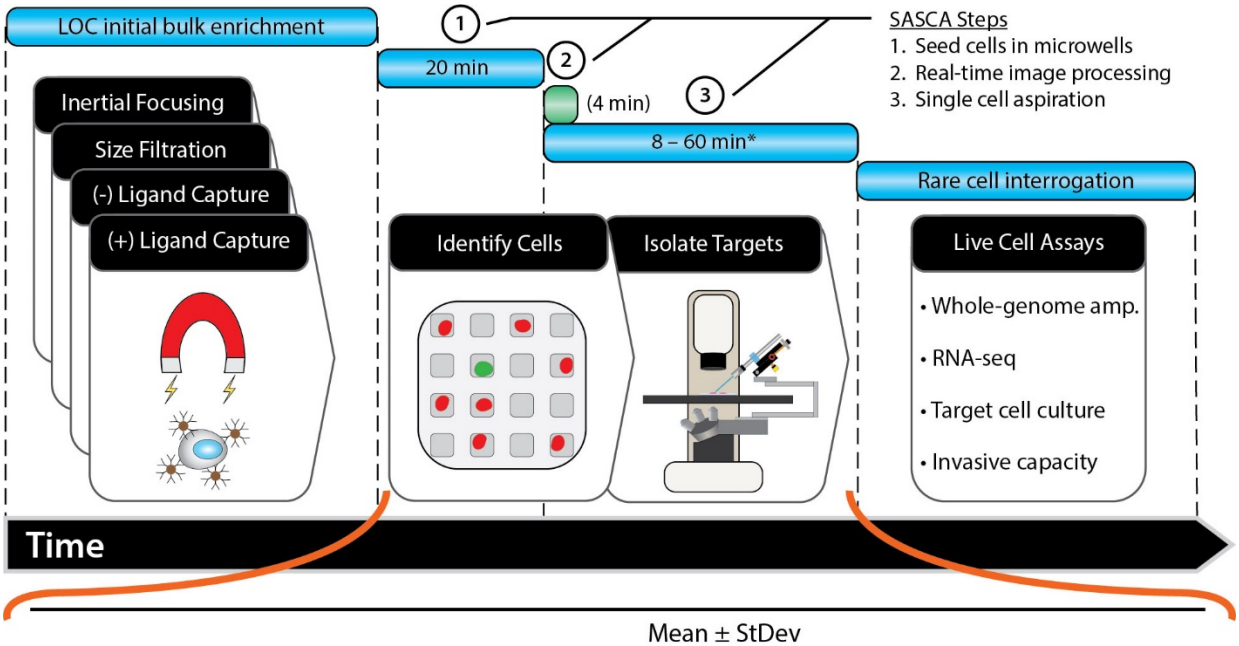

	Mean ± StDev			
SASCA Method	Approx. Input Purity (%)	Output Purity (%)	Targets/10 min	Transfer Efficiency (%)
MIC	10.0	98.4 ± 2.7	9.91 ± 1.1	95.0 ± 8.7
AIMC	10.0	100 ± 0	11.3 ± 1.6	93.3 ± 12
MIC	1.0	88.9 ± 19	2.48 ± 1.0	93.3 ± 12
AIMC	1.0	93.3 ± 12	5.32 ± 1.5 *	85.0 ± 13

Figure 3.6. *Sample Throughput* – (Top) The general SASCA workflow begins with the initial bulk enrichment of CTCs from whole blood using any variety of LOC enrichment techniques. Once the bulk sample is enriched it is processed using the SASCA platform. The sample is seeded into a MA, the sample is imaged and cells are identified in real-time (optional), and targets are gently aspirated for downstream assays. In total, the SASCA platform step adds <90 minutes to the total processing time. (Bottom) When comparing MIC and AIMC protocols, it was found that the AIMC protocol increased aspiration rate (*p = 0.03) while not sacrificing final purity or CTC transfer efficiency (n=3).

Target cells were identified using either the MIC or AIMC method, before being aspirated, dispensed, and counted to quantify output purity and transfer efficiency. As shown in Fig. 3.6, both methods provided highly pure samples (90-100%) while very few cells were lost between aspirating and dispensing (85-95% transfer efficiency). We observed increased output purity and speed of target isolation when using the AIMC method relative to the MIC. In fact, the more impure the sample was, the more significant the increase in aspiration speed became (p = 0.03, Fig. 3.6),

suggesting that semi-automated processing could provide the viable, highly pure CTC samples required for advanced cell interrogation.

3.3.3 Aspiration Enriches qPCR Endpoint

To test the isolation capabilities of the SASCA, we focused on the enrichment of prostate cancer CTCs because it offers a heterogeneous system with a rare subpopulation of cells that have been shown to provide insight into disease progression and drug resistance. To evaluate the accuracy of the SASCA, we tested our ability to separate individual prostate cancer cell lines from a mixed cell sample based on phenotypic differences. To replicate a VERSA enriched CTC sample, a human prostate cancer cell line (22Rv1) was spiked into samples of human monocyte cell line, THP-1. We began by labeling the 22Rv1 cell line using anti-EpCAM-PE antibodies and the THP-1 cell line with anti-CD45-AlexaFluor 647 and mixing the cells at a ratio of 1:100. Pure samples of both 22Rv1 and THP-1 cells were also used as starting populations for aspiration to provide a pure cell benchmark. Each cell mixture was added to one or multiple bullseye MAs to ensure at least 50 cells were available for aspirations at a distribution of 720 cells per MA. The 22Rv1s were aspirated using the SASCA using the MIC method, prior to the implementation of the real-time imaging software. To quantify the accuracy of this process, the SASCA purified populations were imaged and manually identified as either a 22Rv1 target cell or THP-1 contaminant cell, as per their staining phenotype. Using this method, the SASCA platform achieved an output purity of 83.8% (Fig. 3.7A).

RNA was isolated from the aspirated cells to evaluate enrichment of prostate specific transcripts. Fig. 3.7B represents the qPCR results from this experiment. As expected, pure 22Rv1s expressed prostate specific markers, and THP-1s expressed high levels of leukocyte marker PTPRC (CD45) in both the pre-purified and aspirated samples. As compared to the pure THP-1 population, we observed reduced expression of PTPRC in the aspirated prostate cancer sample. Additionally, all prostate specific markers showed increased expression in the aspirated sample, indicative of a

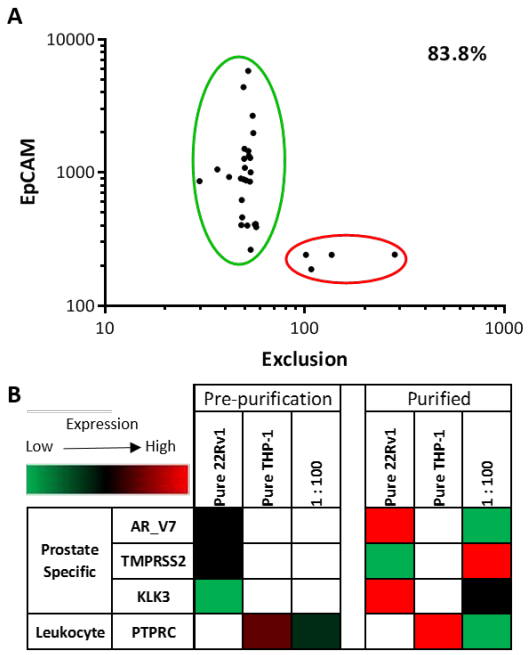

Figure 3.7. *Cell Line Enrichment* – A) Fluorescently labeled 22Rv1s and THP-1s were combined at a ratio of 1:100. The cell mixture was added to microwell arrays and 22Rv1 cells, identified using the MIC method, then isolated using the SASCA platform. Cells were imaged to quantify percent purity achieved (upper corner of scatter plot). Pure cell populations were also isolated. B) mRNA was extracted from approximately 50 cells from the initial cell populations indicated, as well as cells aspirated and described in (A). qRT-PCR was performed using primers specific for each gene listed. Data describes relative expression of each gene normalized to expression of POLR2A and P0 housekeeping genes. Expression was represented by a color scale from lowest (green) to middle (black) to highest (red). White indicates that no expression was detected.

highly enriched 22Rv1 population. Here, it is helpful to consider the composition of the initial cell mixture populations. Assuming an estimated 50 cells in each mixture prior to purification, only 0.5 cells would be found in a 1:100 mixture. This is reflected by the lack of expression of prostate specific markers. However, after purification with the aspirator, expression of these markers is significantly improved. This corresponds to a greater concentration of 22Rv1s in the final population of cells, indicating that the aspirator successfully enriched the target 22Rv1 population. Though we demonstrate our ability to precisely identify and isolate rare cell subpopulations, we further optimized the aspiration by automating the image processing software and applying the AIMC technique to isolate target cells from heterogeneous cell mixtures, with the aim of increasing purity and decreasing sample acquisition time.

3.3.4 Molecular Analysis of Low Cell Numbers

To determine the number of cells necessary for transcriptomic and genomic endpoints, we captured defined numbers of cells with the SASCA platform. First, the prostate cancer cell line C4-

2B was used to assess mRNA extraction and whole transcriptome amplification at low cell numbers. Starting with four different cell inputs (15, 10, 5, 3, and 1), we were able to successfully amplify all targeted prostate specific genes as well as housekeeping genes POLR2A and RPLOP0 for all starting inputs (Fig. 3.8A). All Ct values reported were under 35. A clear trend is visible between increased cell number and decreased Ct value.

LAPC4 cells were isolated with the SASCA platform followed by whole genome amplification (WGA) to evaluate quality of the amplified DNA using a panel of 7 genes. Amplification of genomic DNA from low numbers of aspirated LAPC4 cells (15, 12, 5, 3, and 1) was completed, then assessed using a qPCR assay. To validate our ability to obtain high quality WGA products, we used a cancer gene panel comprised of genes known to play a role in cancer[121]. Using a threshold for detection set at 36 Ct values, we chose a binary rating system to assess whether or not we had attained high quality WGA DNA (Fig. 3.8B). A starting input of ≥ 5 cells appears to provide a lower threshold for cell input, after which we are able to retain consistent quantities of DNA that should be reliable enough to perform downstream applications. Inputs of ≥ 5 cells gave expression readouts on all target genes, nearly half of genes for 3 cells, and only 2 genes for 1 cell. Due to a limited DNA template from which to amplify, stochastic amplification can occur, thus providing inexact WGA products. As seen in Fig. 3.7B, an increase in cellular input lessens this variability and is likely necessary for performing optimal downstream sequencing analysis. These findings are concordant with those from Sho et al., which showed that a cellular input of 5-10 cells is needed to reliably obtain amplified WGA products suitable for precise next-generation sequencing and aCGH analysis. Although we were able to obtain a low degree of single cell resolution for downstream genomics, we believe that a higher starting cellular input (5-10 cells) is imperative for generating amplified DNA with high fidelity. With regards to CTCs, it is not unreasonable to surmise that at least 5 CTCs would be found in a peripheral blood draw sample and accordingly be seeded into a microwell array for discovery and aspiration. Consequently, so long as the minimum threshold of cellular

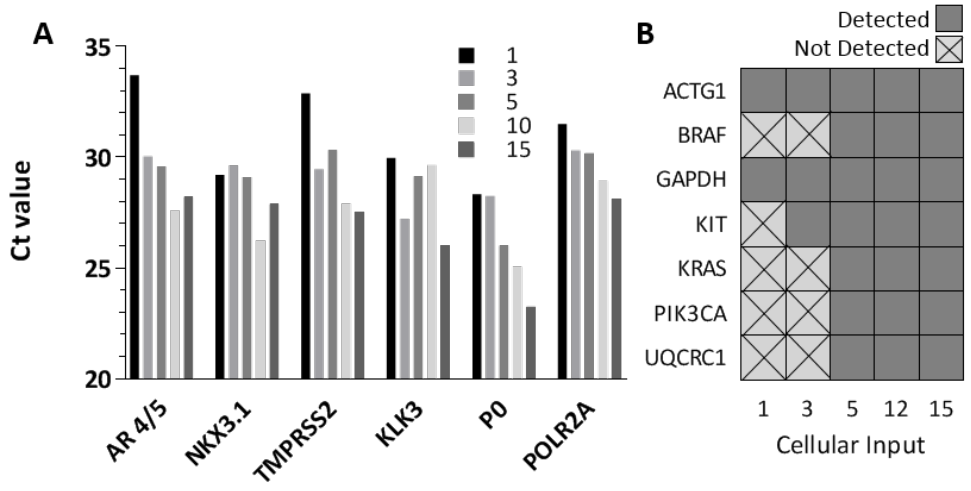

Figure 3.8. *Low Cell Numbers* – Pure cell line populations were seeded onto microwell arrays and the SASCA platform was used to isolate low numbers of cells. (A) C4-2Bs were dispensed into lysis buffer before undergoing mRNA extraction, reverse transcription, and qRT-PCR for primers specific to each listed gene. (B) LAPC4s were dispensed into PCR tubes before undergoing whole genome amplification and qRT-PCR. The binary heat map represents whether or not we were able to detect gene expression readouts for the target gene listed, using cellular inputs listed. Dark gray squares indicate detected expression, and light gray crossed-out squares indicate no detected expression.

input is reached, the integration of the SASCA platform with a modified WGA protocol should yield high quality WGA products from CTCs satisfactory for downstream sequencing analysis. Successful sequencing results enable a method to characterize the genomic landscape of a patient's disease, thereby increasing the clinical utility of a liquid biopsy.

3.3.5 Aspiration Selection of CTCs in CRPC

We applied the SASCA technology to isolated CTCs from patients with castrate resistant prostate cancer (CRPC). Blood samples were obtained from two patients. We isolated CTCs using the VERSA, an EpCAM antibody-based positive-selection system. Cells were stained in the VERSA with EpCAM and exclusion markers (CD45/CD34/CD11b). Captured cells were imaged in the VERSA device before being transferred to the microwell arrays. Of the events isolated as CTCs using the aspirator, 78% (5/23) were $EpCAM^{+}/Exclusion^{-}$ in patient 1, while 100% (8/8) were $EpCAM^{+}/Exclusion^{-}$ in

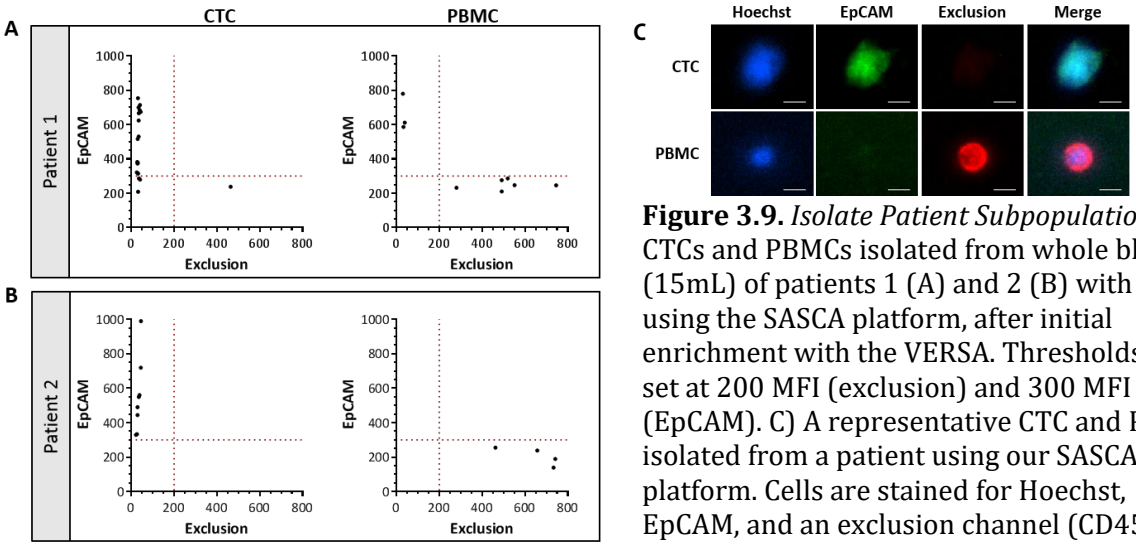

Figure 3.9. *Isolate Patient Subpopulations* – CTCs and PBMCs isolated from whole blood (15mL) of patients 1 (A) and 2 (B) with CRPC using the SASCA platform, after initial enrichment with the VERSA. Thresholds are set at 200 MFI (exclusion) and 300 MFI (EpCAM). C) A representative CTC and PBMC isolated from a patient using our SASCA platform. Cells are stained for Hoechst, EpCAM, and an exclusion channel (CD45, CD34, CD11b). Scale bar is 10 μm.

patient 2. Similar purity levels were seen in isolated PBMC populations: 67% (6/9) and 100% (4/4) purity was achieved in patients 1 and 2, respectively (Fig. 3.9A-B). As seen in Fig. 3.9C, aspirated CTCs and PBMCs were phenotypically distinct upon fluorescent microscopy analysis. This data demonstrates that the SASCA platform performs well in its application of selecting specific cell subpopulations found within the heterogeneous environment of a patient sample.

A third patient sample was able to provide viable PCR data, demonstrating the platform's ability to acquire highly pure CTC samples. Briefly, cells from both populations were isolated from the same patient using VERSA purification and SASCA isolation. They then separately underwent RNA extraction. Gene expression analysis of CTC and PBMC populations showed expression of prostate specific markers exclusively in the CTC population, including the androgen receptor splice variant AR_V7, the presence of which has been suggested to act as a predictor of therapeutic resistance to both abiraterone acetate and enzalutamide. These results are concordant with the clinical narrative of the patient, who after undergoing disease progression on abiraterone, did not show a clinical response to enzalutamide. While only demonstrated in a single patient, these results are indicative

of the clinically relevant information that can be attained when using the SASCA platform to isolate and interrogate rare cell populations.

3.4 DISCUSSION

The SASCA platform leverages multiple technologies to improve purification of live rare cell populations. Here, we describe its application in CTC isolation from liquid biopsies. Our initial CTC enrichment is performed using the VERSA device, which employs EpCAM labeled paramagnetic beads to bind and extract EpCAM expressing cells. Although this method provides a high degree of enrichment, the purity is often insufficient for precise molecular analysis of CTC populations, including transcriptomic and genomic assays which have been shown to hold clinically relevant information. Acquiring viable, purified cells is imperative for reliable molecular characterization. The presence of contaminating background cells can mask changes occurring in rare cells, and obscure expression of potentially clinically relevant biomarkers. Additionally, the quality of genomic sequencing is enhanced with a higher purity cellular input, allowing visualization of copy number changes, insertions/deletions, gene rearrangements, and mutations. To overcome this obstacle, the SASCA platform detects and isolates rare cells on an individual basis, according to their phenotype. Live cells are collected and can be used for a wide variety of downstream analysis applications.

We sought to develop a strategy that integrates LOC bulk enrichment approaches with single-cell selection in order to improve rare cell purities. As we developed each component of this tandem approach, achieving high purity of isolated cell populations was our primary objective, potentially at the expense of cell yield and throughput. While there is potential for cell loss when transferring from the upstream LOC device to the SASCA, this step is still necessary to achieve the level of purity required for advanced downstream analytics. To this end, the SASCA was designed to maximize

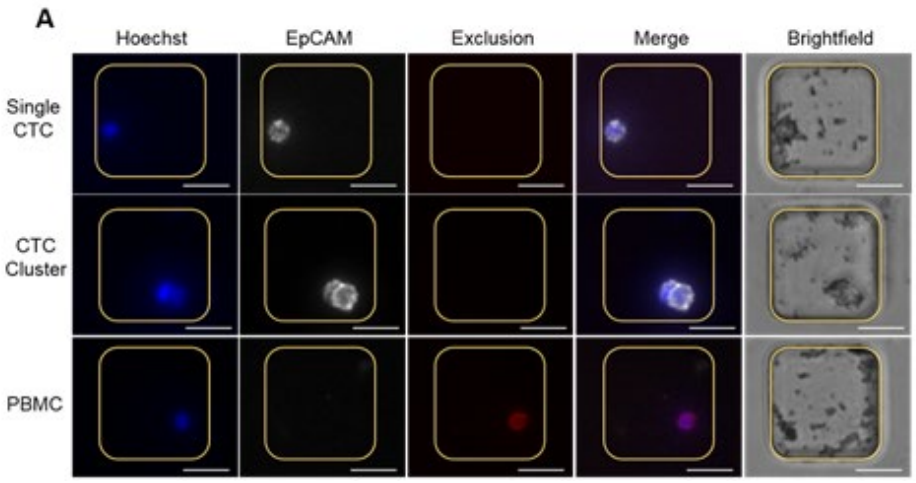

B

	Gene	CTC	PBMC
Prostate	AR_Exon 1/2	23.35	
	AR_Exon 4/5	23.66	
	AR_V7	32.75	
	AR_V9		
	KLK2	28.02	
	KLK3	28.73	
	TMPRSS2	27.25	
	HOXB13	28.27	
	FOLH1	32.30	
	NKX3.1	27.74	
House-keeping	CD45	29.29	31.01
	POLR2A	31.10	34.58
	P0	29.29	39.15

Figure 3.10. *Patient CTC RNA Analysis* – A) Images of representative CTCs and PBMCs isolated from whole blood of a patient with CRPC using the SASCA platform, after initial enrichment with the VERSA. Cells are stained for Hoechst, EpCAM, and an exclusion channel (CD45, CD34, CD11b). Scale bar is 25 μm. B) Matched qPCR gene expression profile of isolated CTC and PBMC populations from the same patient

output purity by integrating with a standard inverted microscope and a microwell array device. The platform itself is mounted to the z-axis of the microscope, improving the ease of sample navigation, which in turn improves sample throughput. Guided by the semi-automated software, the MA device facilitates confident rare-cell collection. Combining these features greatly increases output purity without sacrificing speed and recovery. Moreover, all of the components used to fabricate the SASCA platform are easily accessible and affordable, which could benefit other labs performing rare-cell studies.

Commercially available technologies exist for manipulating individual cells within a bulk population. Previous rare-cell studies have used CMMs to isolate and interrogate individual cells. CMMs come in manual, motorized, or automated models. The more motorized and automated a model is, the more expensive they are; automated models can cost up to $300 thousand, while the simplest mechanical models start at $750. However, cost is inversely proportional with regard to maneuverability and sample throughput. he SASCA was designed to get the best of both worlds. To achieve this, it was mounted to the z-axis of the microscope to circumvent these drawbacks. We

assess how the SASCA compares to other CMMs in Fig. 3.11, where we consider design parameters we found to be important.

Similar to the SASCA, The CellRaft System is a commercially available platform that integrates microscopes with MAs to isolate sub-populations of cells, and it also is mounted to the z-axis. CellRaft illustrates how the integration of microtechnology with microscopy can be leveraged to enable microscale applications and capabilities. While our study and CellRaft show the benefits of attaching a microscope modification to the z-axis users should verify with their microscope manufacturer to ensure it is able to withstand the addition of the SASCA platform.

In addition to our unique CMM mounting method and our semi-automated collection approach (AIMC), we have provided an optimized method of seeding heterogeneous samples into microwells. Previous attempts in the literature to optimize microwell seeding density have used a Poisson distribution to model how cells distribute to wells. Indeed, the Poisson distribution is very effective at modeling truly monodisperse suspensions of cells; however, in reality, cell suspensions typically also contain small clusters of cells as well. Therefore, we have chosen to use the Pólya-Aeppli distribution. The Pólya-Aeppli distribution models "Poisson delivery" of clusters of items (i.e., cells) where the number of items in the clusters follows a geometric distribution. This distribution modeled the experimental seeding data significantly better than the Poisson distribution. To our knowledge, we are the first to suggest and demonstrate application of the Pólya-Aeppli distribution to microwell seeding. Together, the tools described above were designed to be flexible and enable translation to alternative microscopy platforms, representing a significant contribution to rare cell enrichment technologies.

Although the single-cell isolation platform introduced here was used for circulating tumor cell interrogation, the capabilities of the SASCA are not limited to CTCs, as advanced single-cell isolation presents a variety of applications for rare cell studies. Traditionally, molecular biology has studied tissue slices (tumor, brain, embryo, etc.), blood, or populations of cultured cells, which have varying

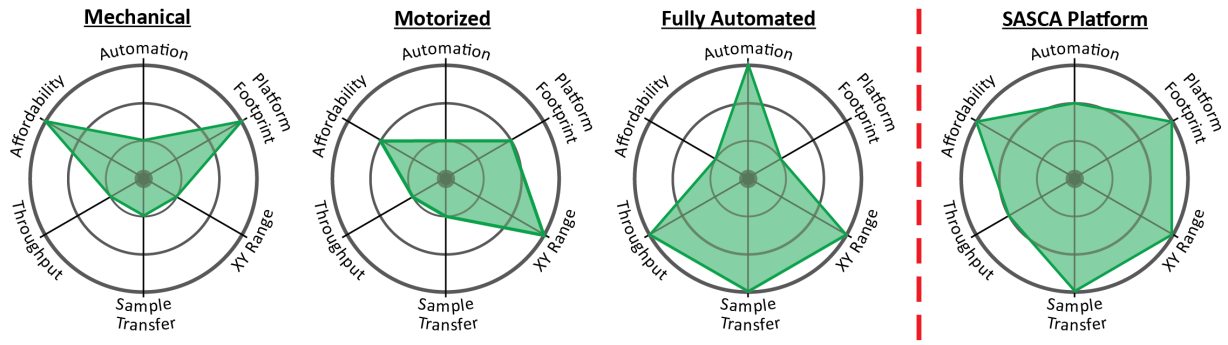

Figure 3.11. *Competing CMM Platforms* – Here, radar charts are used to illustrate how commercially available CMMs compare to the SASCA platform. The plots have three distinct levels; the innermost level represents a trait that has the least advantage compared to other platforms while the outermost level represents a trait that has the most advantage over others. Each tier of CMM provides its own degree of advantages, but only the SASCA provides the broadest range of benefits to scientists who wish to isolate individual or rare cells in an affordable manner.

levels of heterogeneity that researchers aim to better understand. For example, the analysis of neural progenitor cells could improve our understanding of developmental neural disease progression, but requires the ability to isolate sub-populations of neural cells. Advances such as microdissection and single cell isolation have allowed analysis of the heterogeneity of complex systems, which could provide new insights into disease progression[122]. As studies into the heterogeneity of diseased and developing tissue continue to increase, the SASCA provides an affordable, highly controllable platform to facilitate this research.

3.5 CONCLUSION

Improving the molecular evaluation of tumoral heterogeneity requires robust technology able to separate individual live cells for interrogation. To address these challenges, we have developed a platform that integrates low cost technologies, such as microwell arrays and manual micromanipulators, with real-time imaging software to isolate viable single cells based on phenotypic markers. Our platform successfully demonstrated enhanced purification of cell line

subpopulations, resulting in the enrichment of gene expression endpoints. When applied to patient samples, we were also able to enrich both prostate cancer CTC and PBMC populations. The SASCA platform presents a highly controlled, affordable method for the isolation of subpopulations of cells which could provide the specificity and reliability needed for rare-cell investigation.

4. Gradient stamps in well-plates for high-throughput tissue model assays

Jacob J. Tokar, Jay W. Warrick, Courtney K. Lynch, Benjamin W. Horman, Gavin T. Knight, Randolph S. Ashton, and David J. Beebe (To be submitted to Lab on a Chip)

Gradients are integral parts of physiology, providing signals of proliferation, migration, transformation, or death. Microfluidic gradient generators have produced interesting tissue models in the past. Unfortunately, such models have not been significantly implemented in the biomedical community. One argument as to why has been that such devices are intimidating, whereas established technologies – such as well-plates – are cheaper and already fully integrated with standard laboratory equipment. We address this issue here by designing gradient stamps that are easily integrated into standard well-plates. This provides a high-throughput design that is simple to operate and readily compatible with microscopes and other laboratory equipment. The well-plate gradient stamps were characterized by comparing fluorescent dextran gradients with modeled results. The platform was then validated by a series of unique gradients and tissue cultures. The gradient stamps were shown to induce directional neutrophil migration, cell proliferation along a nutrient gradient, and cancer cell response to chemotherapy drug gradients. Being modular, well-plate gradient stamps provide a versatile high-throughput platform for more complex tissue models.

4.1 INTRODUCTION

Gradients are important in all facets of human physiology. Gradients provide direction in development[123], immune response[124], reproduction[125], and cancer metastasis[126], among other systems. The dawn of microfluidics two decades ago brought with it an explosion of technologies capable of producing specific, controllable, static gradients across cell and tissue cultures[37,127,128]. The ability to produce a known, and controlled gradient allowed scientists to observe tissue response to specific concentrations and gradient shapes, providing a more systematic way of approaching *in vitro* tissue treatments. As more research begins to shift from *in vivo* animal models to *in vitro* models mimicking physiological conditions, continued advancement in gradient culture technology can provide a higher level of tissue system mimicry with regards to spatial response.

Depending on the system, biological gradients can come in different sizes, shapes, and time scales. Thanks to the physics of fluids at the sub-millimeter level, microfluidics provides a high level of control over these three parameters. In the past, gradients have been developed using microfluidic mixing trees or diffusion within a continuously perfused device[128–130]. Continuous flow devices provide the highest level of control over a gradient's shape and longevity, but they require inconvenient pumps and tubes to do so. Others have used pumpless, open microfluidic devices to generate gradients[28,131,132]. However, such techniques are better used in scenarios where only a short-term gradient is required. Active and passive gradient generating technologies have both provided new insight into biological systems, but they require special training to operate and highly engineered modifications to microscopes and plate readers to produce readouts. A simpler, more integrated microfluidic gradient technology would further improve the relevance of *in vitro* biomedical research.

Much of *in vitro* laboratory research is performed in well plates under specific media conditions. Because of this most laboratory equipment is designed to fit well plates and petri dishes. Recent

studies have shown the promise of integrating open microfluidic inserts with well-plates[18–22]. Given this, it seems viable to integrate microfluidic gradient generators into well-plates. Previous studies have demonstrated ways of producing gradients in modified well-plates[42,133]. While these techniques are useful, the idea of simply inserting a device into a well-plate to perform co-culture experiments has proven more appealing to researchers, given the popularity of the Transwell insert. Mimicking the simplicity of the Transwell can provide a blueprint on how to engineer a simple technology that is used by many.

In this study, we present a technique for engineering gradients within the wells of a well-plate by providing simple well inserts that require little training or expertise to use. These devices produce long-term, stable gradients that can be used to differentiate cells, study chemotaxis, or observe the drug response of cells along a gradient. Specifically, we demonstrate that microfluidic gradients can be integrated into well plate tissue cultures using simple hydrogel stamps, requiring no specialized pumps, tubing, or culture chamber while still providing a high-throughput platform. Using these stamps, we were able to observe biological reactions to chemotactic, nutrient, and chemotherapy drug gradients, illustrating the versatility of well plate gradient inserts.

4.2 MATERIALS AND METHODS

4.2.1 Fabricating Hydrogel Stamps

The hydrogel gradient stamps were fabricated from a milled PS insert and molded agarose hydrogel. The insert was designed in Solidworks CAD software and milled out of 4 mm thick polystyrene sheets using techniques described previously[64] (Fig 4.1). Top and bottom molds were also designed and fabricated to mold the hydrogel within the insert, producing a proper stamp. The PS insert gives a fully assembled stamp its rigid structure while also guiding diffusion. Stamps are

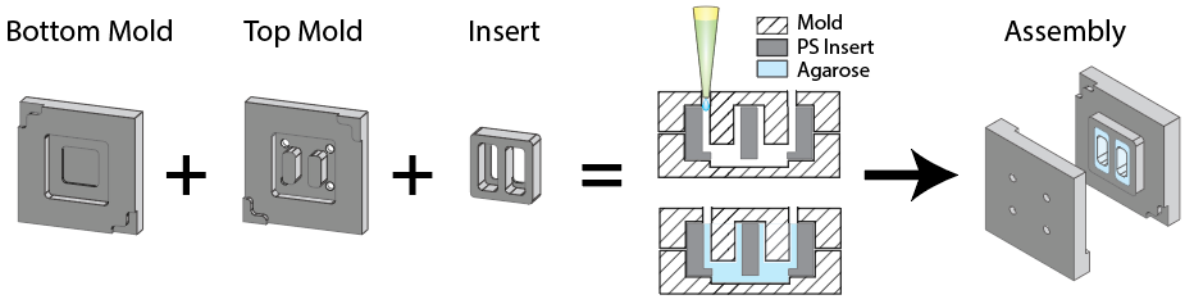

Figure 4.1. *Stamp Molding* – Stamp molds consist of three parts (bottom, top, and insert). When assembled the mold can be filled from one of four vents on the top mold. Agarose is allowed to cool and cure fully before removal of the molded stamp (agarose + insert).

molded using a 2 percent agarose solution (Sigma-Aldrich). Agarose was dissolved in 1x PBS solution by being heated to boiling in a microwave. The solution was then kept warm in a dry bath so it remained liquid until needed. For dextran diffusion characterization studies, the stamps were molded in a non-sterile environment, but for cell culture studies they were molded in a biosafety hood to maintain sterility of the cultures. Sterile stamps can be made a few days ahead of time and stored in a 50 mL conical tube filled with PBS until needed.

The stamp molding technique is similar to casting where molten material is filled into a mold of complex geometry and allowed to cool and harden into shape before it is released. As such, a p1000 micropipette was used to pipet liquid agarose slowly into one of four vents in the top mold until the mold was completely filled (~250 µL), indicated by excess agarose flowing out of the other three vents. Stamps were allowed to cure for up to 30 minutes before removal from the mold. Stamps can cure in as little as 10 minutes, but it was found that closer to 30 minutes resulted nearly a 100 percent success rate in removal from the mold compared to the 50-60 percent success rate of 10 minute cures. In addition, it was found that using hydrophobic material for the top and bottom molds greatly improved mold removal success as well. Specifically, top molds were made from PTFE (Grainger) or PDMS (Sylgard) and bottom molds were made exclusively from PTFE.

4.2.2 Modifying Well-plates

All well plate modifications made in this study were purely additive, not material was removed, allowing standard well plates to be used directly out of the package. Well plates were fitted with well bottom modifiers to hold stamps in proper alignment within the wells. Modifiers were designed in Solidworks and milled out of 4 mm thick polystyrene sheets (Goodfellow). Modifiers were attached to well bottoms using medical grade double sided adhesive (ARCare). Modifiers were properly aligned and attached using an assembly apparatus that was designed in Solidworks and 3D printed (Ultimaker). Experiments in this study used both plastic bottom (Falcon) and glass bottom (Cellvis) 12-well plates. Glass bottom well plates were used for automated time-lapse imaging during doxorubicin gradient experiments because of the superior flatness of the glass well bottoms, providing high quality and more consistent images.

4.2.3 Setting up Gradients

Hydrogel stamp gradients were set up at least 24 hours before they were needed to treat cells to allow for the gradients to fully form within the stamp. The specific gradient protocol depended on the diffusion coefficient (D_c) of the molecule of interest (MOI). One common element of each gradient protocol was the first nine hours of setup. To start the gradient setup, the source and sink wells are filled with 40 μL of their respective solution. Given the relatively large volume of the molded hydrogel, it takes several source/sink refresh steps to achieve a fully developed gradient. A fully developed gradient is defined as a gradient that has reached its maximum source concentration before the sink begins to increase in concentration, equilibrating the system.

Reaching a fully developed gradient within the stamps requires a source/sink refresh step every three hours over the first nine hours of gradient development for each of the MOIs used in this study. A refresh step involves the aspiration of old well contents and the addition of fresh source and sink solutions. Following the first nine hours, the gradient development protocol changes

depending on the D_c of the MOI. Larger molecules such as 10 kDa dextran and serum proteins require refresh steps only every 24 hours from the start of the gradient. Smaller molecules like IL-8 and Doxorubicin require refresh steps every 12 hours from the start of the gradient.

4.2.4. Neutrophil Migration

Neutrophils were extracted from consenting, healthy blood donors. Cells were purified and stained with Calcein AM for easier tracking. A glass bottom 12-well plate was assembled with well bottom modifiers and placed on ice to chill. Once chilled for a few minutes, the modified glass bottoms were coated with 100 µg/mL P-selectin solution for 60 minutes, remaining on ice. Following coating, the plate was removed from ice and the wells were rinsed with PBS. Next the wells were seeded with neutrophils at 200 x 10^3 cells/mL for 5 minutes, enough for the cells to lightly adhere. Once seeded, the cells were rinsed with EGM media to remove any unadhered cells, adding back a final well volume of 600 µL. Gradient stamps were placed, then the plate was immediately moved to a fluorescent microscope for time-lapse imaging. Images were taken every two minutes for X hours.

4.2.5 Serum Gradients

Growth factor proteins in serum have similar size and D_c values as 10 kDa dextran. Given this, serum gradients were set up using the same gradient protocol used during dextran gradient characterization of the gradient stamps. Serum gradient experiments were set up with experimental and control stamps using source media (DMEM with 20% FBS) and sink media (base DMEM). Control stamps were saturated with serum by filling both stamp wells with source media. Experimental stamps contained a serum gradient by filling the source and sink wells with source and sink media, respectively.

4.2.6 Doxorubicin Gradients

Doxorubicin chemotherapy drug diffuses nearly five times faster than 10 kDa dextran. Given this, doxorubicin gradients were set up and maintained using the same protocol as IL-8 gradients. Four distinct experimental gradients were set up for doxorubicin studies, with source concentrations of 50, 10, 2, and 0.4 μM. These concentrations produced gradient ranges with slight concentration overlap between the source and sink ranges of adjacent stamps, providing phenotypic observations along the full length of a concentration range contained within a single 12-well plate.

4.2.7 Cell Culture

For bulk cell culture MDA-MB-231 breast cancer cells (both GFP and wild-type) were cultured in DMEM media with 10% FBS, 1% pen./strep. antibiotics, and 4.5 mg/mL glucose. Experiments using 2D cultures within modified 12-well plates were cultured using the same media. Cells were seeded into 2D plates at a density of 50 x 10^3 cells/mL in 600 mL of solution.

For 3D culture in the modified well plates the cells were embedded in rat tail collagen I (BD Biosciences). Briefly, a plastic bottom 12-well plate was assembled with modifiers, sterilized and coated with Polyethyleneimine (PEI). After coating for 10 minutes, the PEI was aspirated and a Glutaraldehyde (GA) solution was then added, coating for 30 minutes. Following PEI/GA coating, the wells were thoroughly rinsed 3 times with DI water to ensure not cytotoxic, unbound GA was left in the well. The PEI binds to the plastic substrate of the well and modifier. The GA binds to the PEI and provides a binding site for collagen fibers, preventing gel contraction or delamination.

During the 30 minute GA coating a 4.5 mg/mL collagen solution was prepared on ice, diluting the 9 mg/mL stock collagen with enough cell solution to create a 75 x 10^3 cells/mL final solution, with the remaining dilution volume being HEPES buffer. The HEPES is added before the cells to neutralize the solution, making it more habitable for the cells. Once the solution is made it can be kept as a liquid on ice for some time, though it is usually seeded into the wells once they have been

washed of PEI/GA. The collagen is allowed to gel at room temperature for 10-15 minutes before it is moved to a cell culture incubator for 60-120 minutes. Once the collagen is fully solidified, the wells are filled with 600 mL of culture media.

4.2.8 Image Analysis

Raw images were pre-processed using JEX image analysis program (www.github.com/jaywarrick/JEX). In JEX, images were processed using a sequence of functions. All images had signal background and noise filtered out using the *Weighted Mean Filteri*ng function. Using the filtered image, cell maxima were detected in fluorescent images using the *Find Maxima Segmentation* function. To identify cell maxima in images that do not have adequate fluorescent maxima – doxorubicin staining for example – a step was added to generate maxima from two brightfield images taken ±5 μm from the focus plane. The *TIE Phase Calculator* function takes this two image z-stack, calculates the phase shift, and outputs a phase contrast image that was used to find maxima when fluorescent channel maxima were not viable options. Cell maxima were used as ROIs for the *Measure Maxima (v2)* function, which produces a data table for downstream analysis. For tracking cell migration, the cell maxima of a time-lapse were input into the *Track Points (LAP)* function, which produces a position table that was used to plot migration and motility. Once raw images were processed down to data tables, the tables were imported into RStudio and analyzed using custom written code.

4.3 RESULTS

4.3.1 Gradients in Well-plates

The well-plate gradient stamps were designed to produce symmetric gradient. The stamps also needed to be small enough to fit within the well of a 12-well plate (Fig. 4.2A). To produce a

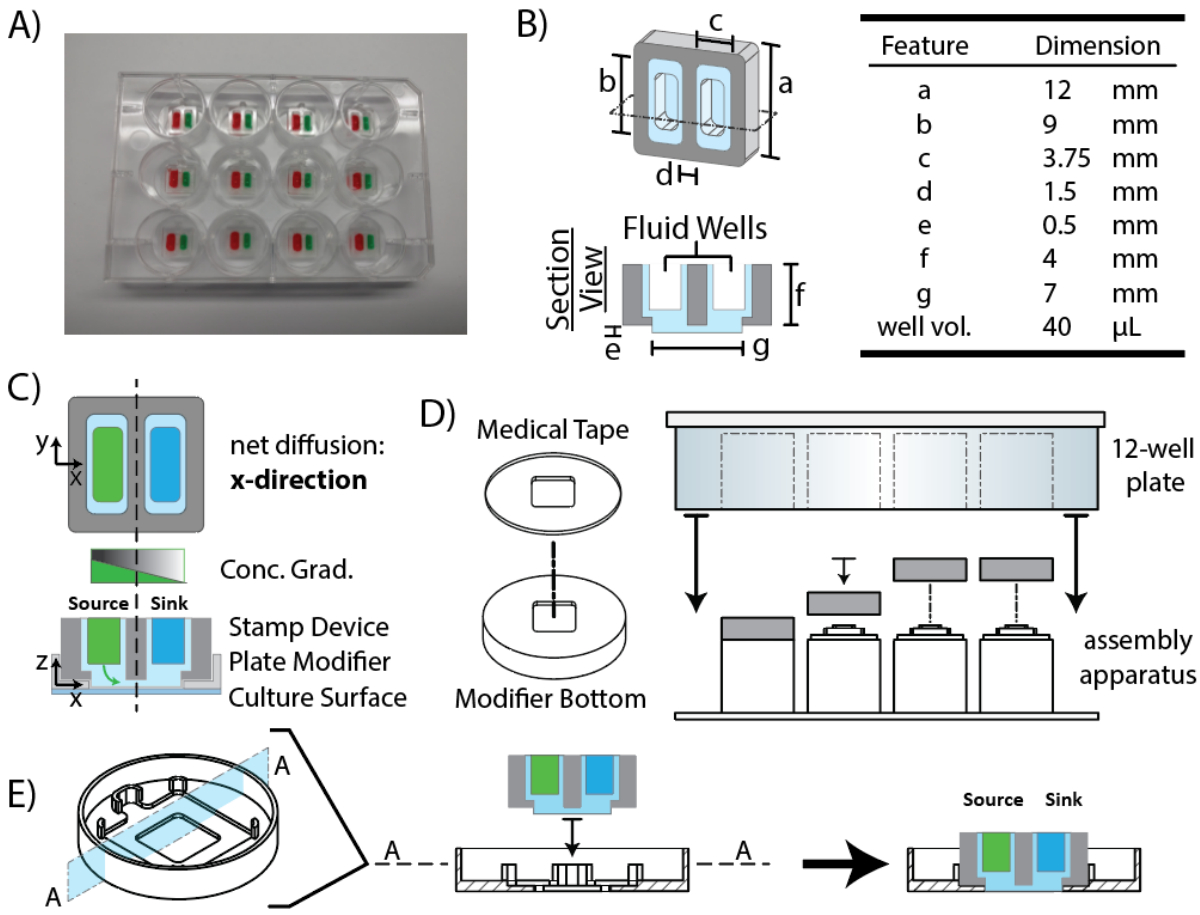

Figure 4.2. *Well-plate Gradient Stamps* – A) Stamps are designed to integrate with standard well-plates. B) Stamps have a symmetric design with two wells. C) Because of the symmetric design, net diffusion through the stamp is uni-directional from source to sink along the bottom protrusion of agarose. D) Well plates are upgraded using well-bottom modifiers, which are properly assembled using a 3D printed assembly apparatus. E) The well bottom modifier has a contour fit of the stamp, holding it just above the culture surface.

symmetric gradient, we mimicked a common microfluidic gradient design, placing two fluid reservoirs on either end of the device (Fig. 4.2B), generating a gradient between them, though standard microfluidic designs require constant flow[134]. Our fluid reservoirs are two rectangular fluid wells molded into the agarose that makes up the stamp. The wells are separated by a center wall milled out of the insert's polystyrene form. The center wall guides diffusion from the source well down through the agarose underneath the dividing wall towards the sink well (Fig. 4.2C). The

guided diffusion generates a gradient along the bottom of the agarose stamp which is placed directly over the tissue culture within a well.

Because the stamps were meant to remain over tissue cultures for an extended period, a method was needed to hold the stamps in place once they were placed. The solution devised was a well bottom modifier (Fig. 4.2D-E). Well bottom modifiers fit snuggly within the bottom of a 12-well plate well. The modifiers are permanently affixed to the well surface with medical grade double sided adhesive. To properly fit the stamp profile the modifiers were designed to have a square center hole that is just wide enough for the square agarose protrusion from the bottom of the stamp (Fig 4.2E). The stamp protrusion has a thickness of 500 μm. The medical adhesive has an approximate thickness of 142 μm. The square hole in the bottom modifier is milled to 450 μm thick, holding the bottom of the stamp approximately 92 microns above the culture surface, providing adequate clearance for cells as well as some tolerance for slight variance in modifier and tape thickness.

For ease of operation and downstream processing (i.e.- imaging, plate reader, etc.), it is essential for the modifiers to be properly aligned. To ensure precise alignment of the modifiers an assembly apparatus was designed in 3D modeling software and fabricated using a 3D printer (Fig. 4.2D). The apparatus has an array of cylindrical columns that are spaced to specifically fit into the wells of a 12-well plate. The top of each column features a sequence of steps that fit specific features of the well bottom modifiers, ensuring correct alignment while also providing structural support during assembly.

During assembly, the apparatus sits flat on a benchtop, the modifiers are turned upside-down and placed onto their respective apparatus column. Next, the adhesive is applied to the modifiers, then the 12-well plate is turned upside-down and slid over the modifier topped columns until the modifier adhesive is touching and fully adhered to the well-plate. The plate is removed from the assembly apparatus, rinsed with 70 percent ethanol and DI water, then it is dried for storage until

needed. When needed for an experiment, the modified plate is sterilized using 0_2 plasma treatment, though the plate can also be sterilized using UV light or excessive 70 percent ethanol rinse immediately preceding transfer into a biosafety hood.

Because the stamps rely purely on diffusion to produce gradients, generating steady gradients requires approximately 24 hours, depending on the diffusion coefficient (D_c) of the molecule of interest (MOI). Gradients can be set up directly over tissue cultures. However, if nearly instantaneous gradients are desired, gradients can be set up in a different plate a prior to the start of stamp treatment. Since instantaneous gradient application was desired for the experiments demonstrated in this study, a specialized "setup plate" was fabricated to hold stamps during the setup stage (Fig. 4.3A). The setup plate was made from an omni-tray and modifiers molded from PDMS. These modifiers were also attached to the omni-tray using the same medical grade double sided adhesive used for the well bottom modifiers. Sacrificial evaporation drops of PBS were pipetted between the PDMS modifiers to limit the level of evaporation from the stamps.

4.3.2 Gradient Modeling

During design of the stamps it was essential to know the nature of the gradient – gradient shape, concentration drop, etc. – that would develop within the stamp. To estimate the features of the gradient, finite element analysis software (FEA) was used to develop a 3D model of the diffusion of MOIs through the device. The FEA software (COMSOL) predicted a gradient with a sigmoidal shape, with it becoming relatively stable within approximately 24 hours. Of course, the speed of gradient develop depends on the diffusion coefficient of the molecule. Because gradient development was to be verified empirically with fluorescently labeled 10 kDa Dextran, initial modeling used the diffusion coefficient of 10 kDA dextran ($D_c = 75x10^{-12}$ m^2/s) in its calculations[135,136].

Agarose was specifically chosen in the design of the stamps because it is bioinert with respect to mammalian cells and is relatively inert chemically[137,138], meaning the gel would neither perturb the

tissue culture nor inhibit diffusion of a MOI via molecular forces. Agarose also has a relatively large pore size; a two percent wt./vol. agarose gel consists of a matrix with an average pore size between 150-250 nm in diameter, with less dense gels having even larger pores[139]. For a comparison, antibodies are one of the largest MOIs of potential use in such a system as proposed here, and their molecular diameter is 10-15 nm – just 10 percent that of the smallest pores within the agarose matrix – so the molecules diffusion would be negligibly restricted by the gel.

Given the negligible restriction to the diffusion of MOIs, the FAE model was simplified to strictly diffusion through an aqueous medium. Briefly, a 3D model of the molded hydrogel was drawn in Solidworks CAD software and imported into COMSOL. The entire system material was set to water. The wells were set as specific domains so their MOI concentration could be set individually with respect to the agarose domain. For most iterations of the model, the initial source was set to a concentration of 1 unit while the initial gel and sink domain concentrations were set to zero units. The diffusion coefficient was set to the specific D_c of the MOI in question, depending on the experiment; this enabled the tweaking of the experimental gradient protocol for specific gradient treatments.

Because this technology was motivated by simplicity, a method was needed to generate and maintain a fully developed gradient within the stamps similar to what can be achieved with active flow microfluidic gradient generators. The method conceived was to periodically refresh the source and sink well solutions a specifically determined time points. To model the periodic refreshment of the source and sink media, a chemical reaction equation was devised to mimic the near instantaneous replacement of old media with fresh media. The addition of fresh source media was mimicked by Equation 1 where the reaction rate coefficient, K, relatively quick at producing MOIs, increasing the source domain concentration back to 1 unit within a few minutes.

$$R_c = K(1 - c) \times series(t) \qquad Eq.\ 1$$

$$K = 0.01\ s^{-1} \qquad \textit{Reaction Constant}$$

In similar fashion, the addition of fresh sink media was mimicked using the same equation, but this time K was multiplied by -1, rapidly decreasing the source concentration back to zero, as shown in Equation 2.

$$R_c = (-1)K(c) \times series(t) \qquad \textit{Eq. 2}$$

Being time dependent, the equations contain a constant that is set to either one or zero by a time series. When the constant is zero, the equation results to zero, meaning it has no impact on the concentration of the well domains. However, when the constant is set to one the reaction equation is initiated, resetting the well domain concentrations for a brief time before the equation is again halted when the constant switches back to zero. Once the reaction equations were set up, various gradient protocols could be tested, enabling investigation of their effect on the development and consistency over a multi-day period. The various time series explored are listed in Appendix 2.

Several iterations of a well refresh timeline were investigated, the development and long-term consistency of each were compared to one another. Through these iterations it was found that a fully developed, consistent gradient can be produced within 24 hours using a specific setup protocol. For the 10 kDa dextran it was found that a relatively steady, long-term gradient could be created in the symmetric stamp design by refreshing the wells 3, 6, and 9 hours after starting the gradient diffusion, then the wells only required a refresh step at every 24 hour mark to maintain a consistent gradient over multiple days (Fig. 4.3B-C). Once this protocol was determined, it was found that only minor tweaks were required for MOIs with faster diffusion coefficients.

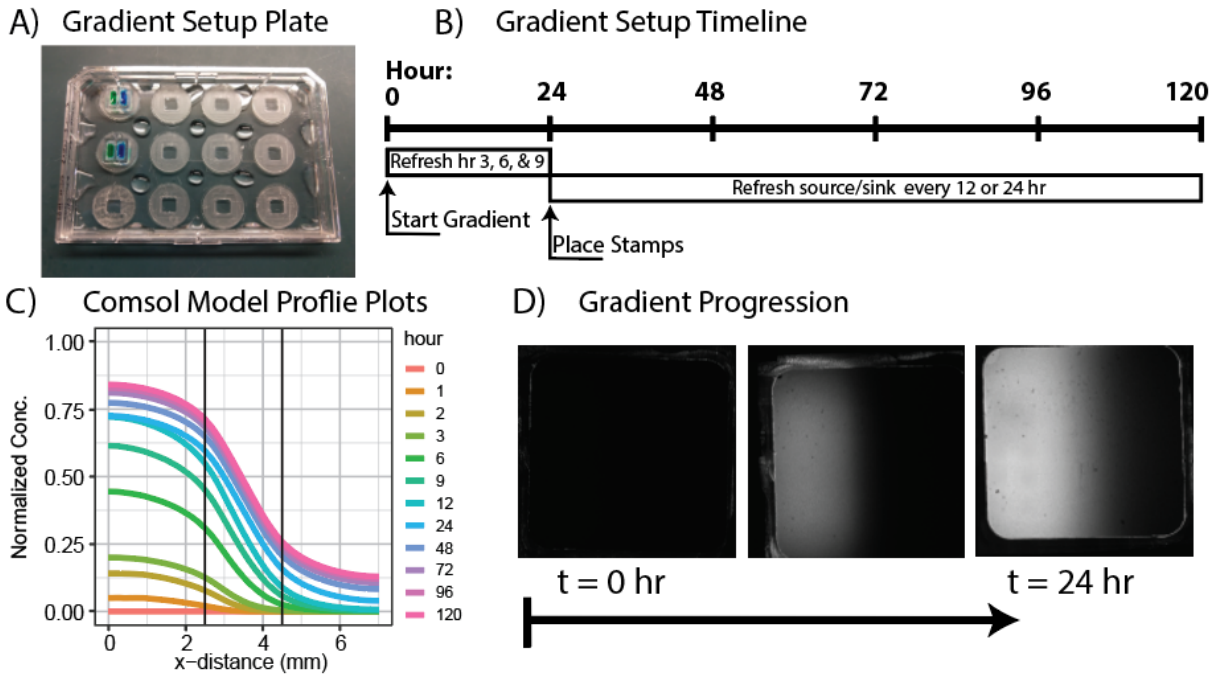

Figure 4.3. *Gradient Development* – A) Gradients were developed in a setup plate 24 hours prior to start of treatment, enabling rapid introduction of steady gradients. B) A standard gradient protocol was developed, generating gradients within 24 hours and maintaining them over multiple days of treatment. C) The gradient protocol was modeled in COMSOL to provide a benchmark for empirical characterization. D) Dextran gradient generation were imaged using a confocal microscope.

4.3.3 Gradient Characterization

Once a viable gradient protocol was determined within the model it had to be tested empirically. This was done so using a 10 kDa dextran because its diffusion coefficient is similar to that of various growth factor and morphogen proteins[140–142]. To track diffusion of the dextran, it was labeled with Alexa-Flour 560 so the fluorescence within the gel could be imaged. Because of where the source and sink wells are situated – partially above the gradient region of the stamp – the gradient stamps could not be imaged with a standard inverted microscope. This is because standard fluorescent microscopes excite the entire z column, resulting in high background fluorescence from the source well, skewing quantification of relative fluorescence.

To address dextran imaging issues, a confocal microscope was used because it only excites the dextran probes within the focal plane of the microscope, allowing imaging of only the gradient

region at the bottom of the stamp (Fig. 4.3D). To calculate relative gradient concentration compared to initial source solution, control images were taken in wells without stamps. The control wells were filled with 100 μL of the source dextran solution; enough for the liquid column to be greater than 500 microns. The fluorescence of each experimental image was normalized to the fluorescence of the control image, providing a concentration ratio for each pixel along the x-axis of the gradient. This concentration ratio was plotted against x-distance along the gradient and compared to the concentration plots produced by the FEA model.

First, it had to be confirmed that the gradient developed as expected by the model, which meant tracking the first 24 hours of the gradient. The first 24 hours of gradient setup were tracked within the setup plate, showing that the gradient develops in a similar fashion to what was estimated by the model (Fig. 4.4A-B). Second, it had to be confirmed that the gradient remained stable for multiple days as expected by the model. First this was done by continuing to track and image the gradient for several days more days within the setup plate. As expected, the gradient appears to remain consistent for at least four days following the setup day (Fig. 4.4C). When gradient formation was tracked in the well plates it was found that a gradient of similar shape and stability still forms, though it is slightly more dilute (Fig. 4.4D-F).

The advantage of the well plate gradient stamps is their modularity, allowing gradients to be set up in a different plate before placing on the tissue cultures, providing a near instantaneous gradient. To characterize how the movement of the stamps from the setup plate to the well plate cultures might disrupt gradient stability another dextran gradient experiment was devised. As before, gradients were set up within stamps over the first 24 hours in the setup plate. After the 24 hours of gradient setup, the source and sink wells of each stamp were refreshed before they were placed into a modified 12-well plate for further tracking of the gradient. To replicate a tissue culture experiment, the wells of the of the modified plate were filled with 500 μL of PBS prior to placing the stamps. An attempt was made to aspirate well liquid before placing the stamps in order to prevent

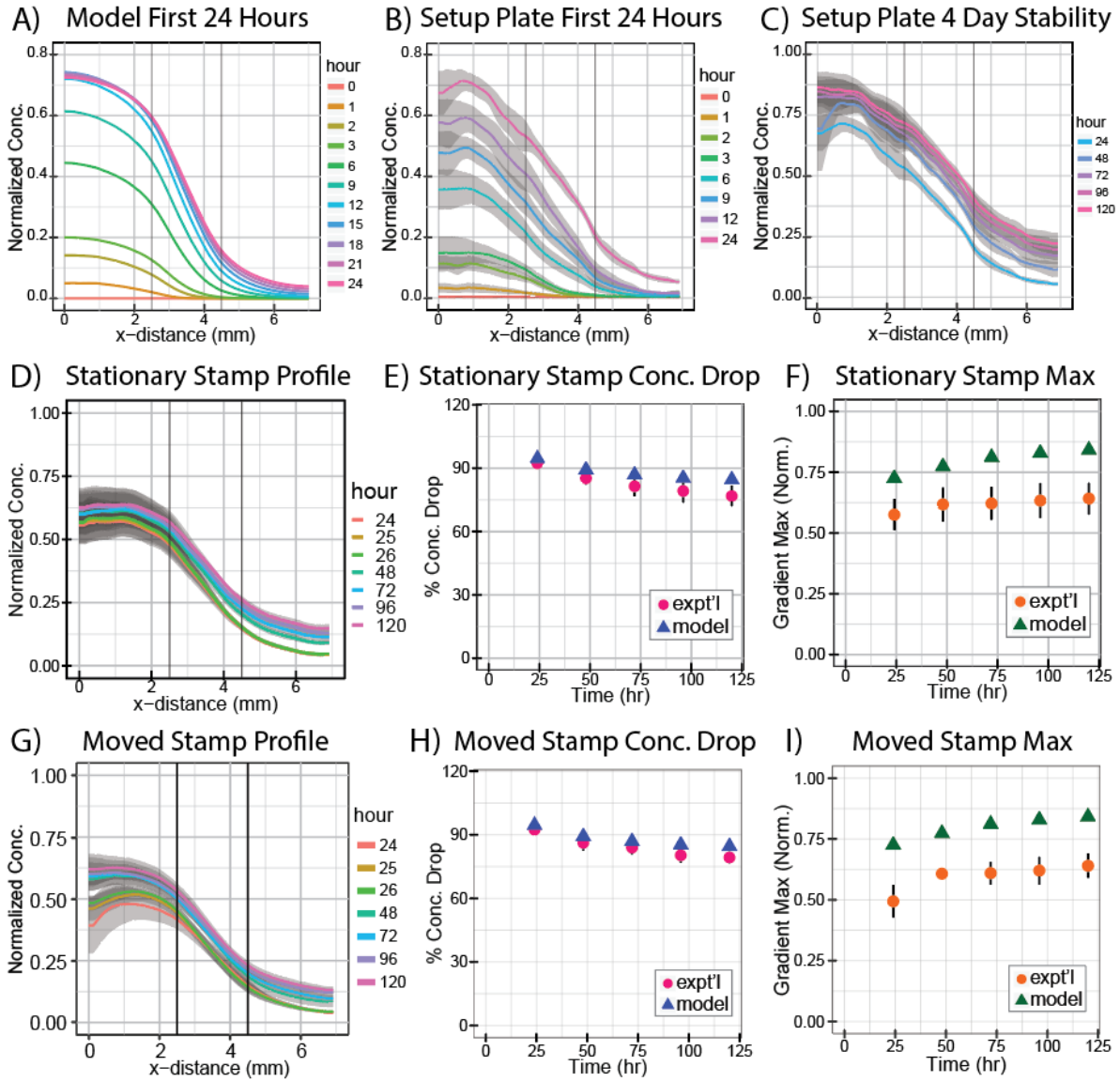

Figure. 4.4. *Experimental Gradient Characterization* – A & B) Gradient generation was verified empirically by comparing the model to how the dextran gradient set up within 24 hours. C) The dextran gradient was then maintained for another four days to confirm stability. Gradients in (B) & (C) were monitored in the setup plate. D) Stationary gradient stamps within modified well plates were then monitored over 5 days. E & F) The stationary stamp gradients were compared to the model by looking at the gradient concentration drop and maximum concentration. G-I) To confirm stamps moved from the setup plate to the culture plate maintained steady gradients, Dextran gradients were again used, comparing gradient profile, concentration drop, a gradient maximum.

any dilution of the gradient, but bubbles often became trapped beneath the stamps. Placing the stamps into wells filled with liquid drastically reduced bubble trapping.

For the next four days following stamp placement the source and sink were refreshed every 24 hours. Immediately following each refreshment, the Dextran gradient was imaged. The gradient was found to acceptably steady over the multi-day period (Fig. 4.4G-H), though the gradient does appear to require a couple hours to stabilize after the stamps are transferred to the plate. Once the gradient stabilizes the overall maximum gradient concentration within the transferred stamps replicates what was observed in the stationary stamps (Fig. 4.4F & I). Confident that the stamps provide steady gradients over a multi-day treatment, experiments were devised to test these gradients biologically.

4.3.4 Biological Gradients

The immune response of neutrophils to gradients of IL-8 is a highly characterized physiological gradient[28,131,132,143]. To confirm the gradient stamps can replicate thoroughly established results, IL-8 gradients were developed within the molded hydrogels. Because IL-8 has a diffusion coefficient (D_c = 250 x10^{-12} m^2/s) that is approximately 3.3x faster than that of 10 kDa dextran[144], the diffusion model was used to tweak the gradient protocol. It was determined that the IL-8 gradient would set up properly and remain consistent if the source and sink wells were refreshed at hour 3, 6, 9, and 12, and then at every 12 hour interval following. However, given that neutrophils migrate relatively quickly the gradients did not require more than a final refreshment at hour 24 before they were placed and migration was tracked.

Human neutrophils enriched from healthy donors were seeded into a p-selectin coated glass bottom 12-well plate that had been fitted with modifiers. Migration was tracked using a time-lapse sequence for 60 minutes, with images taken every two minutes. Neutrophils were labeled with Calcein AM so they could be tracked fluorescently. Experiments demonstrated directional migration of neutrophils up an IL-8 gradient, validating that well plate gradient stamps are a viable option for migration studies (Fig. 4.5A).

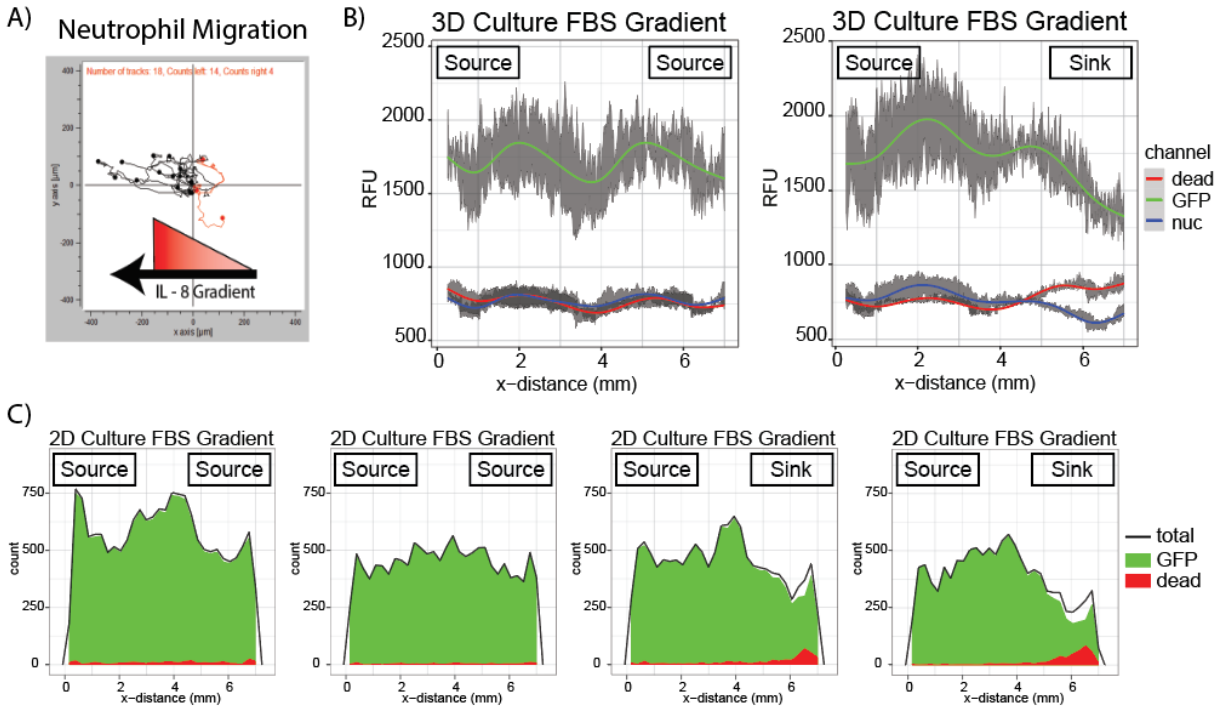

Figure 4.5. *Basic Biological Gradients* – A) Well-plate gradient stamps can induce neutrophil chemotaxis in response to IL-8 gradients. B & C) Well-plate gradient stamps can induce a spatially dependent proliferation curve in both 3D and 2D tumor cultures.

As another simple biological test of gradient formation, cell proliferation and cell death were tracked in 3D cell cultures subjected to gradients of serum, which contains growth factors and other nutrients that enable cell proliferation. Here human breast cancer cell line cells (MDA-MB-231) were seeded in 3D collagen I gels. The cultures were allowed to grow for 24 hours before they were pre-treated prior to gradient treatment. Control cultures were pre-treated with normal 10% FBS media, whereas experimental – serum starved – cells were treated with 2% FBS media for one hour and then serum free media for an additional hour prior to stamp placement.

FBS gradients were generated within stamps using a source media with 20% FBS and a sink media with no FBS using the same protocol as with the 10 kDa dextran gradients. Control stamps were developed along with the experimental stamps, though for these stamps both wells received 20% FBS media. After two days culturing beneath the serum stamps, a clear gradient in cell proliferation had developed within the collagen gels. Ethidium Homodimer staining showed that

cells beneath the sinks of the stamps had a significantly larger ratio of dead cells when compared to cells beneath the source (Fig. 4.5B). This experiment was repeated in 2D cultures using the same cell line and similar results were observed (Fig 4.5C). Once it was established that the stamps could invoke a gradient response in tissue cultures, more complex gradient treatments were explored.

4.3.5 Chemotherapy Gradients

Doxorubicin is a well-established chemotherapy drug that has been around for decades[145]. The drugs effect on cultures of MDA-MB-231 breast cancer cells has been extensively studied[146,147]. The cells have shown interesting migratory behavior along doxorubicin gradients within traditional microfluidic devices[148]. This model presents an interesting and thorough way to further test the efficacy of the well-plate gradient stamps. To this end, the FEA model was again altered to adjust for the diffusion coefficient of Doxorubicin. Because Doxorubicin has a diffusion coefficient that is approximately 4.8x faster (D_c = 358 x10^{-12} m^2/s) than that of 10 kDa dextran, it was anticipated that robust doxorubicin gradients would require a protocol similar to that of IL-8 gradients. In fact, the model suggested that the IL-8 gradient protocol would also produce a long-term Doxorubicin gradient, so stamps were set up in the same manner.

All doxorubicin gradient experiments were performed using 2D cultures of MDA-MB-231 cells. As with the neutrophil migration experiment, well bottom modifiers were assembled into a glass bottom 12-well plate. The plate was sterilized O_2 plasma and seeded with MDA-MB-231 breast cancer cells. Cells were allowed to culture overnight prior to stamp placement. Dox gradient stamps were started at least 24 hours prior to the beginning of gradient treatment of the cells. Immediately following placement of the stamps, the plate was moved to an on-stage incubator affixed to the microscope stage. The incubator maintains temperature, heat, and CO_2 levels over the culture allowing them to remain stable over a long-term time-lapse imaging sequence.

The 12-well plate was split up into four conditions, each with three replicates. To achieve a significant enough concentration range to observe the transition from fully viable to fully dead cell populations, the source concentrations for each condition were 50, 10, 2, and 0.4 μM, respectively. Note that each subsequent source concentration is a fifth of the previous source concentration. This provides some concentration overlap between stamp conditions since the concentration drop along the stamp gradients is approximately six-fold. By slightly overlapping concentration ranges, the consistency of gradient maintenance for multi-day cultures could be confirmed further by comparing cell phenotypes in these areas.

The cultures remained under the stamps for 48 hours. Stamp wells were refreshed every 12 hours – per the protocol – and images of the cultures were taken every 20 minutes. The cells expressed GFP so brightfield and fluorescent images were each taken so viability and motility could be observed over time (Fig. 4.6A). Most cells along the length of the 50 μM gradient stamps were dead by the end of the treatment as determined by their high circularity and minimal motility (Fig. 6 column 1). Conversely, most cells along the length of the 0.4 μM gradient were viable and quite active, illustrated by their low circularity and high motility (Fig. 6 Column 4). The greatest change in viability came between the 10 and 2 μM gradient stamps, with the source region of the former producing mostly dead cells whereas the sink region of the latter producing mostly viable cells (Fig. 4.6 column 2 & 3). Interestingly, the normalized local cell counts and cell motility curves followed similar trends along the length of the full concentration range, while cell circularity followed an opposite trend (Fig. 4.6B-D). It should be noted that while cell migration was observed, there was no significant directional migration (Fig 4.6E).

Once the viability transition range was determined, a second experiment was designed to observe drug uptake within the cells after 24 hours of treatment. Conveniently, Doxorubicin is itself slightly fluorescent, exciting around 485 nm and emitting around 607 nm[149,150]. This allowed fluorescent imaging of doxorubicin uptake by cells after they were treated. Non-GFP MDA-MB-231

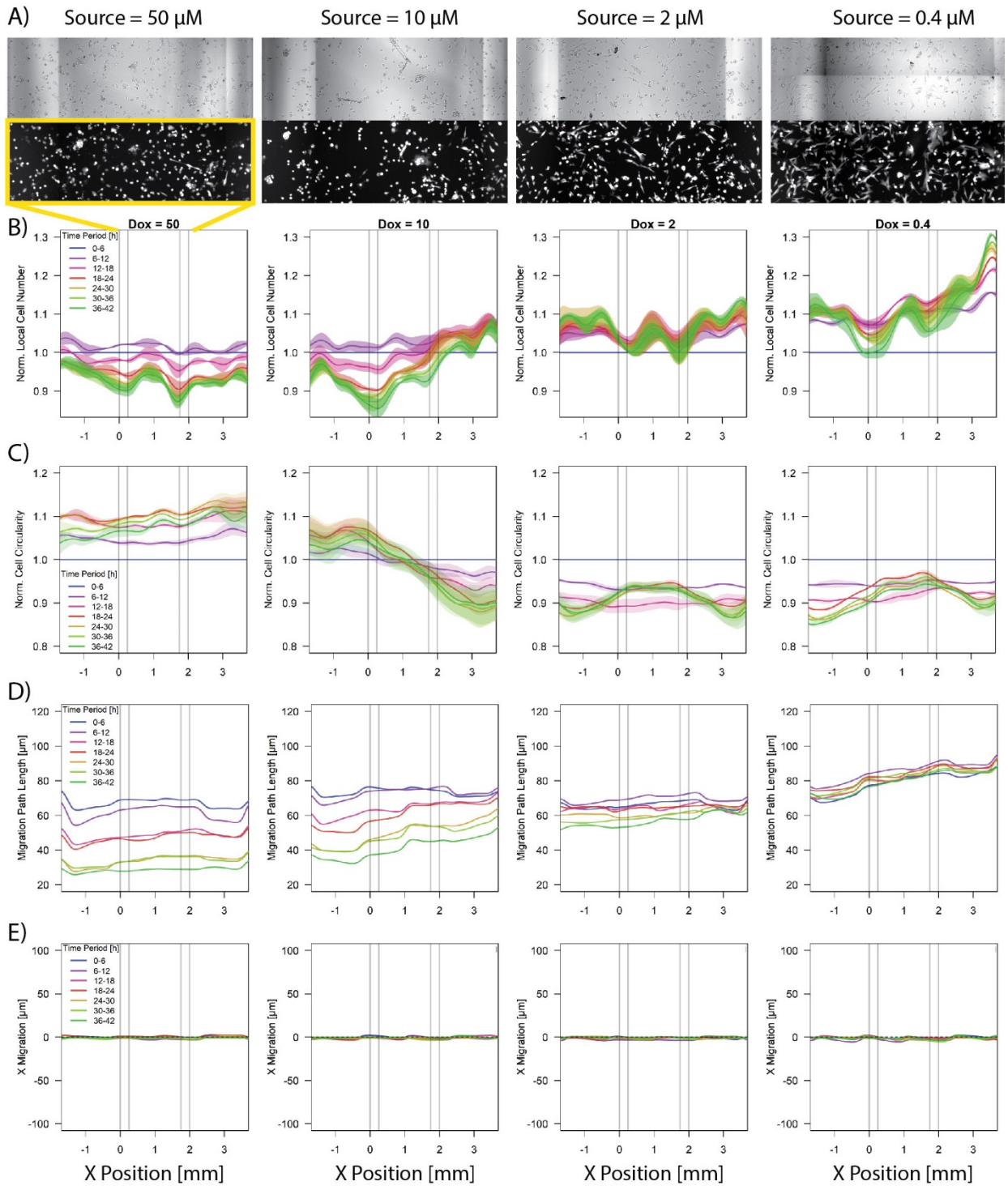

Figure 4.6. *Cancer Cell Dose Response* – A) Dox gradient stamps induce dose dependent phenotypes after two days of treatment. A gradient dependent response is observed in cell proliferation (B), cell viability/circularity (C), and overall cell motility (D). However, no significant directional migration was observed under any gradient condition.

cells were used to prevent any fluorescent bleed through from the GFP, given the low fluorescent intensity of doxorubicin. This time only two gradient stamp conditions were prepared, 10 and 2 μM because the viability transition zone was observed along the gradients of the conditions

After the treatment the stamps were removed, the cells were rinsed with PBS and imaged (Fig. 4.7A). By measuring the Doxorubicin fluorescent intensity within the nucleus of each cell, a gradient of drug uptake was observed, following that which would be expected within the stamps (Fig. 4.7B). As expected, the cells treated with 2 μM Doxorubicin gradients exhibited very low uptake of the drug compared to the 10 μM treated cells. To further investigate the effect of the doxorubicin gradient, the cells were again washed, fixed, permeabilized, and stained for nuclei (Hoechst), cytoplasmic actin (phalloidin) and DNA damage (gamma-H2A.X) (Fig. 4.7C). Again, a spatial response to the Doxorubicin gradient was observed in the intensity of DNA damage along the length of the cultures with the low concentration stamps exhibiting lower DNA damage (Fig. 4.7D). Interestingly, while the low concentration stamps showed a near negligible gradient of drug uptake, the corresponding gamma-H2A.X staining showed a more significant gradient of DNA damage.

4.4 DISCUSSION

The hydrogel stamps demonstrated a way standard well-plates can be upgraded in a simple fashion. Gradient stamps were shown to be steady over multiple days of culture, though the concentration drop along the gradient is not as significant as predicted by the model. This could be due to slight dilution of the MOI out of the stamp. The system was designed with some fluid volume beneath the stamp to provide adequate clearance for the tissue cultures. The system is also somewhat open to the bulk media because the fit between the stamps and the modifiers was built with a 50 micron tolerance around the walls of the stamps. This means that, while the well bottom

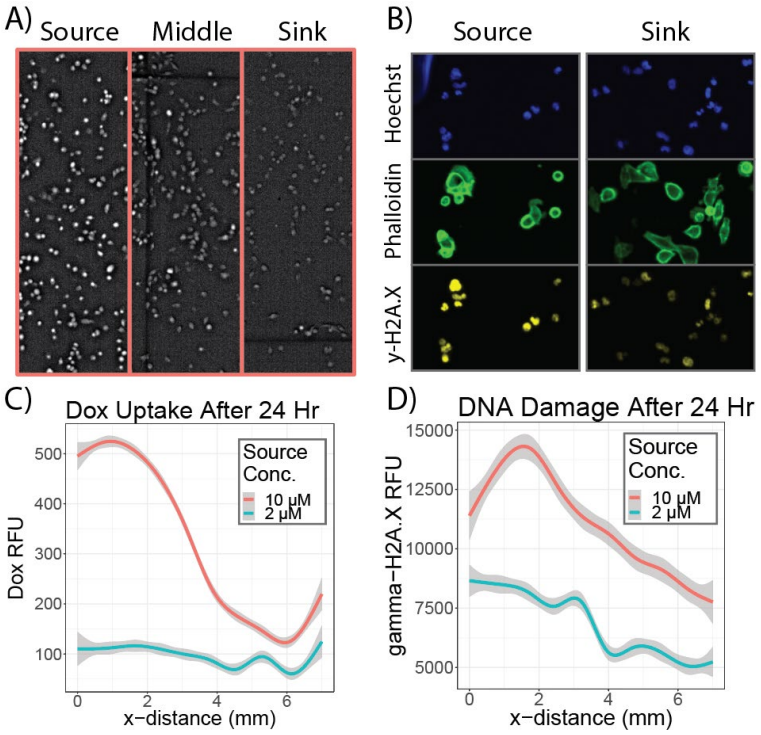

Figure 4.7. *Drug Uptake and DNA Damage* – A & C) Doxorubicin uptake of breast cancer cells displayed a gradient of DNA intercalation in response to the chemotherapy gradient. B & D) Furthermore, DNA damage was also found to be gradient dependent by measuring gamma-H2A.X expression with cell nuclei.

modifiers shield the agarose protrusion feature of the stamps from most of the bulk media dilution, there is some fluid interaction between the bulk media and the media beneath the stamps.

Even with the slight dilution of the maximum gradient concentration, the stamps provided initial evidence of a biological response to simple gradients. Neutrophils migrated up an IL-8 gradient, proving that chemotaxis measurements can be acquired during immune response studies. Tissue cultures of a highly invasive breast cancer cell line showed to respond to nutrient gradients with increased proliferation under the source and increased cell death under the sink, compared to nutrient rich controls. These results were duplicated in both 3D and 2D cell cultures, demonstrating the versatility of well-plate stamps.

To further validate the capabilities of well-plate gradient stamps, an effort was made to replicate previous studies treating breast cancer cell lines with doxorubicin chemotherapy drug gradients. These experiments were motivated by a 2013 study by the Robert Austin group where a traditional flow induced gradient generator was used[148]. A series of four gradient conditions were set up to

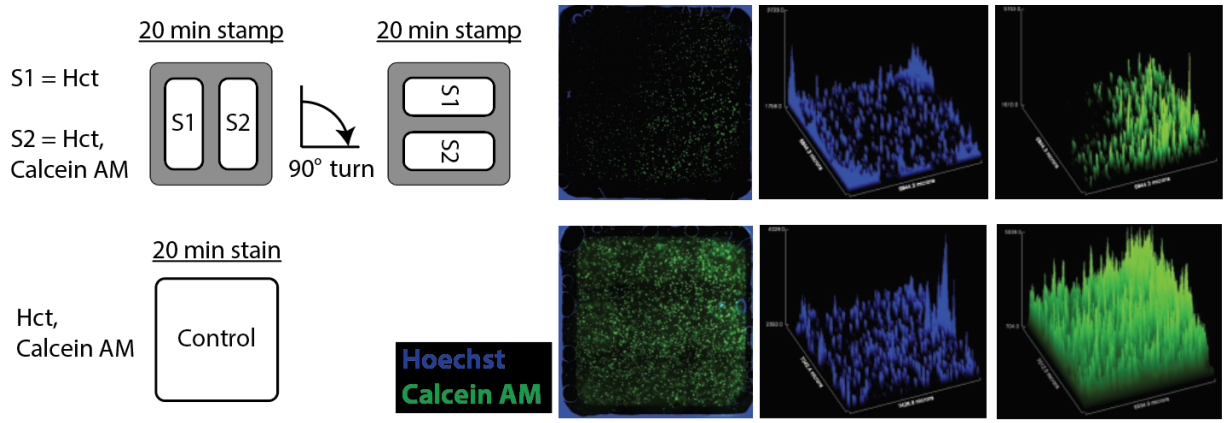

Figure 4.8. *Modular Stamps* – The well-plate gradient stamps were designed to be modular, which gives them the unique ability to be quickly exchanged with different gradients or to be rotated, providing dynamic gradient treatments to tissue cultures.

produce a concentration range that drops 10-fold within a single 12-well plate. As show previously, the highest concentrations greatly perturbed the cells, resulting in little cell proliferation and motility while the lowest concentrations showed little to no inhibition on the cell proliferation or motility. Further investigation correlated gradients of doxorubicin uptake with gradients of DNA damage within treated cells. However, contrary to the Austin group's 2013 study, no significant directional migration was observed along any of the gradient conditions. This finding might be explained by the low number of cells sampled in the 2013 study (n = 12) whereas we sampled thousands of cells along the concentration range.

Given that these stamps are modular, they can be used to produce rather complex gradient treatments. Tissue cultures can be treated with a sequence of stamps, each containing a different MOI gradient or an opposing gradient. In fact, being square shaped, the stamps can be rotated 90, 180, or 270 degrees after initial treatment as demonstrated by simple staining gradients in Fig. 4.8. Having this capability in treatment options could enable some interesting high throughput studies in the future given what others have previously shown with gradient stamps[151,152].

4.5 CONCLUSION

Microfluidic gradient generators are highly useful technologies, but they are often inaccessible to the broader biomedical field, limiting their impact. Engineering microfluidic inserts for standard well plates is proving to be a burgeoning area of study. Here we demonstrated a simple microfluidic gradient stamp designed to integrate with well-plates, taking advantage of the high-throughput format and the ubiquity of well-plate compatible laboratory equipment. The well-plate gradient stamps were able to produce several different biological gradients and corresponding spatial responses, validating the utility of the design.

5. Spatial-temporal differentiation of neural organoids using morphogen gradient stamps in well plates

Work done in collaboration with Gavin T. Knight, Jay W. Warrick, David J. Beebe, and Randolph S. Ashton

Neural tissue models are key tools in the study of developmental and neurodegenerative disease. Most research in this area is done using animal and 2D tissue culture models, however, recent developments have demonstrated the capabilities of neural spheroids and microfluidic tissue models. Microfluidics offers many capabilities when modeling tissue because of fluid physics on the microscale as well as the relative dimensions of tissue microevironments. Here we present a high-throughput microfluidic system for developing highly organized neural organoids. Previous work has demonstrated the capabilities of well-plate gradient stamps. In this study we integrate these concepts with an established neural stem cell engineering platform, which generates neural rosettes on micropatterned glass substrates. By combining these technologies, we were able to spatially differentiate neural organoid arrays with morphogen gradients of Sonic Hedgehog (Shh), as demonstrated by spatially dependent expression of ventral patterning markers, Olig2 and Nkx6.1. In future studies we hope to develop neural disease organoids and investigate taxological effects of various chemicals on proper organoid development.

5.1 INTRODUCTION

Current human central nervous system (CNS) models make use of genetically altered animal models or simple neural stem cell (NSC) cultures[153,154]. Such standard practices have led to significant advances in neural disease understanding. However, there are well accepted limitations to both animal and 2D tissue culture models[155]. Such limitations for animal models include lack of human physiological relevance and ethical issues, while 2D cell cultures lack essential structural and spatial elements of tissue microenvironments. To address these issues, scientists have recently been exploring the capabilities of more complex co-culture and 3D tissue culture models, such as neural spheroids and microfluidic co-culture studies[156,157].

Here we present a hybrid neural model system that combines the advantages of neural organoids with microfluidic gradients for unique, spatial differentiation of NSC tissues. The Ashton group has previously demonstrated a tissue engineering technique to produce a neural tube microarray (NTM) on a patterned glass slide[158,159]. They have further developed the technique and are now able to produce single neural rosettes within each patterned substrate of a NTM[160]. Neural rosettes are self-organized NSC tissues that develop polarized structures with a central luminal space, mimicking the tissue structure of a developing CNS *in vivo*.

To further increase the physiological complexity of these rosette organoids, we developed a platform for treating the tissues with microfluidic morphogen gradients. To treat tissues in a high-throughput manner, slight modifications were made to the well-plate gradient stamp platform demonstrated previously (Chapter 4). We were able to demonstrate that steady gradients can be generated in the modified stamps and maintained over time. Moreover, it was observed that NTMs can remain viable beneath the stamps, developing rosettes and responding phenotypically to Shh gradients. Such a model could prove useful for neurodevelopment models in areas such as toxicology or disease.

5.2 MATERIALS AND METHODS

5.2.1 Modifying Well-plates

The bottom of the well-plates were milled using a Tormach 770 CNC milling machine. The well bottoms were milled with a 1/16th inch, 2 flute mill bit (Performance Micro Tool) so a micropatterned glass slide can be fitted from the bottom. The milled well plates were cleaned thoroughly following milling to remove coolant and machine oil residue. The modified plate was sterilized and assembled in a sterile biosafety hood. Assembly of the plate used a similar assembly apparatus demonstrated previously (Chapter 4). The well bottom modifiers were fitted upside-down on the assembly apparatus and the double sided adhesive was applied to the bottom of the modifiers. The plate was then slid over the columns of the assemble apparatus, affixing the modifiers to the well bottoms. While still on the assemble apparatus, double sided adhesive was used to attach the patterned glass coverslip to the bottom of the plate, centered beneath each well.

5.2.2 Molding Hydrogel Stamps

Stamps were molded in the same fashion as demonstrated previously (Chapter 4). Briefly, the stamp inserts fit into the top and bottom molds, into which molten agarose (2% wt/vol) was pipetted until overflowing out of each of the mold vents (~250 µL). Stamps were allowed to cure for up to 30 minutes before removal from the molds. Stamps intended for dextran diffusion experiments were molded in non-sterile conditions, though stamps intended for biological experiments were molded within a sterile biosafety hood. Stamps were often molded a few days in advance, so they were kept hydrated in a 50 mL conical filled with sterile 1x PBS until needed.

5.2.3 Micropatterned Array Fabrication

The NTMs were cultured on micropatterned glass coverslips (1.5) that are 18 mm square (Fisherbrand). The specialized culture substrates were fabricated using previously published techniques, which use PDMS stamps to micro-contact print molecular patterns onto the coverslips[159–161]. Prior to feature stamping, the glass was coated with a 30 nm base later of Ti and a 180 nm layer of Au. The PDMS stamps were coated with ω-mercaptoundecyl bromoisobutyrate (2 mM in 100% ethanol) and dried under inert gas before being stamped onto the coverslip. Functionalized PEG brushes – PEG-MA and PEG-MEMA – were grown onto the patterned substrates using Surface-initiated atom-transfer radical-polymerization (SI-ATRP), which was allowed to react for 16 hours at room temperature. Following ATRP, surfaces were blown dry and rinsed with ethanol and water before again being dried with inert gas. The coverslips were rinsed a final time and dried before being assembled onto the well-plate. To enable patterned cell adhesion, the substrates were coated with 0.083 mg/mL Matrigel (WiCell) in DMEM/F-12 (Thermo Fisher) overnight at 37^0C.

5.2.4 Generation of Micropatterned Neuroepithelial Tissue

Two different hESC lines were used in this study – WA09 (H9) and HUES3 – which were obtained from WiCell and the Harvard Stem Cell Institute, respectively. The cells were maintained in Essential eight medium (E8) on Matrigel coated tissue culture plates. Accutase (Thermo Fisher) was used to dissociate cells for passage. To derive neuroepithelial phenotypes from the hPSCs, the previously established E6 protocol was used[158]. After one day of the E6 treatment, FGF8 was added to the media. The following day – day two of E6 treatment – CHIR boost was added for the final three days.

After a total five days of the E6 protocol, the cells were sub-cultured at 250 x 10^3 cells/cm^2 onto 150 micron circular micropatterned substrates that were attached to the bottom of a modified well-

plate. Cells were allowed to adhere for 24 hours in E6 media with Retinoic acid (RA), they then were treated with Sonic Hedgehog (Shh) protein for two days, priming the cells for gradient stamps. Stamps with Shh gradients were set up 24 hours prior to mounting of the device over the NTMs. On day eight the stamps were refreshed and placed over the tissues, treating the neural organoids with gradients for four days.

5.2.5 Immunocytochemistry and Microscopy

Following differentiation and Shh gradient treatment, the micropatterned tissues were rinsed with PBS and fixed with 4% paraformaldehyde (PFA, Sigma Aldrich) for 10 minutes at room temperature. Fixed tissues were rinsed to prevent over fixing before they were blocked and permeablized in a 5% donkey serum + 0.3% Triton X-100 solution for one hour at room temperature. Tissue were incubated with primary antibodies overnight at 4^0C. After primary staining, the tissues were thoroughly rinsed with PBS – 3x for 15 minutes each – and stained with secondary antibodies for one hour at room temperature, followed by a 30 minute nuclei stain (DAPI, Sigma Aldrich). The tissue received a final thorough wash before they were mounted on glass coverslips using Prolong Gold Antifade Reagent (Thermo Fisher). Brightfield images of tissues were obtained using a Nikon TS100 microscope and fluorescent images were taken using a Nikon A1R confocal microscope.

5.3RESULTS

5.3.2 Well-plate Modification

Here we applied a similar well-plate modifying technique demonstrated previously (Chapter 4) where well bottom modifiers were attached to the bottom of a well plate using medical grade double sided adhesive (ARCare). The well bottom modifiers are designed to hold the hydrogel

stamps in place over the NTM over a multi-day treatment. What is different about this modification is that the well plate itself is also milled, adding slightly more complexity to the system. Because the NTMs are cultured on micropatterned glass coverslips, slots were milled into the plate bottoms for the coverslips to be attached (Fig. 5.1.A). A center hole was milled into the coverslip slots with dimensions that fit the agarose protrusion from the bottom of the stamps with 50 micron tolerances along the outside edges. The patterned coverslips were attached to the slots with the double-sided medical adhesive, resulting in a custom glass-bottom well-plate. The slots were milled deep enough into the bottom of the plate to reduce the bottom thickens directly beneath the well to 450 microns – the thickness of the agarose protrusion from the bottom of the stamp. The double-sided adhesive for the patterned coverslip is approximately 48 microns thick, providing some tolerance of fit.

The well bottom modifiers were aligned and fitted into the wells using a 3D printed assembly apparatus; attaching to the well bottoms using medical grade double sided adhesive (Fig. 5.1.B). When they are placed, the stamps rest on the bottom surface of the well and are held in place by the well bottom modifiers (Fig. 5.1.C). For NSC tissue system, the middle linear region of the gradient was the region focused on. This region – a 2 mm stretch of the gradient centered on the stamp dividing wall – is referred to as the "experimental region" hereafter. To provide space for the neural organoids to develop beneath the stamps within the experimental region, a tissue culture chamber (2 x 2 x 0.45 mm) was molded into the agarose protrusion (Fig. 5.1.D).

5.3.2 Gradient Stamp Characterization

To estimate the size, shape, and time it takes to develop a gradient within the well-plate stamps, finite element analysis (FEA) software was used to model the system. Because agarose hydrogel has relatively large average pore size, gradient development was modeled as diffusion of a molecule of interest (MOI) through an aqueous medium. The gradient was to be experimentally characterized

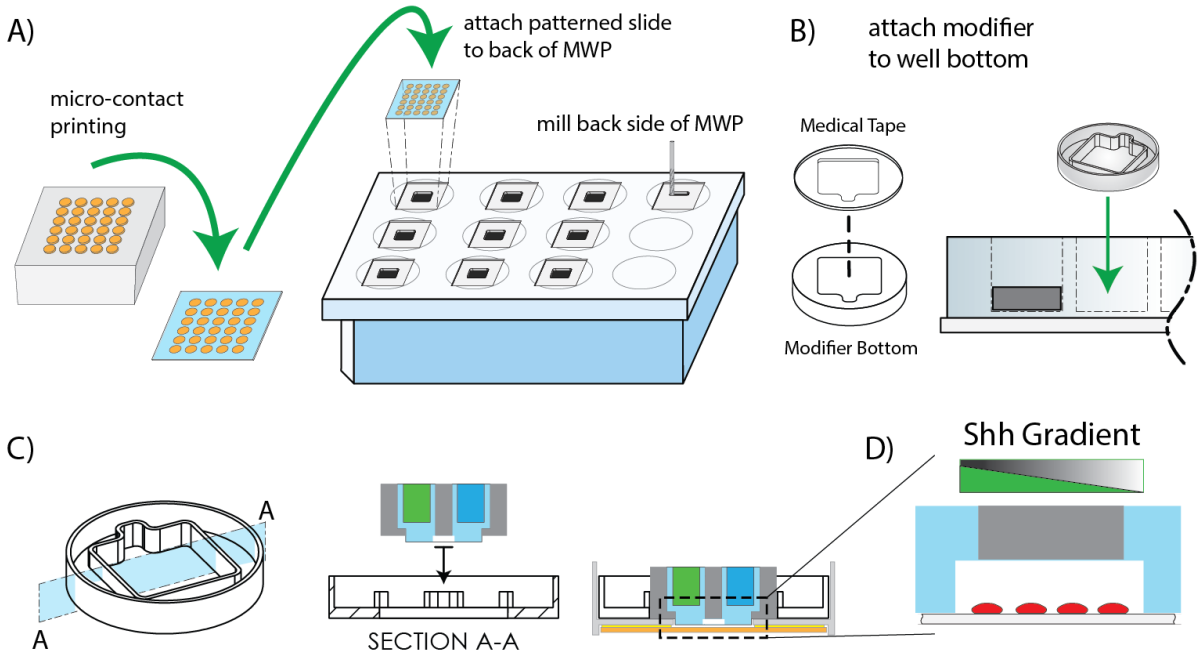

Figure 5.1. *NTM Well-plate Gradient Stamps* – A) Glass coverslips are micropatterned and attached into the recess that was milled out of the bottom of a 12-well plate. B) Well bottom modifiers were affixed to the bottom of the wells. C) The well bottom modifiers maintain proper stamp alignment throughout the culture treatment. D) The stamps have a 2 x 2 x 0.45 mm cell culture region molded into the agarose bottom protrusion to provided ample space for neural organoids to grow.

with fluorescently labeled 10 kDa dextran so the diffusion coefficient of that molecule was used in the model. To simulate periodic well refresh events, time series depended reaction equations were used as previously demonstrated (Chapter 4). The time series used with the reaction functions are listed in Appendix 2. The FAE model suggested that a relatively steady gradient can be formed within 24 hours and be maintained for several days following (Fig. 5.2.A-B). The source/sink well refresh protocol found to generate the steady gradient was dependent on a time series where the wells were refreshed at hours 3, 6, 9, 24, 48, 72, and 96, as established in Chapter 4.

To confirm expected gradient development in the stamps, solution of 10 kDa dextran (AF 560 labeled) were used. The addition of near-instantaneous gradients was desired when treating NTM tissues, so stamp gradients were generated in a separate setup plate for 24 hours prior to

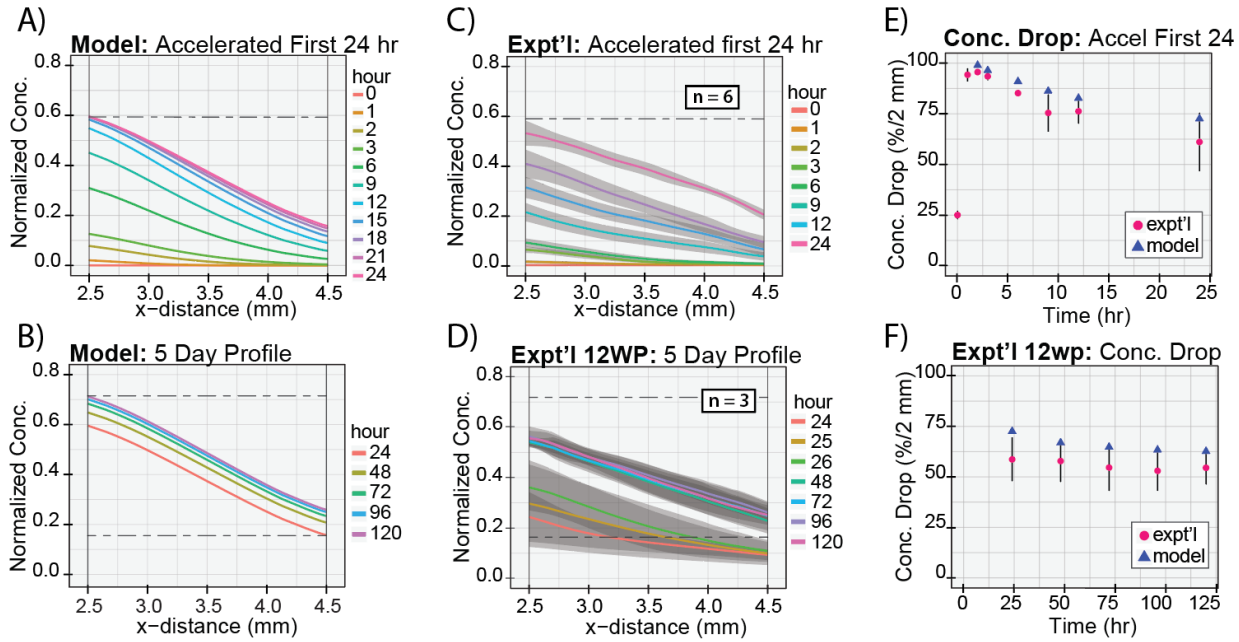

Figure 5.2. *NTM Gradient Characterization* – Because we are only concerned about neural organoids within the cell culture region, we monitored the middle 2 mm of the gradients, the "experimental region." The first 24 hours of gradient development was compared with the model (A), focusing on the gradient profile (C) and concentration drop (E). Next, the stability of the gradient was monitored for another four days and compared to the model (B), again comparing the profile (D) and concentration drop (F).

placement of the stamps over the tissues within a modified well-plate. For thorough characterization, the

setup plate protocol was replicated in dextran diffusion experiments. This meant having the track the first 24 hours of gradient development within the setup plate. In the setup plate, the dextran gradient progresses as expected, though the concentration drop is slightly less than predicted (Fig. 5.2.C & E).

Following the refresh event at hour 24, the stamps were moved from the setup plate to the modified well-plate. The gradient was maintained for 4 days, mimicking a morphogen gradient treatment period. Following the placement of stamps within the well-plate the gradients appeared slightly perturbed by the action, exhibiting initial dilution and higher gradient variability amongst replicates in the hours immediately following. However, the gradients soon stabilize and remain

steady for the remainder of the culture (Fig. 5.2.D). As seen with the first 24 hours, the concentration drop along the stamp gradients was slightly lower than predicted results, though it was stable enough to proceed with biological testing (Fig. 5.2.F).

5.3.3 Neural Tube Microarrays

Deriving spatially differentiated neuroepithelial tissues is a 13 day process (Fig. 5.3.A). In preparation for differentiation experiment, hESCs are sub-cultured at 200 x 10^3 cells/cm^2 in E8 media with 10 μM ROCK inhibitor overnight. The next day the media is rinsed and replaced with E6 media treatment. The sub-cultures were treated with E6 for five days. After day one of E6 treatment, FGF8 was added to the media. After day two of treatment, CHIR boost was added to the media. Media was refreshed daily over this period.

Following five days of E6 sub-culture, the hESCs were dissociated then seeded into a modified well-plate at 250 x 10^3 cells/cm^2 in E6 + RA media and cultured overnight. On day six the Shh protein was added to the culture media, priming the tissues for two days leading up to stamp treatment. The gradients were set up on day seven and the stamps were placed on the cultures on day eight, where they remained for four days, spatially treating the neural organoids.

Four different gradient conditions were set up in order to explore the effects of varying concentrations of Shh gradients (Fig. 5.3.B). Three stamps had source solutions of 0.5, 1.0, and 2.0 μg/μL Shh with sink solutions of E6 + RA media. The fourth stamp was the negative control, with both stamp wells filled with sink media (E6 + RA). Stamp gradients were started 24 hours prior to mounting onto micropatterned tissues. Stamp gradients were set up and maintained identically to the dextran characterization gradients (Fig. 5.3.C)

Olig2 gradient expression

Throughout the gradient treatment, NTMS appeared unperturbed beneath the stamps (Fig. 5.4.C). After the final day of gradient treatment, stamps were removed and culture were fixed,

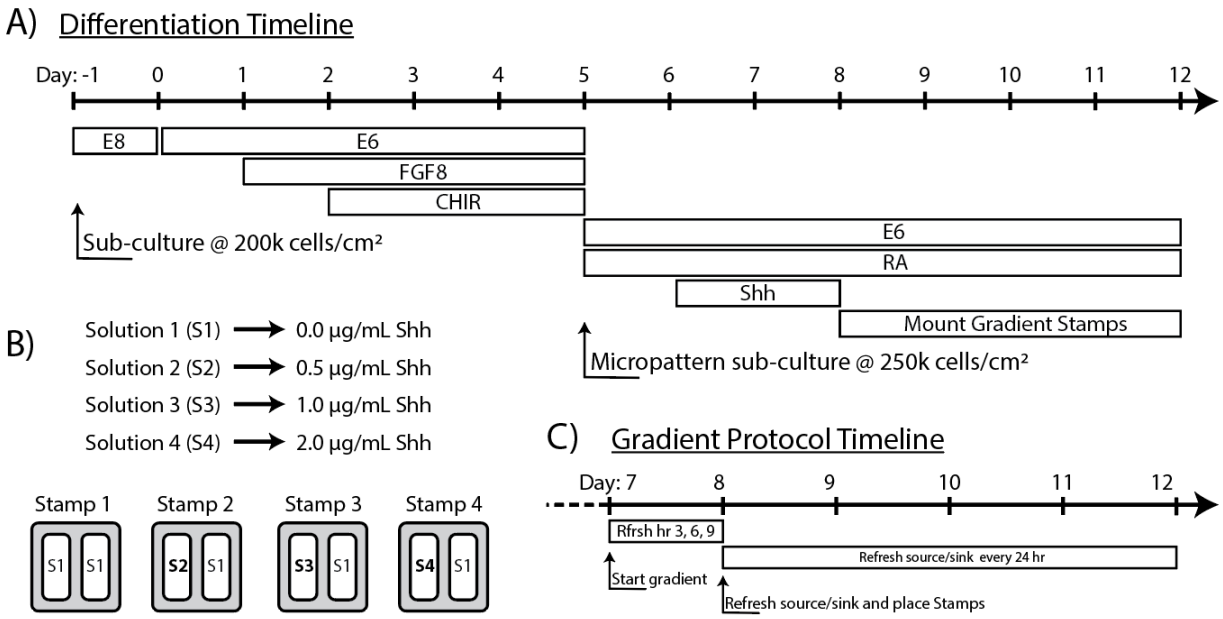

Figure 5.3. *Organoid Culture and Gradient Treatment* – A) Overall derivation and ventral patterning of the hPSC neural organoids takes 13 days, first sub-culturing in E6 treatment within a 6-well plate, then sub culturing on the micro patterned substrates before gradient stamp treatment. B) Four experimental stamps were prepared for NTM Shh treatment. C) Shh gradients were set up and maintained for the four day treatment according to the gradient protocol.

permeabilized, and stained. To identify tissue organization and differentiation, NTMs were stained for N-cadherin, Nkx6.1, Olig2, and DAPI. Neural rosette organization can be visualized with N-cadherin staining while cell nuclei can be identified with DAPI. Ventral differentiation of neuroepithelial cells was monitored by observing Nkx6.1 and Olig2 expression.

In concordance with the Shh gradients, neural rosette Olig2 expression was spatially dependent. However, there appears to be a concentration threshold above 1 µg/mL where rosettes exhibit uniform Olig2 expression (Fig. 5.4.A-B). This is most evident in the 2.0 µg/mL Shh stamps where rosettes along the length of the gradient within the experimental region exhibit approximately 50% Olig2 nuclei staining. As expected, the rosettes treated with the control stamp expressed no Olig2. While not as predominantly expressed as Olig2, Nkx6.1 expression was also expressed in a concentration dependent manner (Fig. 5.4.D).

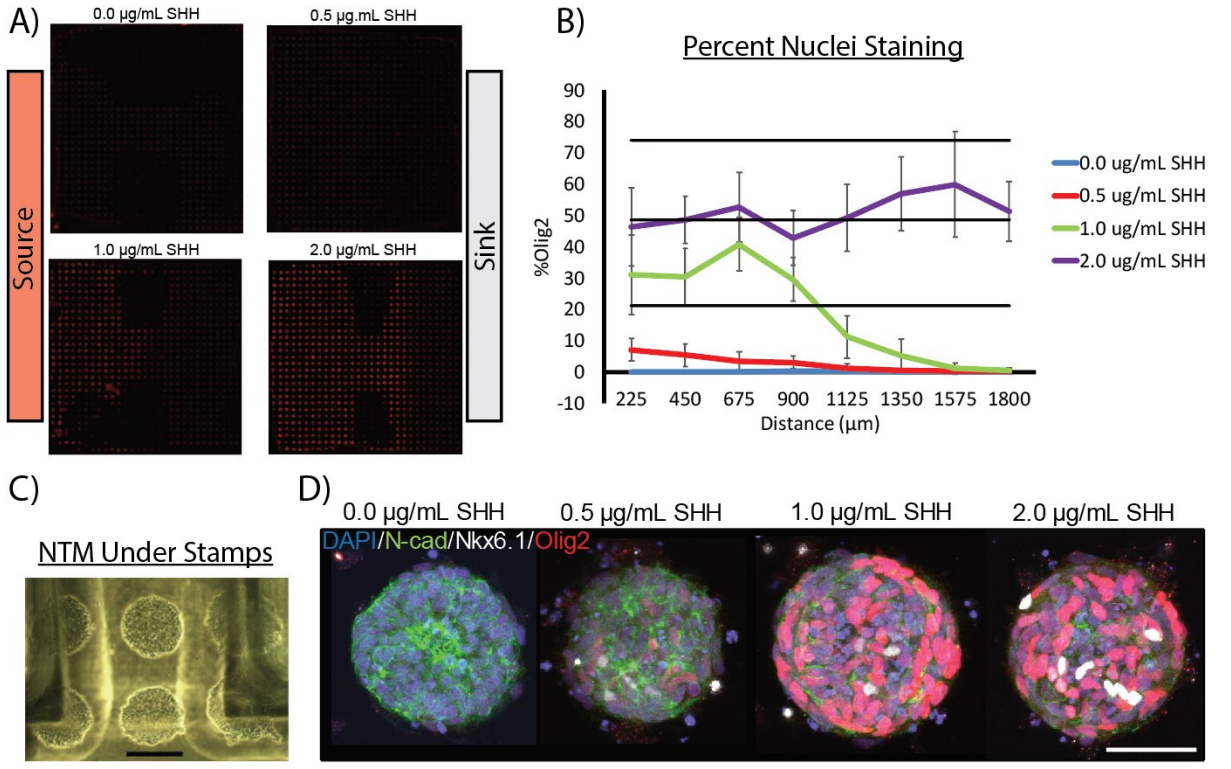

Figure 5.4. *Ventralized hPSC Organoid Microarrays* – A & B) NTMs underneath 0.5 and 1.0 µg/mL Shh gradients exhibited a spatially dependent differentiation response as shown by Olig2 staining, while 2.0 µg/mL stamps showed uniform differentiation and 0.0 µg/mL induced no differentiation. C) Neural organoids appear unperturbed by the well-plate stamps. D) There was a definitive response to increasing gradient concentrations of Shh, with tissues culturing in higher concentrations exhibiting greater ventral differentiation as show by increased Olig2 and Nkx6.1 expression.

5.4 DISCUSSION

Though the work presented in this chapter is preliminary, it is promising. We have demonstrated the ability to create highly organized neural organoid tissues underneath microfluidic gradient stamps in a high-throughput manner. As this platform is further developed, it could prove to be a useful model in neurodevelopment and neural disease studies. For example, neural stem cells could be derived from human induced pluripotent stem cells (iPSCs) from patients with a specific CNS disease. Such cells would retain the mutated gene responsible for the disease. In fact, G. Knight and

R. Ashton et.al. have published on their ability to produce NTMs with an ALS-iPSC line of cells[160]. In the future it would be interesting to investigate Shh induction of motor neuron development and retention amongst these neural organoids compared to healthy neuroepithelial derived NTMS.

G. Knight and R. Ashton et.al. have also demonstrated the ability to engineer micropatterned substrates with "clickable" chemistry to allow tissue outgrowth once rosettes have formed[161]. This would be a useful tool to integrate with the well plate gradient stamps because it would allow organoid outgrowth after the highly controlled derivation and spatial differentiation. Organoids have been observed merging with one another, forming larger rosettes that more closely resemble a developing human neural tube. If this process were to be controlled and characterized, it could provide highly valuable tissue models for future research.

6. Future Work and Conclusion

6.1 FUTURE WORK

For both the automated BAL processing platform and the SASCA, we would like to process more patient samples so we can continue to test the technologies and build a larger patient dataset. What could be interesting is if we were to use the SASCA on enriched BAL samples because the provide a highly heterogeneous sample, leading to background cell carryover, similar to what is seen in the VERSA device. Being able to isolate sub-fractions of cells from a BAL sample could provide insights into lung cancer diagnostic and monitoring markers. What is more, BAL samples are predominantly immune cells and it is known that tumors can have distinct immune cell profiles[162]. Given these facts, BAL samples could provide a wealth of insight in this area of study, so being able to process such samples in a gentle, automated fashion should prove useful.

The well-plate gradient stamp studies presented in this thesis have demonstrated the baseline capabilities of the technique. However, besides the preliminary NTM differentiation results, there is little demonstration of entirely novel biological observations. The next steps will be to begin experimenting with specific tissue models, as we have begun to do with the micropatterned neural organoids. Upcoming work will focus on fine-tuning the Shh gradient protocol to generate spatially differentiated tissues more consistently. Once this is achieved, we can begin to explore disease models, such as hPSCs derived from ALS patients. As this is a disease that affects the patients motor neurons, creating neural tube organoids ventral – motor neuron – patterning is key for the proper development of this model. Eventually, it is desired to dorsally differentiate the NTMs as well, requiring a gradient of BMP family proteins to counter the ventralizing Shh gradient.

As the neural differentiating gradient stamps are further characterized other gradient profiles could be explored. The stamps used currently generate a linear gradient within the experimental

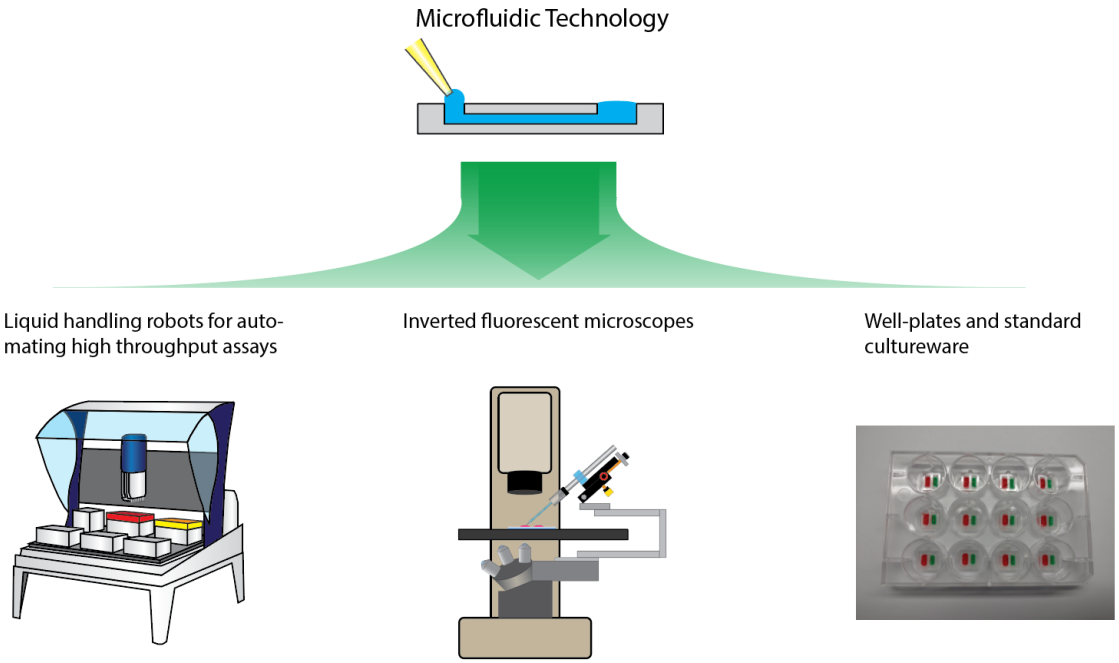

Figure 6.1. *Microfluidic Lab Upgrades* – We have developed upgrades to liquid handling robots, fluorescent microscopes, and multi-well plates.

region because the net diffusion of the MOI is only in one direction. By altering the design of the well-plate gradient stamps, unique profiles can be achieved. Throughout the development on the linear gradient stamps, other designs were proposed which would produce gradients with exponential decay profiles by allowing net diffusion in all 3-dimensional directions, diluting the MOI more quickly (Fig. 6.2). Such designs could provide gradients more mimetic of those seen *in vivo*, as molecular diffusion within tissues also occurs in 3 dimensions.

Another way to modify well-plates with microfluidic gradients could be to affix a more permanent structure to the bottom of the wells. While this method does not allow for the quick addition of a fully developed gradient, like the gradient stamps, it does provide the freedom to test more unique designs. One option we have explored is a point-source gradient insert (Fig. 6.3.A). The device consists of a disc held above the culture surface by posts made out of double-sided adhesive. The space beneath the disc is where tissue cultures are grown and where the gradient

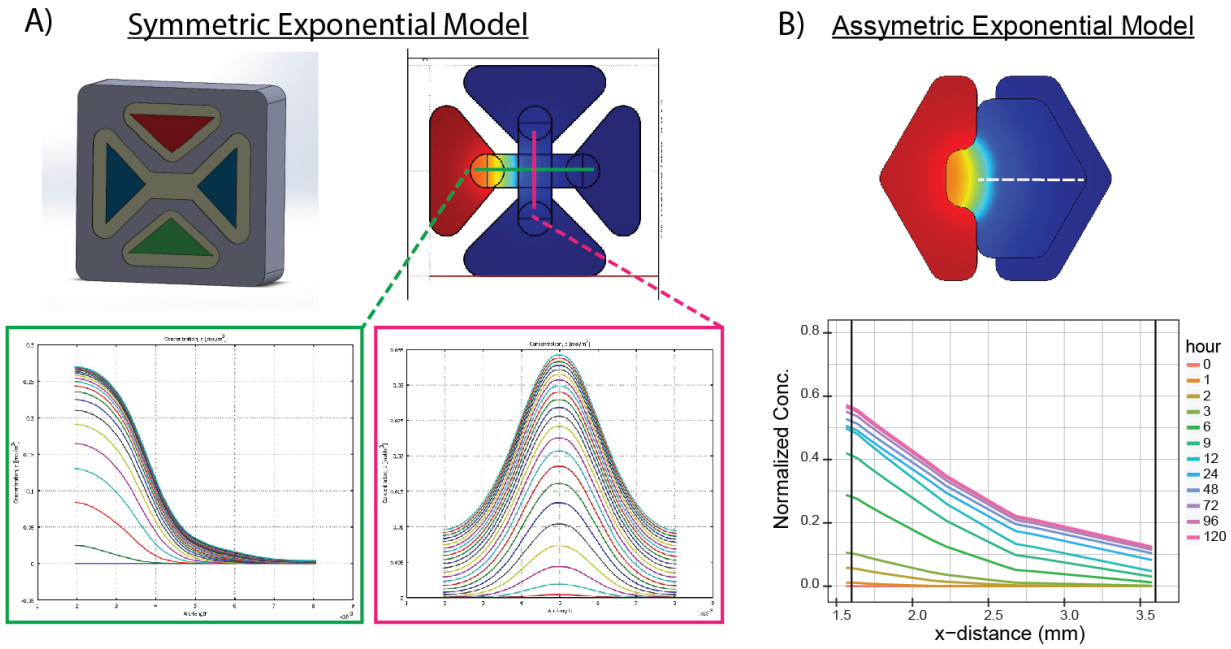

Figure 6.2. *Exponential Gradient Stamps* – In our work we have explored various gradient stamp options, including symmetric exponential gradients (A) and asymmetric exponential gradients (B).

develops. The source is attached to the top of the disc and diffuses through a central pore in the middle of the disc. Flow through the pore in inhibited by the addition of a 5 micron track etch membrane. The point-source inserts are designed to fit into 24-well plates, enabling high-throughput cultures. Because the MOI diffuses radially from a single point, within 24 hours these inserts produce gradients with large concentration drops, relative to the linear stamps (Fig. 6.3.C).

A final idea we had on upgrading well-plates was inspired by the rail channel well-plate inserts reviewed in Chapter 1. The rail channel inserts we designed were designed to fit into the wells of a 24-well plate and they were not too dissimilar than devices already published. What intrigued us about these devices were the various different experiments that could be run within them. The first design was a simple single-rail channel (SRC) that separates two large wells on either side (Fig. 6.4.A). The second design is a double-rail channel (DRC) that consists of a middle tissue culture region and two larger wells on either side of the rails (Fig. 6.4.B).

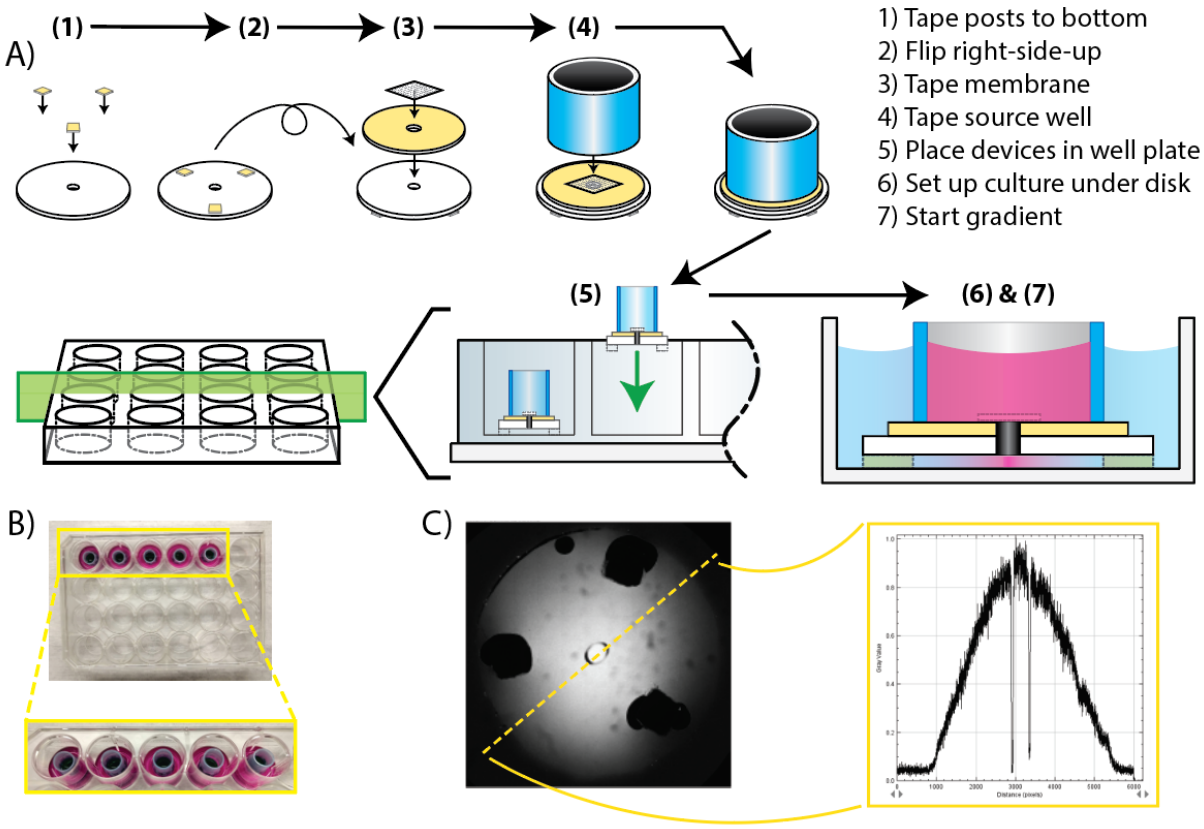

Figure 6.3. *Point Source Gradient Inserts* – Other well plate gradient inserts have also been explored. A) Point source gradient inserts consist of a source well above an experimental area beneath a PS disc. B) Point source inserts were design to fit within a 24-well plate. C) Preliminary data suggests they also produce steady, long-term gradients.

To operate properly, the rails channels must be filled with hydrogel, inhibiting convective flow, which could compromise any gradients developed within the systems (Fig. 6.4.C). Cells could be embedded within the gel within the rail channels and these cells could be subjected to gradients developed between the adjacent large wells, whether they are generated by a source solution or by cells in co-culture. Cells embedded in rail-channels could also be subjected to gravity driven flow by filling only one of the adjacent wells (Fig. 6.4.D). The creeping flow through the gel could be mimetic of interstitial flow within the body, which has been seen to produce migratory reactions in certain tumor cells[163,164]. The DRC device provides more tissue complexity than the SRC device because it could have up to 5 different sub-cultures within the same device compared to the SRC's three culture areas (Fig. 6.4.E). Even with the added co-culture complexity they DRC remains very simple

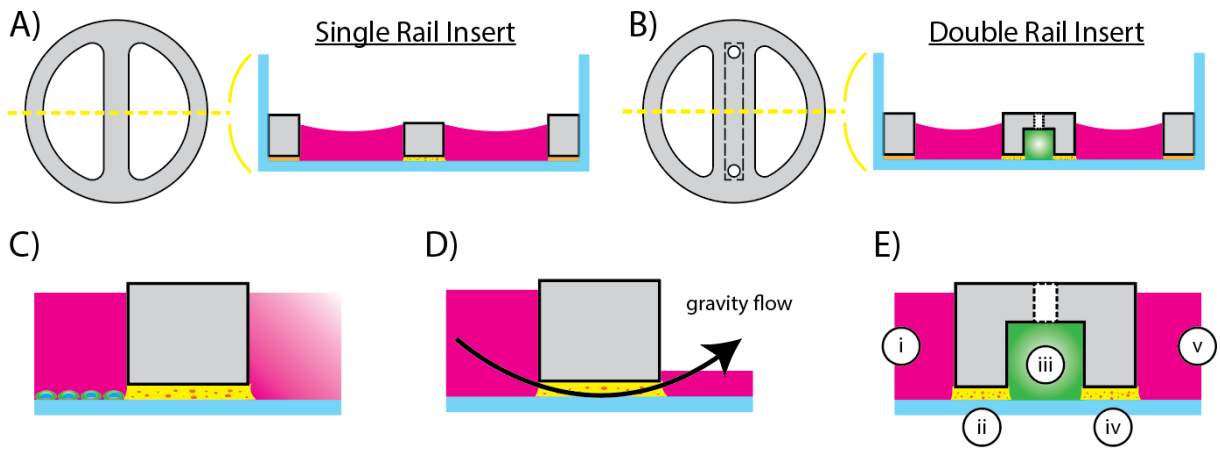

Figure 6.4. *Simple Rail Channel Inserts* – The rail channel inserts previously demonstrated are still rather complex. In response, we have developed simpler rail channel devices that can still be used to perform complex tissue culture experiments. Here we propose a single (A) and double (B) rail channel insert that fits within a 24-well plate.

to setup and operate, demonstrating how such devices could be beneficial in future high-throughput tissue culture studies.

6.2 CONCLUSION

Microfluidics presents many unique advantages in biomedical research. Over the last 20 years scientists have developed many ways to integrate microfluidic devices with established laboratory equipment. In this thesis we have presented a few new techniques for upgrading laboratory equipment with microfluidic technology (Fig. 6.1). First, we demonstrated an automated method for processing bronchoalveolar lavage (BAL) samples by integrating a surface tension driven analyte extraction plate with a liquid handling robot. With this platform we were able to isolate and investigate patient lung cancer cells. Second, we presented an affordable way to upgrade a standard inverted microscope into a semi-automated single cell aspirator (SASCA), which uses a unique microwell array device to entrap and isolate sub-populations of cells from a heterogeneous sample. With the SASCA we were able to select individual CTCs from three different patient samples,

performing RNA PCR analysis on the third sample. Third, we illustrated a well-plate modification technique that was able to upgrade simple well plate tissue cultures with gradient stamps. The hydrogel gradient stamps proved versatile; instigating neutrophil chemotaxis, producing cell proliferation curves within both 2D and 3D tissues, and providing a wealth of data from chemotherapy drug gradients. This technique was further developed to incorporate micropatterned glass substrates and neural tube microarrays (NTMs). The well-plate gradient stamps were able to induce a spatially dependent motor neuron differentiation with Shh gradients. Each of these studies adds to the wealth of evidence that interfacing microfluidic techniques with established equipment could provide incredible technological advancements throughout biomedical research.

Appendix 1

Table S1. SASCA parts list

Item	Supplier	Product No.	Purpose	Price
50 µm ID glass micropipettes	FivePhoton Biochemicals	MGM 1C-50	Collecting cells from microwells	$225 (30 pk)
Four-axis cell micromanipulator	Siskiyou	MX130R	Position and hold glass micropipette	$775
Microtubing (clear PVC)	U.S. Plastic Corp.	054397	Connect syringe pump to micropipette	$81 (100 ft)
10 µL manual syringe pump	Sutter Instruments	(manual microinjector)	Nanoliter resolution fluid control	$1,495
Aluminum square bar stock (5/8")	Grainger	2EZP2 (36" legnth)	Mounting apparatus support cantilever	$8.32
Aluminum flat bar stock (1/4 x 3")	Grainger	2EYZ6 (36" legnth)	Mounting apparatus base	$9.15
Neodymium Magnets	K&J Magnets	R822CS-N52 (one) R622CS-N52 (two)	Magnetic mounting	$1.19 $1.44 (pair)
Steel Sheet (1/64" thick)	Grainger	16NH24 (10" x 4")	Magnetic mounting	$14.25 (6 pk)
			Total:	**$2,610.35**

Table S1. *SASCA Parts List* -- An itemized list of each component used to construct the magnetically mounted aspirator. Supplier and product number information is provided so others can construct their own. The total cost of all required components is about $2600, making it affordable for any CTC researcher to incorporate into their arsenal of laboratory technology.

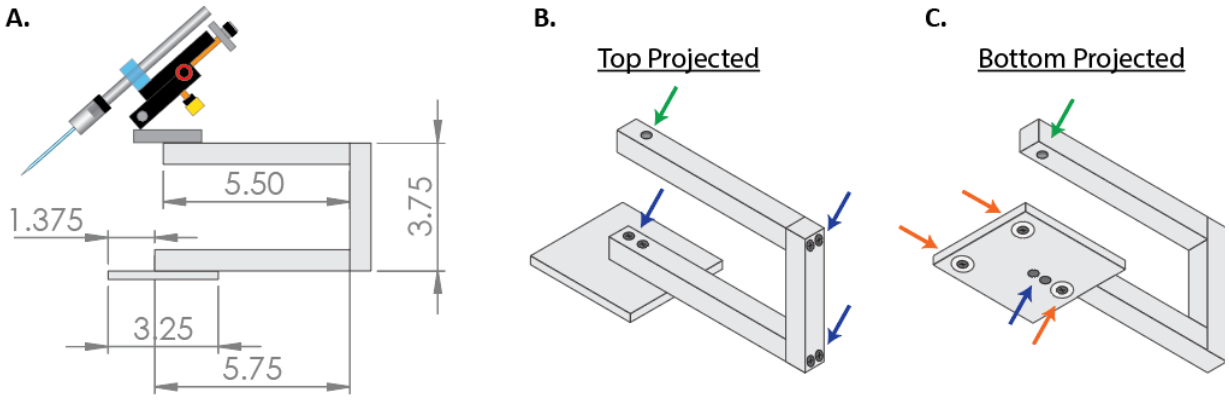

Mounting Cantilever Technical Drawing – A) A technical drawing of the SASCA's mounting cantilever with dimensions shown in inches. Top (B) and bottom (C) projected views of the mounting cantilever with screws and magnets indicated by blue and orange arrows, respectively, while the screw hole for mounting the cell micromanipulator is indicated by a green arrow.

Appendix 2

No Setup Day: refresh every 24 hours

Time Range (days)	series(t) =
0 – 1	0
1 – 1.01	1
1.01 – 2	0
2 – 2.01	1
2.01 – 3	0
3 – 3.01	1
3.01 – 4	0
4 – 4.01	1
4.01 – 5	0

Setup Day: refresh every 24 hours

Time Range (days)	series(t) =
0 – 0.125	0
0.125 – 0.135	1
0.135 – 0.25	0
0.25 – 0.26	1
0.26 – 0.375	0
0.375 – 0.385	1
0.385 – 1	0
1 – 1.01	1
1.01 – 2	0
2 – 2.01	1
2.01 – 3	0
3 – 3.01	1
3.01 – 4	0
4 – 4.01	1
4.01 – 5	0

Setup Day: refresh every 12 hours

Time Range (days)	series(t) =
0 – 0.125	0
0.125 – 0.135	1
0.135 – 0.25	0
0.25 – 0.26	1
0.26 – 0.375	0
0.375 – 0.385	1
0.385 – 0.5	0
0.5 – 0.51	1
0.51 – 1	0
1 – 1.01	1
1.01 – 1.5	0
1.5 – 1.51	1
1.51 – 2	0
2 – 2.01	1
2.01 – 2.5	0
2.5 – 2.51	1
2.51 – 3	0
3 – 3.01	1
3.01 – 3.5	0
3.5 – 3.51	1
3.51 – 4	0
4 – 4.01	1
4.01 – 4.5	0
4.5 – 4.51	1
4.51 – 5	0

References

1 L. R. Volpatti and A. K. Yetisen, *Trends Biotechnol.*, 2014, **32**, 347–350.

2 C. Haber, *Lab Chip*, 2006, **6**, 1118.

3 H. Yu, C. M. Alexander and D. J. Beebe, *Lab Chip*, 2007, **7**, 388.

4 B. H. Weigl, C. J. Morris, N. Kesler, P. Saltsman and R. Bardell, *WELL-PLATE FORMATS AND MICROFLUIDICS-APPLICATIONS OF LAMINAR FLUID DIFFUSION INTERFACES TO HTP SCREENING*, 2001.

5 E. Carrilho, S. T. Phillips, S. J. Vella, A. W. Martinez and G. M. Whitesides, *Anal. Chem.*, 2009, **81**, 5990–5998.

6 C. G. Conant, M. A. Schwartz, J. E. Beecher, R. C. Rudoff, C. Ionescu-Zanetti and J. T. Nevill, *Biotechnol. Bioeng.*, 2011, **108**, 2978–2987.

7 J. I.-Z. C Spencer, C Li, N Chen, Q Johnson, J Nevill, T Kammonen, *Assay Drug Dev. Technol.*, , DOI:10.1089/adt.2011.414.

8 M. Odendahl, H. Mei, B. F. Hoyer, A. M. Jacobi, A. Hansen, G. Muehlinghaus, C. Berek, F. Hiepe, R. Manz, A. Radbruch and T. Dörner, *Blood*, 2005, **105**, 1614–21.

9 S. Hannedouche, J. Zhang, T. Yi, W. Shen, D. Nguyen, J. P. Pereira, D. Guerini, B. U. Baumgarten, S. Roggo, B. Wen, R. Knochenmuss, S. Noël, F. Gessier, L. M. Kelly, M. Vanek, S. Laurent, I. Preuss, C. Miault, I. Christen, R. Karuna, W. Li, D.-I. Koo, T. Suply, C. Schmedt, E. C. Peters, R. Falchetto, A. Katopodis, C. Spanka, M.-O. Roy, M. Detheux, Y. A. Chen, P. G. Schultz, C. Y. Cho, K. Seuwen, J. G. Cyster and A. W. Sailer, *Nature*, 2011, **475**, 524–527.

10 B. Rüster, B. Grace, O. Seitz, E. Seifried and R. Henschler, *Stem Cells Dev.*, 2005, **14**, 231–235.

11 E. S. Lippmann, C. Weidenfeller, C. N. Svendsen and E. V Shusta, *J. Neurochem.*, 2011, **119**, 507–20.

12 E. S. Lippmann, A. Al-Ahmad, S. M. Azarin, S. P. Palecek and E. V Shusta, *Sci. Rep.*, 2014, **4**, 4160.

13 E. S. Lippmann, S. M. Azarin, J. E. Kay, R. A. Nessler, H. K. Wilson, A. Al-Ahmad, S. P. Palecek and E. V Shusta, *Nat. Biotechnol.*, 2012, **30**, 783–91.

14 L. Cao, Y. Yu, J. Wang, J. A. Werkmeister, K. M. Mclean and C. Liu, , DOI:10.1016/j.msec.2016.12.004.

15 A. Kanda, K. Noda, I. Hirose and S. Ishida, *Sci. Rep.*, 2019, **9**, 673.

16 T. Yan, J. Zhang, D. Tang, X. Zhang, X. Jiang, L. Zhao, Q. Zhang, D. Zhang and Y. Huang, , DOI:10.1371/journal.pone.0169155.

17 L. L. Bischel, K. E. Sung, J. a Jiménez-Torres, B. Mader, P. J. Keely and D. J. Beebe, *FASEB J.*, 2014, 1–8.

18 P. Gheibi, K. J. Son, G. Stybayeva and A. Revzin, *Integr. Biol.*, 2017, **9**, 427–435.

19 S. B. Berry, T. Zhang, J. H. Day, X. Su, I. Z. Wilson, E. Berthier and A. B. Theberge, *Lab Chip*, 2017, **17**, 4253–4264.

20 Y. Lee, J. Woo Choi, J. Yu, D. Park, J. Ha, K. Son, S. Lee, M. Chung, B. Ho-Young Kim and N. Li Jeon, *Lab Chip*, 2018, **18**, 2433–2440.

21 Y. J. Yu, Y. H. Kim, K. Na, S. Y. Min, O. K. Hwang, D. K. Park, D. Y. Kim, S. H. Choi, R. D. Kamm, S.

Chung and J. A. Kim, *Lab Chip*, 2018, **18**, 2604–2613.

22 F. Ellett, F. Jalali, A. L. Marand, J. Jorgensen, B. R. Mutlu, J. Lee, A. B. Raff and D. Irimia, *Lab Chip*, 2019, **19**, 1205–1216.

23 G. M. Walker and D. J. Beebe, *Lab Chip*, 2002, **2**, 131.

24 E. Berthier and D. J. Beebe, *Lab Chip*, 2007, **7**, 1475–8.

25 I. Meyvantsson, J. W. Warrick, S. Hayes, A. Skoien and D. J. Beebe, *Lab Chip*, 2008, **8**, 717.

26 J. ROSSIER, S. BARANEK, P. MORIER, C. VOLLET, F. VULLIET, Y. DECHASTONAY and F. REYMOND, *J. Assoc. Lab. Autom.*, 2008, **13**, 322–329.

27 †,‡, Małgorzata A. Witek, †,‡ Mateusz L. Hupert, † Daniel S.-W. Park, § Kirby Fears, †,‡,|| and Michael C. Murphy and †,‡,|| Steven A. Soper*, , DOI:10.1021/AC8002352.

28 E. Berthier, J. Surfus, J. Verbsky, A. Huttenlocher and D. Beebe, *Integr. Biol. (Camb).*, 2010, **2**, 630–8.

29 J. P. Puccinelli, X. Su and D. J. Beebe, *JALA Charlottesv. Va.*, 2010, **15**, 25–32.

30 D. J. Guckenberger, H. M. Pezzi, M. C. Regier, S. M. Berry, K. Fawcett, K. Barrett and D. J. Beebe, *Anal. Chem.*, 2016, **88**, 9902–9907.

31 J. J. Tokar, J. W. Warrick, D. J. Guckenberger, J. M. Sperger, J. M. Lang, J. S. Ferguson and D. J. Beebe, , DOI:10.1177/2472630317696780.

32 S. Wang, L. Ge, X. Song, J. Yu, S. Ge, J. Huang and F. Zeng, *Biosens. Bioelectron.*, 2012, **31**, 212–218.

33 K. A. Ganaja, C. A. Chaplan, J. Zhang, N. W. Martinez and A. W. Martinez, *Anal. Chem.*, 2017, **89**, 5333–5341.

34 A. C. Fu, Y. Hu, Z.-H. Zhao, R. Su, Y. Song and D. Zhu, *Sensors Actuators B Chem.*, 2018, **259**, 642–649.

35 E. W. K. Young and C. A. Simmons, *Lab Chip*, 2010, **10**, 143–60.

36 D. Huh, B. D. Matthews, A. Mammoto, M. Montoya-Zavala, H. Y. Hsin and D. E. Ingber, *Science*, 2010, **328**, 1662–8.

37 D. Huh, Y. Torisawa, G. A. Hamilton, H. J. Kim and D. E. Ingber, *Lab Chip*, 2012, **12**, 2156.

38 E. K. Sackmann, A. L. Fulton and D. J. Beebe, , DOI:10.1038/nature13118.

39 Y.-C. Tung, A. Y. Hsiao, S. G. Allen, Y. Torisawa, M. Ho and S. Takayama, *Analyst*, 2011, **136**, 473–478.

40 J. Kai, A. Puntambekar, N. Santiago, S. H. Lee, D. W. Sehy, V. Moore, J. Han and C. H. Ahn, *Lab Chip*, 2012, **12**, 4257.

41 W. Zhang, Y. Gu, Y. Hao, Q. Sun, K. Konior, H. Wang, J. Zilberberg and W. Y. Lee, *Lab Chip*, 2015, **15**, 2854–2863.

42 C. G. Sip, N. Bhattacharjee and A. Folch, *Lab Chip*, 2014, **14**, 302–314.

43 V. N. Goral, C. Zhou, F. Lai and P. Ki Yuen, *Lab Chip*, 2013, **13**, 1039.

44 D. T. T. Phan, X. Wang, B. M. Craver, A. Sobrino, D. Zhao, J. C. Chen, L. Y. N. Lee, S. C. George, A. P. Lee and C. C. W. Hughes, *Lab Chip*, 2017, **17**, 511–520.

45 A. Haque, P. Gheibi, Y. Gao, E. Foster, K. J. Son, J. You, G. Stybayeva, D. Patel and A. Revzin, *Sci.*

Rep., 2016, **6**, 33980.

46 M. A. Kinney and T. C. Mcdevitt, *Trends Biotechnol.*, , DOI:10.1016/j.tibtech.2012.11.001.

47 L. Ying, Z. Zhu, Z. Xu, T. He, E. Li, Z. Guo, F. Liu, C. Jiang and Q. Wang, *PLoS One*, 2015, **10**, e0129593.

48 B. P. Casavant, E. Berthier, A. B. Theberge, J. Berthier, S. I. Montanez-Sauri, L. L. Bischel, K. Brakke, C. J. Hedman, W. Bushman, N. P. Keller and D. J. Beebe, *Proc. Natl. Acad. Sci. U. S. A.*, 2013, **110**, 10111–6.

49 L. J. Barkal, A. B. Theberge, C.-J. Guo, J. Spraker, L. Rappert, J. Berthier, K. A. Brakke, C. C. C. Wang, D. J. Beebe, N. P. Keller and E. Berthier, *Nat. Commun.*, 2016, **7**, 10610.

50 Y. Lee, J. W. Choi, J. Yu, D. Park, J. Ha, K. Son, S. Lee, M. Chung, H.-Y. Kim and N. L. Jeon, *Lab Chip*, 2018, **18**, 2433–2440.

51 A. Chandrasekaran, F. Ellett, J. Jorgensen and D. Irimia, *Microsystems Nanoeng.*, 2017, **3**, 16067.

52 R. Siegel, J. Ma, Z. Zou and A. Jemal, 2014, **64**, 9–29.

53 T. R. Gildea, P. J. Mazzone, D. Karnak, M. Meziane and A. C. Mehta, *Am. J. Respir. Crit. Care Med.*, 2006, **174**, 982–9.

54 N. Tomiyama, Y. Yasuhara, Y. Nakajima, S. Adachi, Y. Arai, M. Kusumoto, K. Eguchi, K. Kuriyama, F. Sakai, M. Noguchi, K. Murata, S. Murayama, T. Mochizuki, K. Mori and K. Yamada, *Eur. J. Radiol.*, 2006, **59**, 60–64.

55 Y. Wang, F. Jiang, X. Tan and P. Tian, *Medicine (Baltimore).*, 2016, **95**, e4460.

56 T. Azrumelashvili, M. Mizandari, T. Dundua and D. Magalashvili, *Georgian Med. News*, 2016, 32–9.

57 M. K. Gould, J. Donington, W. R. Lynch, P. J. Mazzone, D. E. Midthun, D. P. Naidich and R. S. Wiener, *Chest*, 2013, **143**, 93–120.

58 J. S. Wang Memoli, P. J. Nietert and G. A. Silvestri, *Chest*, 2012, **142**, 385–393.

59 S. Leong, H. Ju, H. Marshall, R. Bowman, I. Yang, A.-M. Ree, C. Saxon and K. M. Fong, *J. Thorac. Dis.*, 2012, **4**, 173–85.

60 S. M. Berry, K. J. Regehr, B. P. Casavant and D. J. Beebe, *J. Lab. Autom.*, 2013, **18**, 206–11.

61 L. Strotman, R. O'Connell, B. P. Casavant, S. M. Berry, J. M. Sperger, J. M. Lang and D. J. Beebe, *Anal. Chem.*, 2013, **85**, 9764–9770.

62 B. P. Casavant, D. J. Guckenberger, D. J. Beebe and S. M. Berry, *Anal. Chem.*, 2014, **86**, 6355–62.

63 E. W. K. Young, E. Berthier, D. J. Guckenberger, E. Sackmann, C. Lamers, I. Meyvantsson, A. Huttenlocher and D. J. Beebe, *Anal. Chem.*, 2011, **83**, 1408–1417.

64 D. J. Guckenberger, T. E. de Groot, A. M. D. Wan, D. J. Beebe and E. W. K. Young, *Lab Chip*, 2015, **15**, 2364–2378.

65 K. Pollock, L. Albares, C. Wendt and A. Hubel, *Exp. Lung Res.*, 2013, **39**, 146–54.

66 J. W. Warrick, A. Timm, A. Swick and J. Yin, *PLoS One*, 2016, **11**, e0145081.

67 J. M. van Haarst, H. C. Hoogsteden, H. J. de Wit, G. T. Verhoeven, C. E. Havenith and H. A. Drexhage, *Am. J. Respir. Cell Mol. Biol.*, 1994, **11**, 344–350.

68 M. G. Pak, D. H. Shin, C. H. Lee and M. K. Lee, *World J. Surg. Oncol.*, 2012, **10**, 53.

69 J.-C. Lin, Y.-Y. Wu, J.-Y. Wu, T.-C. Lin, C.-T. Wu, Y.-L. Chang, Y.-S. Jou, T.-M. Hong and P.-C. Yang, *EMBO Mol. Med.*, 2012, **4**, 472–85.

70 A. Shvartsur and B. Bonavida, *Genes Cancer*, 2015, **6**, 84–105.

71 N. Zhou, H. Wang, H. Liu, H. Xue, F. Lin, X. Meng, A. Liang, Z. Zhao, Y. Liu and H. Qian, *J. Exp. Clin. Cancer Res.*, 2015, **34**, 157.

72 C. Planque, V. Kulasingam, C. R. Smith, K. Reckamp, L. Goodglick and E. P. Diamandis, *Mol. Cell. Proteomics*, 2009, **8**, 2746–2758.

73 A. R. Nobre, A. Albergaria and F. Schmitt, *Acta Cytol.*, 2013, **57**, 1–8.

74 M. L. Ramsey, B. J. Yuh, M. T. Johnson, A. V. Yeldandi and D. L. Zynger, *Virchows Arch.*, 2012, **460**, 89–93.

75 P. C. Mcdonald, J. Winum, C. T. Supuran and S. Dedhar, 2012, **3**, 84–97.

76 J. a Bishop, J. Teruya-Feldstein, W. H. Westra, G. Pelosi, W. D. Travis and N. Rekhtman, *Mod. Pathol.*, 2012, **25**, 405–415.

77 S. Ebinger, E. Ozdemir, S. Tiedt, C. Ziegenhain, C. Castro-Alves, W. Enard and I. Jeremias, *Eur. J. Cancer*, 2016, **61**, S207.

78 S. V. Avery, *Nat. Rev. Microbiol.*, 2006, **4**, 577–587.

79 Z. Shen, A. Wu and X. Chen, *Chem. Soc. Rev.*, 2017, **46**, 2038–2056.

80 L. Yu, S. R. Ng, Y. Xu, H. Dong, Y. J. Wang and C. M. Li, *Lab Chip*, 2013, **13**, 3163–82.

81 J. L. Schehr, Z. D. Schultz, J. W. Warrick, D. J. Guckenberger, H. M. Pezzi, J. M. Sperger, E. Heninger, A. Saeed, T. Leal, K. Mattox, A. M. Traynor, T. C. Campbell, S. M. Berry, D. J. Beebe and J. M. Lang, *PLoS One*, 2016, **11**, e0159397.

82 A. M. Sieuwerts, A. E. Jaco, K. Ae, J. Bolt-De, V. Ae, P. Van Der, S. Ae, B. Mostert, A. E. John, W. M. Martens Ae, J.-W. Gratama, A. E. Stefan, S. Ae and J. A. Foekens, , DOI:10.1007/s10549-008-0290-0.

83 E. Lin, L. Rivera-Báez, S. Fouladdel, H. J. Yoon, S. Guthrie, J. Wieger, Y. Deol, E. Keller, V. Sahai, D. M. Simeone, M. L. Burness, E. Azizi, M. S. Wicha and S. Nagrath, *Cell Syst.*, 2017, **5**, 295-304.e4.

84 A. Goldkorn, B. Ely, D. I. Quinn, C. M. Tangen, L. M. Fink, T. Xu, P. Twardowski, P. J. Van Veldhuizen, N. Agarwal, M. A. Carducci, J. P. Monk, R. H. Datar, M. Garzotto, P. C. Mack, P. Lara, C. S. Higano, M. Hussain, I. M. Thompson, R. J. Cote, N. J. Vogelzang, Jr, R. J. Cote and N. J. Vogelzang, *J. Clin. Oncol.*, 2014, **32**, 1136–42.

85 J. S. de Bono, H. I. Scher, R. B. Montgomery, C. Parker, M. C. Miller, H. Tissing, G. V. Doyle, L. W. W. M. Terstappen, K. J. Pienta and D. Raghavan, *Clin. Cancer Res.*, 2008, **14**, 6302–6309.

86 H. Beltran, A. Jendrisak, M. Landers, J. M. Mosquera, M. Kossai, J. Louw, R. Krupa, R. P. Graf, N. A. Schreiber, D. M. Nanus, S. T. Tagawa, D. Marrinucci, R. Dittamore and H. I. Scher, *Clin. Cancer Res.*, 2016, **22**, 1510–1519.

87 M. Yu, S. Stott, M. Toner, S. Maheswaran and D. A. Haber, *J. Cell Biol.*, 2011, **192**, 373–82.

88 N. J. Nelson, *JNCI*, , DOI:10.1093/jnci/djq016.

89 J. M. Sperger, L. N. Strotman, A. Welsh, B. P. Casavant, Z. Chalmers, S. Horn, E. Heninger, S. M.

Thiede, J. Tokar, B. K. Gibbs, D. J. Guckenberger, L. Carmichael, S. M. Dehm, P. J. Stephens, D. J. Beebe, S. M. Berry and J. M. Lang, *Clin. Cancer Res.*

90 A. Ross, B. Cooper, H. Lazarus, W. Mackay, T. Moss, N. Ciobanu, M. Tallman, M. Kennedy, N. Davidson and D. Sweet, *Blood*.

91 D. T. Miyamoto, R. J. Lee, S. L. Stott, D. T. Ting, B. S. Wittner, M. Ulman, M. E. Smas, J. B. Lord, B. W. Brannigan, J. Trautwein, N. H. Bander, C.-L. Wu, L. V. Sequist, M. R. Smith, S. Ramaswamy, M. Toner, S. Maheswaran and D. A. Haber, *Cancer Discov.*, 2012, **2**, 995–1003.

92 D. T. Miyamoto, Y. Zheng, B. S. Wittner, R. J. Lee, H. Zhu, K. T. Broderick, R. Desai, D. B. Fox, B. W. Brannigan, J. Trautwein, K. S. Arora, N. Desai, D. M. Dahl, L. V Sequist, M. R. Smith, R. Kapur, C. Wu, T. Shioda, S. Ramaswamy, D. T. Ting, M. Toner, S. Maheswaran and D. A. Haber, *Science*, 2015, **349**, 1351–6.

93 Robert Chambers, *J. Infect. Dis.*

94 R. Chambers, *J. Bacteriol.*, 1923, **8**, 1–5.

95 R. Fraser, *Can. Public Heal. J.*

96 S. D. Stoney, W. D. Thompson and H. Asanuma, *J. Neurophysiol.*, 1968, **31**, 659–69.

97 B. F. Brehm-Stecher and E. A. Johnson, *Microbiol. Mol. Biol. Rev.*, 2004, **68**, 538–59, table of contents.

98 E. E. WallachjMD, S.-C. Ng, M. Ariff Bongso, H. Sathananthan and S. S. Ratnam, *Modern trends Micromanipulation: its relevance to human in vitro fertilization*, 1990, vol. 53.

99 J. G. Lohr, V. A. Adalsteinsson, K. Cibulskis, A. D. Choudhury, M. Rosenberg, P. Cruz-Gordillo, J. M. Francis, C.-Z. Zhang, A. K. Shalek, R. Satija, J. J. Trombetta, D. Lu, N. Tallapragada, N. Tahirova, S. Kim, B. Blumenstiel, C. Sougnez, A. Lowe, B. Wong, D. Auclair, E. M. Van Allen, M. Nakabayashi, R. T. Lis, G.-S. M. Lee, T. Li, M. S. Chabot, A. Ly, M.-E. Taplin, T. E. Clancy, M. Loda, A. Regev, M. Meyerson, W. C. Hahn, P. W. Kantoff, T. R. Golub, G. Getz, J. S. Boehm and J. C. Love, *Nat. Biotechnol.*, 2014, **32**, 479–484.

100 D. E. Campton, A. B. Ramirez, J. J. Nordberg, N. Drovetto, A. C. Clein, P. Varshavskaya, B. H. Friemel, S. Quarre, A. Breman, M. Dorschner, S. Blau, C. A. Blau, D. E. Sabath, J. L. Stilwell and E. P. Kaldjian, *BMC Cancer*, 2015, **15**, 360.

101 Y. Gong, A. O. Ogunniyi and J. C. Love, *Lab Chip*, 2010, **10**, 2334.

102 J. Choi, K. Routenberg Love, Y. Gong, T. M. Gierahn and J. C. Love, *Anal. Chem.*, 2011, **83**, 6890–6895.

103 Y. J. Yamanaka, C. T. Berger, M. Sips, P. C. Cheney, G. Alter and J. C. Love, *Integr. Biol.*, 2012, **4**, 1175.

104 T. Ozawa, K. Kinoshita, S. Kadowaki, K. Tajiri, S. Kondo, R. Honda, M. Ikemoto, L. Piao, A. Morisato, K. Fukurotani, H. Kishi and A. Muraguchi, *Lab Chip*, 2009, **9**, 158–163.

105 Y. Xia and G. M. Whitesides, *Annu. Rev. Mater. Sci.*, 1998, 28, 153–184.

106 D. Qin, Y. Xia and G. M. Whitesides, *Nat. Protoc.*, 2010, **5**, 491–502.

107 J. R. Rettig and A. Folch, *Anal. Chem.*, 2005, **77**, 5628–34.

108 V. N. Luk, G. C. Mo and A. R. Wheeler, *Langmuir*, 2008, **24**, 6382–6389.

109 T. Tharmalingam, H. Ghebeh, T. Wuerz and M. Butler, *Mol. Biotechnol.*, 2008, **39**, 167–177.

110 J. R. Lange, J. Steinwachs, T. Kolb, L. A. Lautscham, I. Harder, G. Whyte and B. Fabry, *BPJ*, 2015, **109**, 26–34.

111 Z. Wang and J. M. Belovich, *Biotechnol. Prog.*, 2010, **26**, 1361–1366.

112 J. M. Sperger, L. N. Strotman, A. Welsh, B. P. Casavant, Z. Chalmers, S. Horn, E. Heninger, S. M. Thiede, J. Tokar, B. K. Gibbs, D. J. Guckenberger, L. Carmichael, S. M. Dehm, P. J. Stephens, D. J. Beebe, S. M. Berry and J. M. Lang, *Clin. Cancer Res.*, 2017, **23**, 746–756.

113 B. P. Casavant, D. J. Guckenberger, S. M. Berry, J. T. Tokar, J. M. Lang and D. J. Beebe, *Lab Chip*, 2013, **13**, 391–6.

114 B. P. Casavant, L. N. Strotman, J. J. Tokar, S. M. Thiede, A. M. Traynor, J. S. Ferguson, J. M. Lang and D. J. Beebe, *Lab Chip*, 2014, **14**, 99–105.

115 E. S. Park, J. P. Yan, R. A. Ang, J. H. Lee, X. Deng, S. P. Duffy, K. Beja, M. Annala, P. C. Black, K. N. Chi, A. W. Wyatt and H. Ma, *Lab Chip*, 2018, **18**, 1736–1749.

116 M. Stevens, L. Oomens, J. Broekmaat, J. Weersink, F. Abali, J. Swennenhuis and A. Tibbe, *Cytom. Part A*, 2018, **93**, 1255–1259.

117 A. C. Timm, J. W. Warrick and J. Yin, *Integr. Biol.*, 2017, **9**, 782–791.

118 M. C. Jones, J. J. Kobie and L. A. DeLouise, *Biomed. Microdevices*, 2013, **15**, 453–463.

119 C. D. Ahrberg, J. M. Lee and B. G. Chung, *Sci. Rep.*, 2018, **8**, 2438.

120 M. M. Ferreira, V. C. Ramani and S. S. Jeffrey, *Mol. Oncol.*, 2016, **10**, 374–394.

121 S. Sho, C. M. Court, P. Winograd, S. Lee, S. Hou, T. G. Graeber, H.-R. Tseng and J. S. Tomlinson, *BMC Cancer*, 2017, **17**, 457.

122 J. P. Junker and A. van Oudenaarden, *Cell*, 2014, **157**, 8–11.

123 H. L. Ashe and J. Briscoe, *Development*, 2006, **133**, 385–94.

124 A. Rot and U. H. von Andrian, *Annu. Rev. Immunol.*, 2004, **22**, 891–928.

125 U. B. Kaupp, N. D. Kashikar and I. Weyand, *Annu. Rev. Physiol.*, 2008, **70**, 93–117.

126 E. T. Roussos, J. S. Condeelis and A. Patsialou, *Nat. Rev. Cancer*, 2011, **11**, 573–587.

127 T. M. Keenan and A. Folch, *Lab Chip*, 2008, **8**, 34–57.

128 S. Kim, H. J. Kim and N. L. Jeon, *Integr. Biol.*, 2010, **2**, 584.

129 V. V Abhyankar, M. A. Lokuta, A. Huttenlocher and D. J. Beebe, *Lab Chip*, 2006, **6**, 389–93.

130 O. C. Amadi, M. L. Steinhauser, Y. Nishi, S. Chung, R. D. Kamm, A. P. McMahon and R. T. Lee, *Biomed. Microdevices*, 2010, **12**, 1027–1041.

131 E. K. Sackmann, E. Berthier, E. W. K. Young, M. a Shelef, S. a Wernimont, A. Huttenlocher and D. J. Beebe, *Blood*, 2012, **120**, e45-53.

132 S. F. Moussavi-Harami, H. M. Pezzi, A. Huttenlocher and D. J. Beebe, *Biomed. Microdevices*, 2015, **17**, 9955.

133 J. Parrish, K. S. Lim, K. Baer, G. J. Hooper and T. B. F. Woodfield, *Lab Chip*, 2018, **18**, 2757–2775.

134 B. J. Kim, P. Hannanta-anan, M. Chau, Y. S. Kim, M. A. Swartz and M. Wu, *PLoS One*, 2013, **8**, e68422.

135 M. Arrio-Dupont, S. Cribier, G. Foucault, P. F. Devaux and A. D 'albis, *Biophys. J.*, 1996, **70**, 2327–2332.

136 A. Pluen, P. A. Netti, R. K. Jain and D. A. Berk, *Biophys. J.*, 1999, **77**, 542–52.

137 J.-Y. Xiong, J. Narayanan, X.-Y. Liu, T. K. Chong, S. B. Chen and T.-S. Chung, *J. Phys. Chem. B*, 2005, **109**, 5638–43.

138 M. M. Stevens, M. Mayer, D. G. Anderson, D. B. Weibel, G. M. Whitesides and R. Langer, *Biomaterials*, 2005, **26**, 7636–7641.

139 J. Narayanan, J.-Y. Xiong and X.-Y. Liu, *J. Phys. Conf. Ser.*, 2006, **28**, 83–86.

140 M. E. Young, P. A. Carroad and R. L. Bell, *Biotechnol. Bioeng.*, 1980, **22**, 947–955.

141 D. Brune and S. Kim, *Proc. Natl. Acad. Sci. U. S. A.*, 1993, **90**, 3835–9.

142 T. E. Woolley, R. E. Baker, C. Tickle, P. K. Maini and M. Towers, *Dev. Dyn.*, 2014, **243**, 290–8.

143 S. de Oliveira, E. E. Rosowski and A. Huttenlocher, *Nat. Rev. Immunol.*, 2016, **16**, 378–391.

144 N. L. Jeon, H. Baskaran, S. K. W. Dertinger, G. M. Whitesides, L. Van De Water and M. Toner, *Nat. Biotechnol. 2002 208*, 2002, **20**, 826.

145 C. M. Kurbacher, U. Wagner, B. Kolster, P. E. Andreotti, D. Krebs and H. W. Bruckner, *Cancer Lett.*, 1996, **103**, 183–189.

146 E. Germain, V. Chajès, S. Cognault, C. Lhuillery and P. Bougnoux, *Int. J. Cancer*, 1998, **75**, 578–583.

147 L. Smith, M. B. Watson, S. L. O'kane, P. J. Drew, M. J. Lind and L. Cawkwell, *Mol Cancer Ther*, 2006, **5**, 2115–2135.

148 A. Wu, K. Loutherback, G. Lambert, L. Estevez-Salmeron, T. D. Tlsty, R. H. Austin and J. C. Sturm, *Proc. Natl. Acad. Sci.*, 2013, **110**, 16103–16108.

149 S. Shah, A. Chandra, A. Kaur, N. Sabnis, A. Lacko, Z. Gryczynski, R. Fudala and I. Gryczynski, *J. Photochem. Photobiol. B.*, 2017, **170**, 65–69.

150 N. S. H. Motlagh, P. Parvin, F. Ghasemi and F. Atyabi, *Biomed. Opt. Express*, 2016, **7**, 2400–6.

151 M. C. Regier, E. Olszewski, C. C. Carter, J. D. Aitchison, A. Kaushansky, J. Davis, E. Berthier, D. J. Beebe and K. R. Stevens, *Lab Chip*, , DOI:10.1039/C9LC00122K.

152 M. C. Regier, J. J. Tokar, J. W. Warrick, L. Pabon, E. Berthier, D. J. Beebe and K. R. Stevens, *Sci. Rep.*, 2019, **9**, 6433.

153 M.-F. Chesselet and S. T. Carmichael, *Neurotherapeutics*, 2012, **9**, 241–244.

154 J. Mariani, M. V. Simonini, D. Palejev, L. Tomasini, G. Coppola, A. M. Szekely, T. L. Horvath and F. M. Vaccarino, *Proc. Natl. Acad. Sci. U. S. A.*, 2012, **109**, 12770–5.

155 A. Nyga, U. Cheema and M. Loizidou, *J. Cell Commun. Signal.*, 2011, **5**, 239–248.

156 H.-K. Lee, C. Velazquez Sanchez, M. Chen, P. J. Morin, J. M. Wells, E. B. Hanlon and W. Xia, *PLoS One*, 2016, **11**, e0163072.

157 C. J. Demers, P. Soundararajan, P. Chennampally, G. A. Cox, J. Briscoe, S. D. Collins and R. L. Smith, *Development*, 2016, **143**, 1884–1892.

158 E. S. Lippmann, M. C. Estevez-Silva and R. S. Ashton, 2014, 1032–1042.

159 J. D. McNulty, T. Klann, J. Sha, M. Salick, G. T. Knight, L.-S. Turng and R. S. Ashton, *Lab Chip*,

2014, **14**, 1923–30.

160 G. T. Knight, B. F. Lundin, N. Iyer, L. M. Ashton, W. A. Sethares, R. M. Willett and R. S. Ashton, *Elife*, , DOI:10.7554/eLife.37549.001.

161 G. T. Knight, J. Sha and R. S. Ashton, *Chem. Commun. Chem. Commun*, 2015, **5238**, 5238–5241.

162 T. F. Gajewski, H. Schreiber and Y.-X. Fu, *Nat. Immunol.*, 2013, **14**, 1014–1022.

163 Y. L. Huang, C. Tung, A. Zheng, B. J. Kim and M. Wu, *Integr. Biol.*, 2015, **7**, 1402–1411.

164 W. J. Polacheck, J. L. Charest and R. D. Kamm, *Proc. Natl. Acad. Sci. U. S. A.*, 2011, **108**, 11115–20.